Design of a Switched Reluctance Motor for a Light Sport Aircraft Application

DESIGN OF A SWITCHED RELUCTANCE MOTOR FOR A LIGHT SPORT AIRCRAFT APPLICATION

By

Mohammad Ehsan Abdollahi, B.Sc.

A Dissertation

Submitted to the School of Graduate Studies

in Partial Fulfillment of the Requirements

for the Degree Master of Science

Master of Science (2022) McMaster University

(Electrical Engineering) Hamilton, Ontario, Canada

TITLE: Design of a Switched Reluctance Motor for a Light Sport Aircraft Application

AUTHOR: Mohammad Ehsan Abdollahi

B.Sc. School of Electrical and Computer Engineering

(University of Tehran, Iran)

SUPERVISOR: Berker Bilgin, Assistant Professor

Ph.D. (Illinois Institute of Technology)

NUMBER OF PAGES: XX, 144

تقدیم به پدر و مادر

Dedicated to Mom and Dad

Abstract

With the rapid growth of air travel, concerns about the emissions of greenhouse gas emissions resulting from the air transportation sector are growing. Although the current battery technologies might not be adequate for all-electric regional aircraft, the energy density of the current battery technologies could be adequate to electrify light-sport aircraft used for training and recreation. Due to the nature of the propeller load and noise isolation of the cabin, switched reluctance motors can be an excellent candidate for the propulsion system of electrified light-sport aircraft. The proposed SRM is designed to replace a 70 kW permanent magnet synchronous motor used in the aerospace industry with similar volume constraints and operational requirements. In order to meet the high-power density requirements of this application, a design framework is proposed which includes several layers of the design process. The design objectifies are the average torque, torque ripple, and radial forces by integrating the control and geometry design into the proposed framework. A comprehensive design process is carried out with the proposed framework, and a detailed coil design process is performed. The rotor cut-outs are designed to reduce the weight of the motor. The thermal performance of the motor has been analyzed for the calculated motor losses and the cooling system constraints.

Acknowledgement

It is my distinct pleasure to extend my sincere thanks to my supervisor and mentor, Dr. Berker Bilgin, for his kind support, guidance, and trust. Dr. Berker is an amazing scientist and a tremendous leader both in terms of research and professional ethics. I have learned much from him, and I am grateful for the experience that I have had with him. His unique professional character and dedication to science made him an inspiration to me.

I would like to acknowledge the support and trust given to our project by Dr. Nir Vaks from Carpenter Technology. Dr. Vaks is among the brightest people I have ever known, and his comments on the project always enlightened us. My thanks are also extended to Dr. Babak Nahidmobarakeh, a member of my supervisory committee, for his insightful comments and discussions throughout my studies. I was fortunate to attend Dr. Nahidmobarakeh's course on "Control of Adjustable Speed Drives", which allowed me to develop a deeper understanding of electrical motor drives in particular the fault-tolerance control system that is vital in the electrification of aviation.

My sincere gratitude goes out to Mr. Ahsan Zahid for his cooperation during the project's first phase. This project would not have reached this point without him. His dedication, professionalism, and shrewdness make him one of the best researchers I have encountered. It was an honour to work with him and call him a friend.

My thanks go to my parents and my sister for their support and patience during my academic career. You have provided me with the love and guidance that has enabled me to remain motivated throughout all these years. They taught me never to give up no matter how difficult life became.

Contents

List of Figures

List of Tables

Notation

Abbreviations:

AWG	American Wire Gauge
CCW	Counter-clockwise Rotation Direction
CVD	Chemical Vapour Deposition
CW	Clockwise Rotation Direction
DC	Direct Current
DOE	Design of Experiment
EASA	European Union Aviation Safety Agency
FAA	Federal Aviation Administrator
FEA	Finite Element Analysis
FFT	Fast Fourier Transform
GA	Genetic Algorithm
GHG	Greenhouse Gas
GRSM	Global Response Surface Method
ICE	Internal Combustion Engine
LSA	Light-Sport Aircraft
MMF	Magnetomotive Force
NN	Neural Network
PM	Permanent Magnet
PMSM	Permanent Magnet Synchronous Motor
PSO	Particle Swarm Optimization

PWM	Pulse Width Modulation
RBF	Radial Basis Function
RMS	Root Mean Square
RPM	Rotations Per Minute
SLS	Selective Laser Sintering
SPL	Sound Pressure Level
SRM	Switched Reluctance Motor

Symbols:

A_s	Slot area
σ	Standard deviation
σ_r	Radial force density
σ_t	Tangential force density
α	Circumferential position
α	Electrical angle
B_r	Radial magnetic flux density
B_t	Tangential magnetic flux density
B	Magnetic flux density
β_r	Rotor pole arc angle
β_s	Stator pole arc angle
D	Electric displacement field
ff	Fill factor
f_r	Radial force

H	Magnetic field intensity
h	Convection heat transfer coefficient
I_{coil}	Current of coil
J	Current density
L	Inductance
m_{total}	Total mass
m	Number of phases
Ns	Number of stator poles
Nr	Number of rotor poles
N_{turns}	Number of turns
$P_{max\text{-}continues}$	Maximum continues power
P_{max}	Maximum power
R	Resistance
R_0	Rotor inner radius
R_1	Rotor outer radius
R_2	Slot inner radius
R_3	Stator outer radius
Si	Silicon
t	Time
T_{mech}	Mechanical period
T_{cont}	Continues torque
T_{max}	Maximum torque
u	Temporal order

v	Spatial order
V	Voltage
V_{dc}	DC voltage
W_f	Magnetic field energy
W_c	Magnetic co-energy
ω	Speed of rotor
ω_{cont}	Continues speed
ω_{max}	Maximum speed
μ	Magnetic permeability
ψ	Magnetic flux
λ	Magnetic flux linkage
θ	Rotor position
θ_{on}	Turn on angle
θ_{off}	Turn off angle

Chapter 1

1. Introduction

In the last decade, the electrification of transportation has attracted a lot of attention due to concerns over global warming. The aviation industry contributes between 2-5 percent of global greenhouse gas emissions annually [1], but some studies predict that, with the current increase in the aviation industry's demand, global aviation emissions will increase dramatically by 2050 [1]-[3]. The aviation industry is not electrifying as fast as the rest of the transportation sector, primarily due to the weight, and hence limited energy density of the current battery technologies limiting the range of electrified aircraft. Apart from costly alternatives for fuel, such as sustainable aviation biofuel [4], electrification of the aviation industry is the only way to reduce carbon dioxide emissions produced by aircraft. There are several methods to reduce the emissions through electrification, such as substituting non-propulsive systems – referred as more electric aircraft – or using hybrid-electric propulsion or an all-electric aircraft which utilizes only electric motors for propulsion. Each electrification method requires highly efficient, robust,

and reliable electric motors. Despite its low-cost production and simplicity, the switched reluctance motors (SRMs) are robust, reliable, and they do not require use of permanent magnets. In either case of propulsive and non-propulsive electrification, SRMs are well suited for the electrification of aviation.

1.1: Motivation

The demand for aerial transportation is increasing. As shown in Fig. 1-1, the demand and energy consumption for air travel has increased drastically in the last decades. The aircraft are becoming more efficient, but that is not enough. They are still releasing considerable greenhouse gas emissions. Driven by global warming concerns, the electrified aircraft market was estimated to reach to $178 billion by 2040. That is a considerable growth compared to the size of the market in 2018, which was $99 million [5].

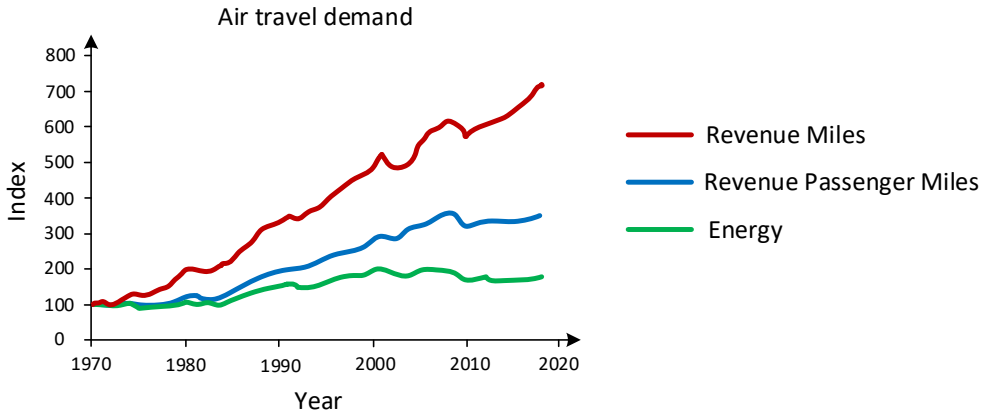

Fig. 1-1. U.S. passenger air travel demand and energy, (100 refers to the index of 1970) [6].

The energy density of the batteries limits the range of the electrified aircraft. The range of an aircraft is highly dependent on energy storage innovations and drive

unit enhancements. For example, the strategic research and development (R&D) investment analysis for the range of eight-seat electric turboprop is illustrated in table 1-1. Each of the scenarios shows the difference in the estimated range based on the possible improvements. Long-haul aviation may not be possible with the current technology of energy storage systems, but short-haul flights may be possible. Short-haul flights, including business aviation, air taxis, training aircraft, and leisure sport aircraft, are not designed for long ranges and are suitable for electrification even with a limited range of current technology. Research and development performed on electrified short-haul aircraft can be scaled up and applied to the next generation of high-range aircraft with high payload and passenger capacities.

Table 1-1: Estimated flying range for an eight-seat turboprop with varying technological improvements [7].

Scenario	Specific energy of batteries	Motor specific power	Flying range [km]		
			min	average	max
sc1	Existing	Existing	53	106	164
sc2		Under development	69	122	178
sc3		Futuristics	72	129	186
sc4	Near-term possible	Existing	141	230	329
sc5		Under development	169	261	352
sc6		Futuristics	181	274	371
sc7	On the horizon	Existing	269	401	531
sc8		Under development	336	452	571
sc9		Futuristics	361	477	594

Switched reluctance motors (SRMs) are one of the most suitable fits for the propulsion system of aviation. The phases of an SRM are electrically isolated from

each other. This makes an SRM highly fault tolerant. The simple and robust construction of SRM without permanent magnets or conductors on the rotor makes it suitable for high-speed and high-temperature operation. The traditional drawbacks of SRMs, such as torque ripple and acoustic noise, are not a significant problem for propulsion systems as the amount of noise produced by the propeller is significantly higher, and the pilot cabin is usually isolated from the drivetrain. The lack of permanent magnets makes SRM independent of the volatile price of rare earth materials.

1.2: Contributions

SRM is a strong candidate for light sport aircraft propulsion systems. In order to propose a more adoptable solution, we defined the design and performance specifications of the SRM based on a 70 kW permanent magnet motor used for a light sport aircraft propulsion system. HIPERCO® 50, a high magnetic saturation iron-cobalt soft magnetic alloy produced by Carpenter Technology, is selected as the magnetic core material of the SRM to improve the torque density of the motor.

In order to design a high power density SRM, a multi-objective design framework has been developed. The framework integrates geometry design and control optimization by utilizing several layers of design optimization methods and nonlinear surrogate models. Rotor cut-outs are proposed to reduce the weight of the motor. The thermal performance of the motor has also been conducted based on the defined cooling constraints. The SRM design meets all necessary specifications.

1.3: Outline of the Thesis

There are seven chapters in this thesis.

Chapter 1 discusses the motivation for this research, including the expected increase in air travel demand and the estimated electric flight range based on the available battery and motor drive technologies. The benefits and limitations of the SRM are discussed, and it was articulated why SRM is a good candidate for electrified propulsion of aircraft.

Chapter 2 reviews the current motor technologies used in the electrification of aircraft, particularly the light-sport aircraft. Different motor specifications are discussed, and the motor specification and constraint selected for this research is presented.

Chapter 3 begins with a summary of the advantages and challenges of SRMs. Main characteristics, (e.g., flux linkage, stored magnetic energy, and equivalent magnetic circuits) and the operational principles of SRMs are explained. A brief explanation of SRM control with asymmetric bridge converters is provided.

Chapter 4 overviews the radial force calculation and verification, its decomposition to temporal and spatial harmonics. Surface waves are used to explain the different temporal and spatial harmonics. A sample radial force harmonics of an 18/12 SRM is presented in the temporal and spatial coordinate system.

Chapter 5 introduces the proposed framework for the design of high-power density SRMs with the integration of control and geometry design. The framework

divides the design process into two stages. In the first stage, surrogate models are used by global optimization algorithms to identify the geometry combinations with the highest average static torque. In the second stage, these geometry combinations are used in a design loop involving control and optimization. In the second stage, dynamic average torque, torque ripple, and radial forces are defined as the objectified.

Chapter 6 utilizes the proposed design framework to design an SRM for the propulsion system of a light-sport aircraft. A coil design process is proposed, and a winding configuration based on the physical constraints is selected. A reduction in weight is achieved by incorporating motor cut-outs. It is verified that the cutouts do not have an impact on the mechanical and electromagnetic performance. In order to examine the motor's performance at various speeds, torque-speed characteristics are developed. The simulation results confirm that the motor meets the performance requirements. The motor losses are calculated for the base speed, and thermal analysis is performed to determine the feasibility of the design with the defined cooling constraints.

Finally, **Chapter 7** the conclusions of this research and provides an outlook on the next steps.

Chapter 2

2. Overview of Electric Motors for Aircraft Applications

2.1: Introduction

Electrified consumer automotive vehicles are currently the central focus of electrification, and commercial electrified automotive vehicles are rapidly entering the market. Mass electrification is primarily driven to reduce the greenhouse gas (GHG) emissions, operating costs, and fossil fuel dependency. According to the environmental and energy study institute, commercial aviation accounts for 2.4% of global greenhouse gas emissions in 2018 and is expected to triple by 2050 [8]. In order to reduce the carbon footprint of aviation, all-electric aircraft are a viable solution. But there is still a long way to go before the aviation industry becomes fully electrified, as the battery energy density significantly affects what can be accomplished in the aviation sector today. Compared to other transportation methods, aviation requires lift force, as shown in Fig. 2-1; hence the aircraft's

weight is extremely important. The energy density of aviation fuel is much higher than the highest-energy-density batteries that are commercially produced today. Due to this issue, several new technologies have been investigated to replace batteries with other energy storage systems like hydrogen fuel cells. These technologies have made significant progress, but there is still much improvements needed.

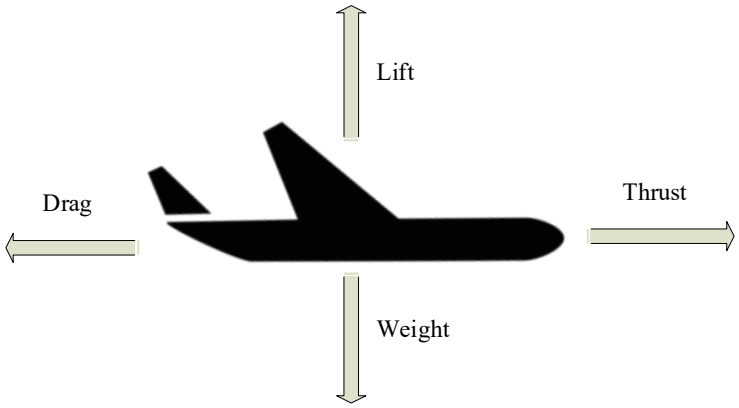

Fig. 2-1. General simplified aircraft forces.

With the trade-off between weight and range, certain applications can be electrified using current battery technology despite weight restrictions. The electrified light-sport aircraft (LSA) segment has been undergoing electrification in recent years, which is expected to be used in flight schools and for general leisure aviation. In the near future, electrified LSAs will become more prevalent, and the technology developed for LSA can be scaled up and applied to the future development of commercial aviation.

2.2: Light-sport Aircraft Market

In the U.S. alone, there are estimated to be 10,800 legacy training aircraft, which are, on average 48.1 years old [9]. In the next decades, the demand for pilots will increase [10]. Using electrified LSA to substitute the aging training aircraft fleet has several benefits. In addition to reducing the greenhouse gas emissions, the initial purchase price and aircraft's operational costs are also reduced. The initial cost of an electrified LSA like the e-Flyer 2 is 289,000 USD, and the initial cost of an internal combustion engine (ICE) LSA like the Cessna 172 (see Fig. 2-2) is 438,000 USD. There is a 51% difference in the initial price of the electrified LSA compared to the ICE LSA, which is a great incentive to buy electrified LSA. An electrified LSA can remarkably downsize the operational cost per hour in comparison to ICE LSA. The operating cost per hour of flight for an e-Flyer 2 (see Fig. 2-3) is $19.80, and for a Cessna 172 is $125.76 [9].

Fig. 2-2. Cessna 172 conventionally used for pilot training schools [11].

Fig. 2-3. Electrified LSA, eFlyer 2 by Bye Aerospace[12].

Generally, light-sport aircraft are powered by piston engines and fueled by aviation gas. Aircraft that operate with small piston engines are responsible for only 0.13 percent of all aviation emissions

[13]. But most aviation fuel contains lead, and a significant portion of that lead is released into the atmosphere. It was reported that, approximately 50% of all lead discharge in the atmosphere is caused by small piston aircraft. Lead is one of the most toxic elements and the effects of lead exposure can be quite profound, especially on children, and can cause neurological and cognitive problems [14].

2.3: Existing Electric Light-sport Aircraft

A wide range of companies, including startups and traditional large corporations, are exploring the possibility of electrifying LSAs. Since an electric motor is smaller compared to internal combustion engines, the aircraft has a greater degree of aerodynamic flexibility. In addition, as a result of the better control over acceleration and power output, the aircraft is able to go faster at a higher efficiency. Fig. 2-4 shows Spirit of Innovation, the latest all-electric light-sport aircraft produced by Rolls-Royce. It is claimed to be one of the fastest all-electric aircraft in the world. The aircraft holds three world records:

- Top speeds of 555.2 Km/h for three kilometers
- Top speed of 532.7 Km/h for fifteen kilometers
- Three kilometers climbed in 202 seconds

In order to produce such an enormous amount of power, three motors are stacked together, which are produced in partnership with automotive powertrain supplier YASA. The powertrain produces 400 kW and a speed of 2200 rpm [15].

Fig. 2-4. Rolls-Royce Electric Aircraft [16].

In order for an aircraft engine to be used in aviation, it must undergo an approval process. The approval process in aviation is complicated and strict due to the nature of the aviation industry, especially to avoid malfunction of a part at a high altitude during a flight. There are a number of detailed guidelines for ICE aircraft that are provided by the Federal Aviation Administrator (FAA) responsible for designating the approvals in the United States [17]. The electrified LSA itself is airworthy as per regular certification; only the motor, controller, and battery require special consideration when it comes to certification [18]. Across Europe, the European Union Aviation Safety Agency (EASA) is responsible for certifying airplanes and their pilots. There is a bit more transparency with the EASA motor certification, and Pipistrel published its certification for an electric LSA motor, the

E-881, on its website [19]. According to the EASA, the Reg. (EU) 2018/1139 Article 77 (1) and Commission Reg. (EU) No.748/2012 should be taken into consideration in the design of electrical motors for electrification of aviation [20].

2.4: Existing Electric Motors for Light-sport Aircraft

In recent years, a variety of electric motors have been developed for aircraft propulsion with high power density and higher efficiency. Table 2-1 summarizes the ones for which the operational data is publicly available. Several companies do not disclose information about their programs due to the high classification of aviation research and development.

Table 2-1: Specification of motors from Siemens, Magnix, and Pipistrel for LSA propulsion [21]- [25].

Motor Name		**SP70D**	**SP55D**	**SP260D**	**E-811**	**Magni500**	**Magni250**
Company		Siemens	Siemens	Siemens	Pipistrel	Magnix	Magnix
$P_{continuous}$		70kW @2600 rpm	55kW @3000 rpm	260 kW @ 2500 rpm	49.2 kW @2350 rpm	560 kW	280 KW
P_{max}		92kW up to 2 minutes	72 kW up to 2 minutes		57.6 kW up to 90 second		
ω_{cont}		2600 rpm	3000 rpm		2350 rpm	1900 rpm	1900 rpm
ω_{max}		2600 rpm	3000 rpm		2500 rpm	2600 rpm	3000 rpm
T_{cont}		260 Nm	180 Nm	1000 Nm	200 Nm	2814 Nm	1407 Nm
T_{max}		340 Nm	240 Nm		220 Nm		
V_{dc}		350-450 V	350-450 V	580 V	400 V	450 - 750 V (V_n = 540)	490 - 750 V (V_n = 540)
m_{total}		26 kg	26 kg	50 kg	22.7 kg	135 kg	71 kg
Cooling		Water /Glycol	Water /Glycol	Oil @90°C	Water /Glycol	Liquid cooling	Liquid cooling
Efficiency		max. 95%		max. 95%		>93%	>93%
Size	***Length***			30 cm	9.1 cm	55.8 cm	27.9 cm
	Diameter			41.8 cm	26.8 cm	65.2 cm	55.9 cm
Fault Protection				Redundant 3-Φ windings		4 x 3-Φ architecture	2 x 3-Φ architecture
Other details		Direct drive for max power density.			Axial flux synchronous PM.	No gearbox needed, high torque in low speed.	

2.4: Selected Motor Specifications and Constraints

A combination of existing LSA ICEs and PMSMs data was used as a reference to determine the motor parameters after an extensive research comparing electrical motors used for aircraft propulsion. In particular, SP70D designed by Siemens is selected as the design objective as shown in Fig. 2-5. SP70D is a direct drive PMSM with continuous power of 70KW and max power of 92KW. This motor was used by Bye Aerospace for their eFlyer all-electric aircraft.

Fig. 2-5. SP70D electrical motor designed by Siemens [24].

Due to the lack of complete information about that specific motor, two other motors, SP260D [22], and Magni250 [23] are used as references to fill the gap with information about SP70D.

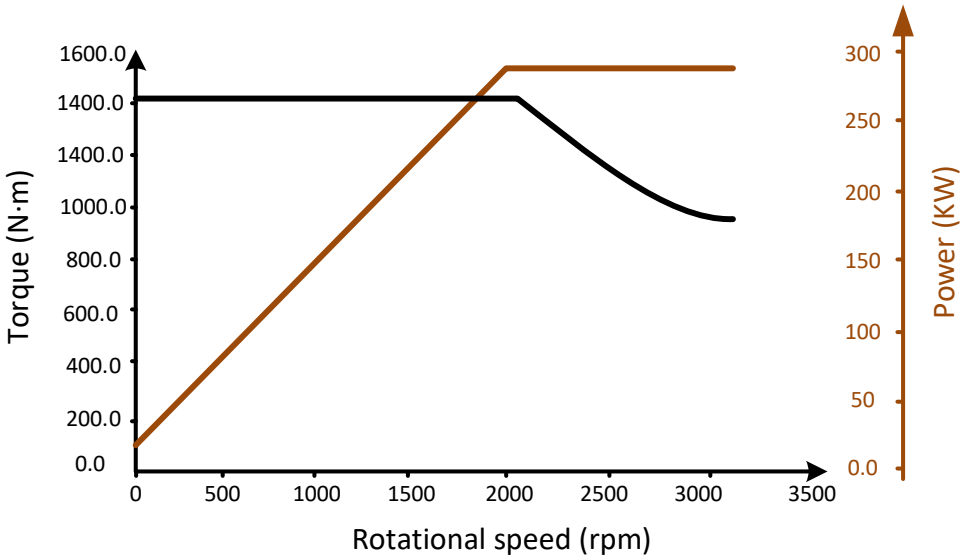

Fig. 2-6. Torque-speed and power diagram for Magni250 [23].

Based on the parameters of SP70D, we can estimate that 30% more power may be used for two minutes. However, this time is limited by the sensitivity of permanent magnets to temperature. Due to the absence of permanent magnets in the rotor, the peak power duration can be higher in SRMs. The thermal class of insulation materials primarily determine the allowable temperature rise in an SRM. We can assume that the motor's winding temperature should not exceed the thermal limit of the winding insulation [27], [28].

Using CAD tools and images of the motor presented in different presentations, the dimensional constraints of the motor are estimated. The motor's input voltage depends on the battery system and the altitude at which the aircraft flies. Based on the Siemens design, the DC link voltage is limited to 450V. The

physical and electrical requirements are summarized in Table 2-2. And the torque-speed envelope requirement is summarized in Table 2-3.

Table 2-2: Target physical and electrical requirements

Parameter	**Current density (A/mm^2)**
Outer Diameter	~300 mm
Stack Length	~100 mm
Shaft Radius	25 mm
V_{DC}	450 V
Current Density	< 30 A/mm^2 (Liquid Cooled Systems)
Ambient Temperature	-20°C to +40°C [24]
Wire Fill Factor	40 to 60 percent

Table 2-3: Target torque-speed envelope requirement

Speed	**Torque**
2600 rpm	260 Nm
4000 rpm	120 Nm

2.5: Conclusions

In comparison to conventional LSAs, electrified LSAs are more efficient, have smaller motors, have better aerodynamics, utilize a more straightforward gearbox, and use simpler cooling systems. They do not emit GHGs into the atmosphere, and they also have reduced operating cost. An analysis is conducted of

existing electrified LSAs with a focus on the electrical motors that power them. After an in-depth analysis of current electrical motors and ICE engines used in electrification of aviation, the specifications and constraints of the design are determined.

Chapter 3

3. Operating Principles of Switched Reluctance Machines

3.1: Introduction

In recent years, switched reluctance motors (SRMs) have attracted a lot of attention due to their simplicity, robustness, and reliability. They are simple in construction and do not require permanent magnets or brushes. The simple structure of the motor makes mass production simpler and more economical [31].

Due to the limited supply and increased global demand, the price of rare earth materials has increased dramatically over the past decades. Currently, the electrification of various transportation sectors is heavily dependent on permanent magnet synchronous motors (PMSMs). However, these motors have a number of supply chain issues, which will only exacerbate over time. As an example, in 2011, the price of rare earth materials spiked for geopolitical reasons [34], [35]. Fig. 4-1 shows the rare earth material price spike in comparison with gold and silver during

that period. Electrification of transportation should not be based on technologies which are highly dependent on the fluctuating prices of rare earth materials. Due to the geopolitical nature of rare earth materials, they can serve as a powerful tool in future trade wars. Furthermore, the rare earth elements used in producing permanent magnets like Neodymium produce a high carbon footprint in the mining, refining, and transportation processes [32], [33]. The SRMs are independent of volatile price and supply chain issues of permanent magnets, making them an ideal option for the next generation of electric motors.

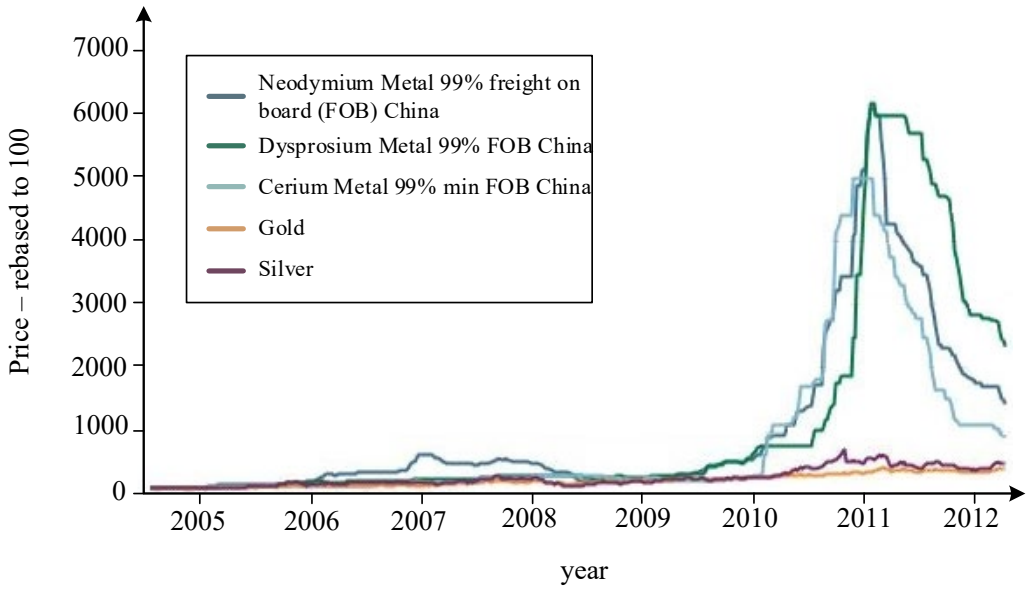

Fig. 3-1. Price of rare earth material vs. gold and silver during the 2011 spike [34].

Permanent magnets are sensitive to temperature; hence the operating temperature of a PMSM can be more limited than an SRM. In an SRM, capability to operate at a higher temperature can likely increase the duration of peak power operation. The limiting factor for the maximum temperature in an SRM is the

insulation and impregnation material softening temperature and fatigue considerations. In addition, SRMs do not contain magnets or conducting bars, which increase the weight and inertia of the rotor of PMSMs and induction motors as they are located closer to the rotor outer diameter. In an SRM, the larger portion of the rotor weight is the back iron, which is closer to the rotating shaft. Therefore, SRMs usually have a lighter rotor weight and lower inertia as compared to PMSMs and induction motors.

Among the top priorities in aviation is the ability to operate fault-tolerantly. PMSMs do not have isolated windings, so if there is a problem in one of the phases or switches, it can cause the whole motor to fail. If a phase winding is shorted, the constant flux of the rotor magnets would induces a voltage in the shorted windings, making the operation after a short circuit fault challenging. Conversely, SRMs are inherently fault-tolerant since they have electrically isolated phases, which reduce the circulating current in the case of short circuit fault. SRMs can operate with reduced power with fewer phases even in case of an inverter fault, as each phase use an isolated converter called an asymmetric bridge converter.

Compared to PMSMs, SRMs have three main challenges: torque ripple, noise and vibration, and power density. However, these challenges can be addressed by designing a motor and controlling it properly. In addition, for the light-sport aircraft (LSA) propulsion, these challenges have a less significant effect on the motor performance. For example, the propeller load, e.g., blades, is less sensitive to torque ripple. The cabin of the aircraft is isolated from the drivetrain, and the

noise of the propeller blade is considerably higher than the motor noise [36]. The weight of the motor is not comparable to the battery and body weight. The weight of the motor is less than 4% of an electrified LSA. The slight difference in the motor weight is acceptable in exchange for the higher reliability that the SRM provides.

3.2: Operating Principles

In order to understand the operating principle of SRMs, it is better to start with the principle of reluctance-based actuators. As shown in Fig. 3-2, a reluctance-based actuator is composed of two main components: a mover, which is equivalent to the rotor, and a core, which is equivalent to the stator. The air gap between the core and mover is the primary source of magnetic circuit reluctance. Based on Lorentz's force, when the coil is conducting current, the magnetic field attempts to minimize the reluctance of the electromagnetic circuit, which means that the airgap between the core and the mover reduces and, hence, the mover gets close to the core (stator). When the coil stops conducting, the spring moves the mover back to a higher airgap and, hence, to a higher reluctance position. This concept has been used in different applications for centuries, for instance, the electric bell.

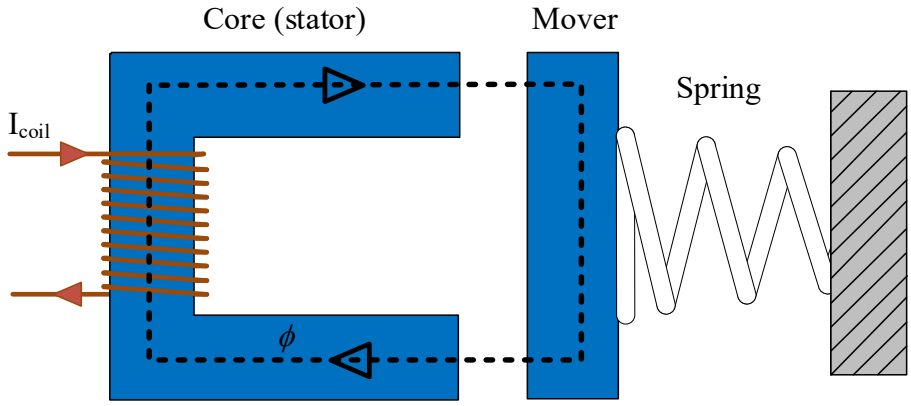

Fig. 3-2. Reluctance based electric actuator.

The idea behind an SRM is similar to the reluctance-based actuators. SRMs consist of salient stator and rotor poles, which are also referred as; and based on the rotor's position with respect to the stator poles, the reluctance of the magnetic circuit is different. For example, for a three-phase 6/4 SRM, Fig. 3-3 demonstrates how the rotor moves from high reluctance to low reluctance by excitation of a single phase. Fig. 3-3-a shows the position when the reluctance is highest for phase A, referred to as the unaligned position. The nature of the magnetic circuit tries to reduce the reluctance,; hence, based on Lorentz law, the rotor moves to a lower reluctance position, as shown in Fig. 3-2-b. The motion stop once the stator and rotor teeth are aligned, and the magnetic circuit is at the lowest reluctance, as shown in Fig. 3-2-c. This position with the lowest reluctance is referred to as the aligned position. Exciting coils of different phases that are located around different stator teeth maintains continuous rotation.

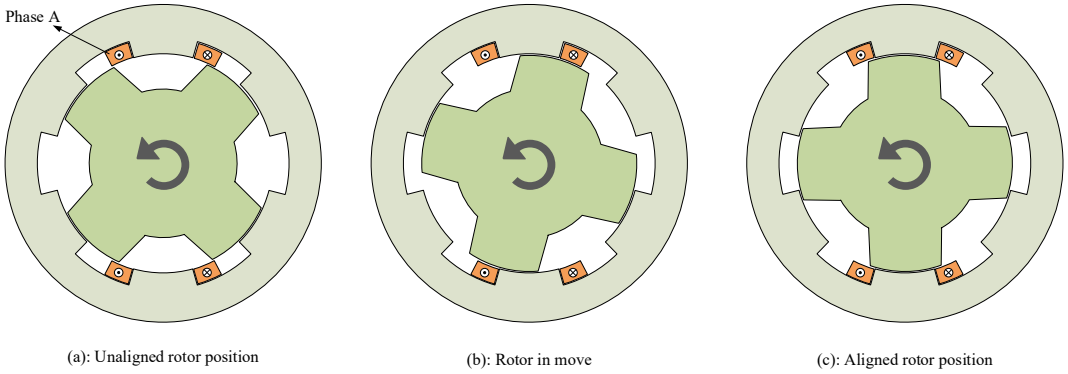

Fig. 3-3. A 6/4 SRM aligning to an energized pole. a) Rotor pole is unaligned, b) Rotor in the move, and c) Rotor pole is aligned.

Internal rotor SRMs have coils on the stator only, and the number of rotor and stator poles can be different combinations depending on the number of phases [37].

3.2.1: Flux Linkage and Stored Magnetic Energy

According to Ampere's law (3.1), when a stator coil is excited, the magnetic field intensity is created by the current density of the coil region:

$$\nabla \times \vec{H} = \vec{J} \tag{3.1}$$

where the $\vec{H}$ is the magnetic field intensity, and $\vec{J}$ is the current density. The magnitude of the current density can be expressed as the product of the number of turns, N_{turns}, and coil current, I_{coil}, over the conductor cross section area, A_{copper}:

$$J = \frac{I_{coil}\, N_{turns}}{A_{copper}}. \tag{3.2}$$

The magnetic flux density, B, is related to the magnetic field intensity, and the equivalent material permeability, μ as shown in (3.3).

$$\vec{B} = \mu\vec{H} \ . \tag{3.3}$$

The magnetic flux, ψ, can be calculated by integrating the magnetic flux density over the cross-section area of the flux path, S:

$$\psi = \int_S \vec{B} \cdot d\vec{S} \ . \tag{3.4}$$

In electric machines, the flux of each turn is added together and create the flux linkage, λ:

$$\lambda = N_{turns}\, \psi. \tag{3.5}$$

The flux linkage in the SRM is dependent on the reluctance; hence, the rotor position. The reluctance and inductance are also dependent on the current and, hence, magnetic field intensity, H, due to the nonlinearity of the ferromagnetic materials used in the stator and rotor cores. The flux linkage is a function of rotor position and coils current, and it can be expressed as:

$$\lambda_{(\theta,i)} = L_{(\theta,i)} i \tag{3.6}$$

where the $L_{(\theta,i)}$ is the inductance as a function of current, i and rotor position, θ. Inductance is dependent on the rotor position, because as the rotor position changes, the relative position of a salient rotor teeth with respect to a salient stator teeth changes and this results in a varying airgap length. Fig. 3-4, illustrates the changes in inductance for different rotor positions. The inductance is the highest when the rotor and stator teeth are aligned. The inductance is the lowest when the stator and rotor are completely unaligned, and the air gap is maximum. When the coils are energized, the rotor moves towards the stator teeth to reach to the aligned position.

This motion can be expressed and formulized better with magnetic energy and co-energy.

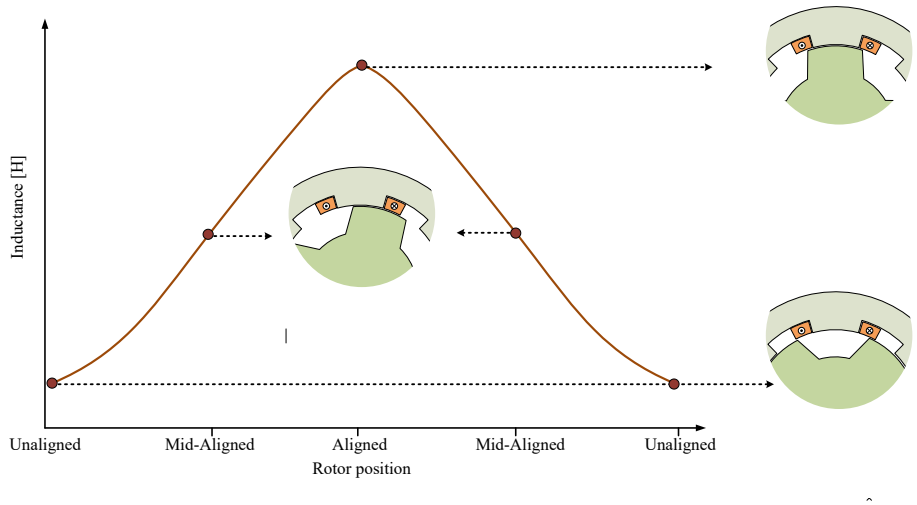

Fig. 3-4. Phase inductance of SRM for different rotor positions at constant current.

In a switched reluctance motor, as the rotor moves towards the aligned position, the airgap gets smaller and, hence, the reluctance of the magnetic circuit reduces. When the airgap is small at the aligned position, the reluctance is the smallest and, hence, the equivalent permeability of the equivalent circuit is high. When the air gap is high at the unaligned position, the reluctance is the highest and, hence, the equivalent permeability is low. Fig. 3-5 illustrates the differences in the inductances for three different rotor positions for varying currents.

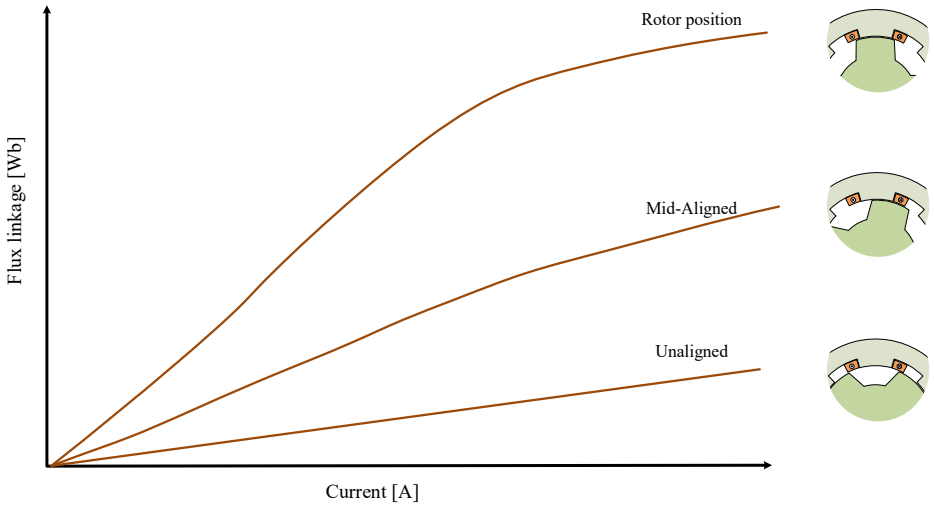

Fig. 3-5. A graph of flux linkage versus current for different positions of the rotor.

Magnetic flux generated by the magnetomotive force by the current applied to the SRM coils flows through the magnetic circuit which is made of the stator and rotor cores, and the airgap. Compared to the stator and rotor cores, which are made of ferromagnetic materials, the airgap exhibits much larger reluctance. The majority of the magnetic energy is stored in the airgap, which is referred as magnetic field energy, W_f:

$$W_f = \int id\lambda. \tag{3.7}$$

The magnetic field energy can be represented graphically as the area above the line of flux linkage-current characteristics in Fig. 3-6. The complement of the magnetic field energy is a non-physical quantity called co-energy, which is useful for the electromechanical conversion of energy. The co-energy is defined as:

$$W_C = \int \lambda di. \tag{3.8}$$

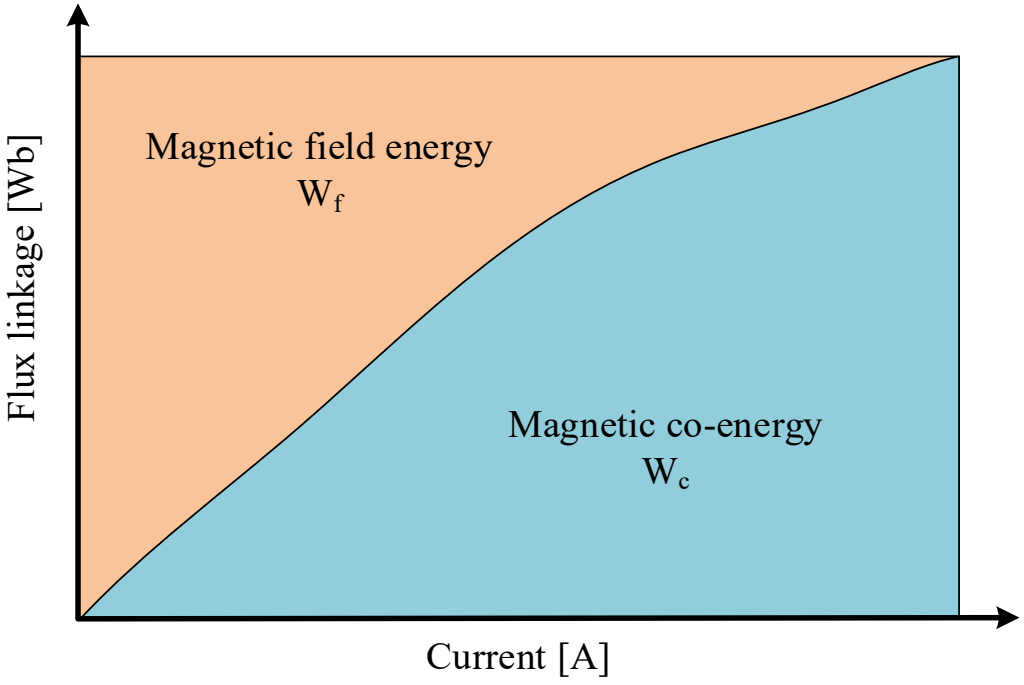

Fig. 3-6. Flux linkage versus current characteristics and the areas representing magnetic field energy and co-energy.

Considering (3.8) and (3.6), the simplified formula for co-energy with constant current is as follows:

$$W_c = \frac{1}{2} L(\theta) i^2. \tag{3.9}$$

In electrical machine theory, the torque, T_e can be calculated based on the change in the co-energy with the rotor position. Using (3.9), electromagnetic torque can be expressed as:

$$T_e = \frac{\partial W_c}{\partial \theta}\bigg|_{i=const} = \frac{1}{2} \frac{dL(\theta)}{d\theta} i^2. \tag{3.10}$$

3.2.2: Equivalent Circuit and Airgap Power

According to Faraday's law of magnetic induction, the phase voltage equation of an SRM can be expressed as:

$$V = iR + \frac{d\lambda_{(\theta,i)}}{dt} \tag{3.11}$$

where λ is flux linkage as a function of rotor position, θ, and current, i. R is the phase resistance, and V is the terminal voltage. Since the flux linkage is the product of inductance and current as shown in (3.6), the terminal voltage equation in (3.11) can be rewritten as:

$$V = iR + \frac{d\lambda_{(\theta,i)}}{dt} = iR + \frac{dLi_{(\theta,i)}}{dt} = iR + L_{(\theta,i)}\frac{di}{dt} + i\frac{dL_{(\theta,i)}}{d\theta}\frac{d\theta}{dt}. \tag{3.12}$$

The speed of the rotor, ω can be used to link rotor position, θ, and time, t:

$$V = iR + L_{(\theta,i)}\frac{di}{dt} + i\frac{dL_{(\theta,i)}}{d\theta}\omega. \tag{3.13}$$

Similar to direct current machines, the term ϵ is defined as representing the airgap power which is converted to mechanical power:

$$\epsilon = \frac{dL(\theta,i)}{d\theta}\omega i. \tag{3.14}$$

Hence:

$$V = iR + L_{(\theta,i)}\frac{di}{dt} + \epsilon. \tag{3.15}$$

The equivalent circuit for a phase of an SRM is shown in Fig. 3-7. The resistance, R is the source of resistive losses, and the back emf, ϵ is caused by airgap power and, hence, is the part that produces the electromagnetic torque.

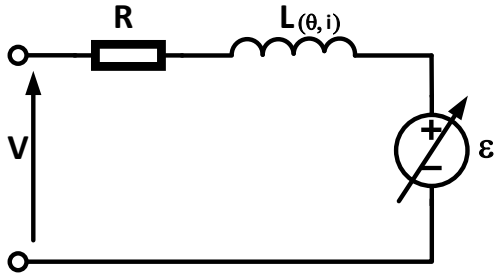

Fig. 3-7. Equivalent circuit for SRM's phase.

In order to better understand the energy conversion of the motor, the instantaneous power for the SRM can be expressed as:

$$Vi = i^2R + i\,L_{(\theta)}\frac{di}{dt} + i^2\frac{dL_{(\theta)}}{d\theta}\omega. \tag{3.16}$$

The changes in magnetic co-energy (3.9) over time can be simplified as follows:

$$\frac{d}{dt}\left(\frac{1}{2}L_{(\theta)}i^2\right) = \frac{1}{2}i^2\frac{dL_{(\theta)}}{d\theta}\frac{d\theta}{dt} + iL_{(\theta)}\ \frac{di}{dt} = \frac{1}{2}i^2\frac{dL_{(\theta)}}{d\theta}\omega + iL_{(\theta)}\ \frac{di}{dt} \tag{3.17}$$

By substituting the expressions in the rectangular boxes in (3.17) in (3.16), the instantaneous power equation can be expressed as:

$$Vi = i^2R + \frac{d}{dt}\left(\frac{1}{2}L_{(\theta)}i^2\right) - \frac{1}{2}i^2\frac{dL_{(\theta)}}{d\theta}\omega + i^2\frac{dL_{(\theta)}}{d\theta}\omega \tag{3.18}$$

Therefore:

$$Vi = i^2R + \frac{d}{dt}\left(\frac{1}{2}L_{(\theta)}i^2\right) + \frac{1}{2}i^2\frac{dL_{(\theta)}}{d\theta}\omega \tag{3.19}$$

The airgap power is dependent on the rate of the change of inductance with rotor position. Since torque is produced from the airgap power, torque production of the SRM is mainly dependent on the change in inductance with rotor positions, as derived from the co-energy in (3.10):

$$Airgap\ Power = \frac{1}{2}i^2\frac{dL_{(\theta)}}{d\theta}\omega = T_e\,\omega \tag{3.20}$$

3.3: Control of Switched Reluctance Motors

As the name switched reluctance motor implies, the excitation of the different phases should be switched to rotate the rotor. In Fig. 3-8, the rotation of a three-phase 6/4 SRM is illustrated by switching the excitation between different phases. After excitation of phase A, the rotor is aligned to phase A (Fig. 3-8-a). Then, phase B is excited, and the rotor moves to align with phase B (Fig. 3-8-b). Then, phase C is excited as shown in Fig. 3-8-c, and the rotor moves to align with phase C. The continuous excitation loop of phases A, B, and C rotates the rotor. The excitation time and shape of the phase current waveform controls the motor speed and torque production.

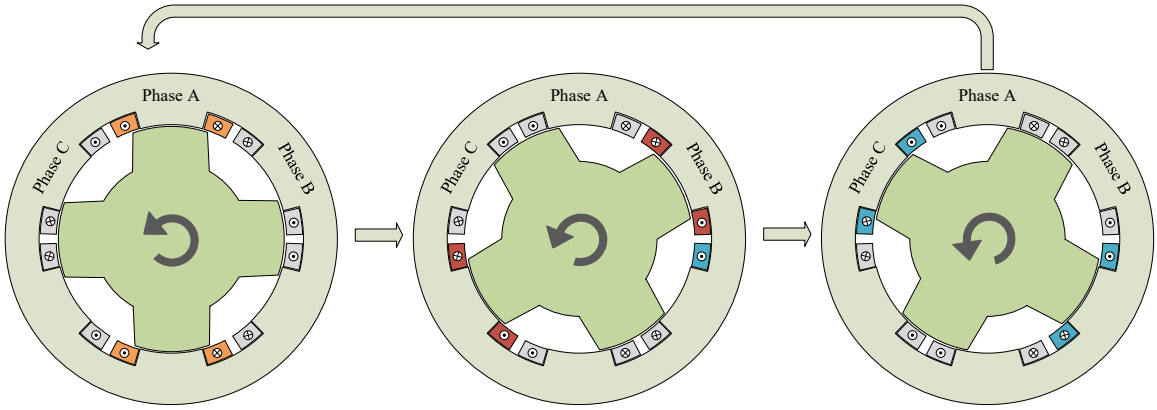

(a): Phase A excited (b): Phase B excited (c): Phase C excited

Fig. 3-8. Switching between different phases in a three-phase 6/4 SRM.

The most commonly used circuit for controlling phase excitation in an SRM is an asymmetric bridge converter. As shown in Fig. 3-9, each phase of an SRM needs one asymmetric bridge converter consisting of two switches and two diodes.

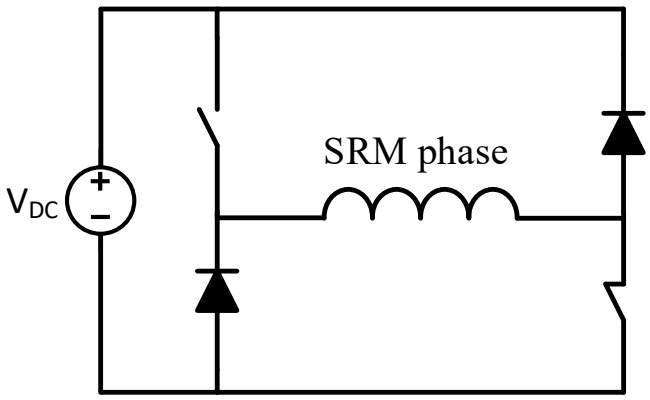

Fig. 3-9. Asymmetric bridge converter used for SRM control.

In an asymmetric bridge converter, different switching states are utilized to control the phase current depending on the control strategy. When both switches are on, the dc link voltage is applied to the phase, increasing phase current (Fig. 3-10-a). When the phase current is non-zero, if both switches are turned off, the diodes become forward biased. A negative dc link voltage is applied to the phase, reducing the phase current (Fig. 3-10-b). If only one of the switches is conducting, the phase is short circuited, and the current flows in a loop until it reaches zero (Fig. 3-10-c).

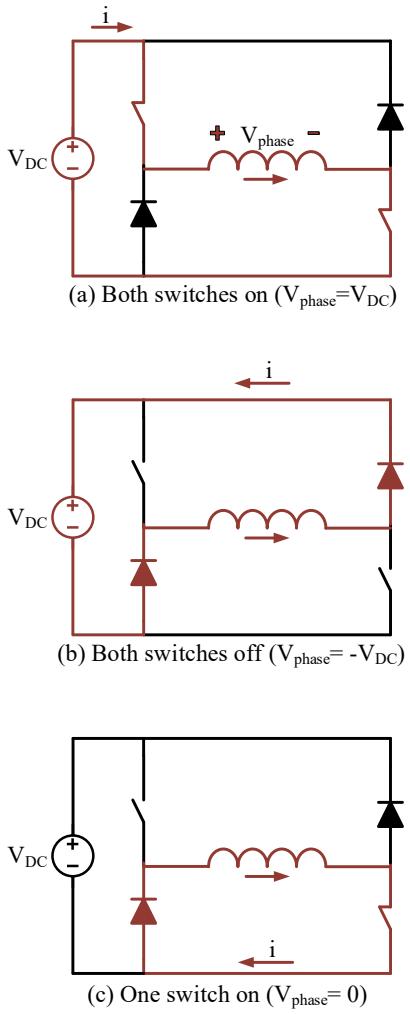

Fig. 3-10. Asymmetric bridge converter's different operating states.

Using an asymmetric bridge converter, the current of each phase can be independently controlled. The most straightforward method to control an SRM is setting a hysteresis current controller with conduction angles. The motor's performance, including average torque, torque ripple, and vibration, can be enhanced by optimizing the conduction angles.

3.4: Conclusions

SRM's robust, simple, and reliable structure, as well as its independence from the volatility of the permanent magnet prices, makes them good candidate for various applications. SRMs, however, may suffer from low power density, high torque ripple, and acoustic noise. However, these drawbacks can be mitigated through careful geometry and controls design. Moreover, these challenges of SRMs are not detrimental to the propulsion of light aircraft due to the nature of the load and the isolation of the cabin. In this chapter, the operating principles of SRMs are discussed. The torque production principal of an SRM is discussed using the magnetic field energy and co-energy. The equivalent circuit and instantaneous power are studied to express the relationship between airgap power and torque production. Finally, the control of SRM with asymmetric bridge converters is presented.

Chapter 4

4. Modeling and Analysis of Radial Force Density in Internal-Rotor Switched Reluctance Motors

4.1: Introduction

Switched reluctance motors (SRMs) are prone to acoustic noise and vibration due to their doubly salient construction. The electromagnetic forces exerted on the stator, especially those exerted radially, are one of the main sources of vibrations and acoustic noise in internal-rotor SRMs. Fig. 4-1 shows the decomposition of the forces exerted on the stator as radial and tangential forces. In rare instances (special geometries), the tangential force can impact the vibration and acoustic noise of the internal-rotor SRMs, too [38].

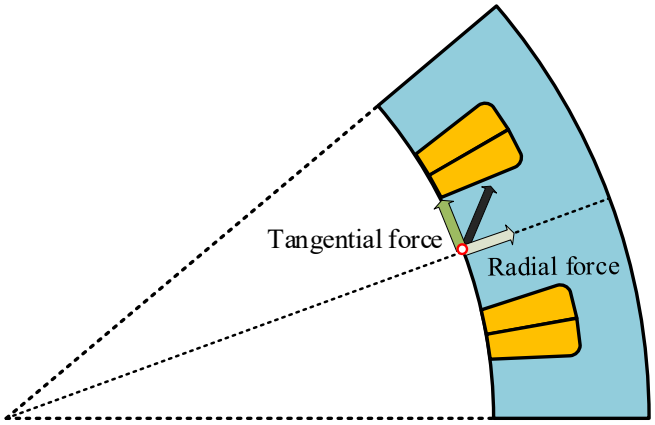

Fig. 4-1. Decomposition of stator electromagnetic forces in the radial and tangential direction.

In an SRM, radial force density harmonics is the main source of vibrations and acoustic noise. Using the radial force density harmonics and then the mechanical damping ratio, radiation factor, and natural frequencies for different mode shapes, it is possible to determine mechanical displacement (vibrations) and sound pressure level (SPL). Hence, reduction in radial force density harmonics could imply an improvement in the noise and vibration behaviour of the motor.

4.2: Radial Force Density in Switched Reluctance Motors

Utilizing the magnetic flux density in the airgap in the Maxwell Stress Tensor method, it is possible to calculate the radial force density on stator teeth. Temporal and circumferential periodicities reduce the computation time and memory requirements, and speed up the analysis. It is possible to decompose the radial force density into circumferential and temporal harmonics. The dominant harmonics can be used as objectives for motor design or control.

4.2.1: Calculation

For calculation of the electromagnetic forces based on the electromagnetic flux density, the Maxwell Stress Tensor method (4.1) can be used in the airgap:

$$\begin{pmatrix}\sigma_{r(t,\alpha)}\\ \sigma_{t(t,\alpha)}\end{pmatrix} = \frac{1}{2\mu_0}\begin{pmatrix}B^2_{r(t,\alpha)} - B^2_{t(t,\alpha)}\\ 2B_{r(t,\alpha)}B_{t(t,\alpha)}\end{pmatrix} \tag{4.1}$$

where σ_r is the radial force density, σ_t is the tangential force density, B_r is the radial magnetic flux density, B_t is the tangential magnetic flux density, α is the spatial position, t is time, and μ_0 is the magnetic permeability of the vacuum. Fig. 4-2 shows the typical position for airgap flux density measurement for the calculation of the radial force density with the Maxwell Stress Tensor method. For the measurement of magnetic flux density, typical airgap support arc radius is a quarter of airgap thickness away from the stator [39].

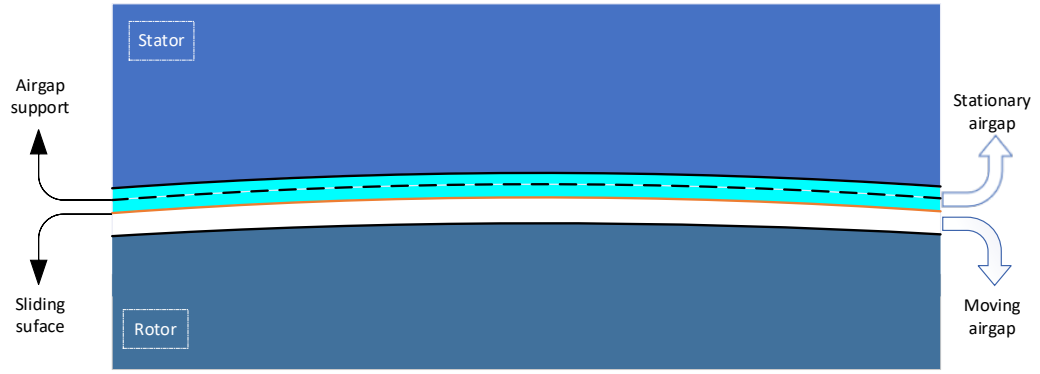

Fig. 4-2. Typical air gap support position for airgap flux density measurement for the calculation of the radial force density [39].

Radial forces should be measured in the entire circumferential position (α) or within a periodic circumferential position, as shown in Fig. 4-4, when the coils are excited by a dynamic current waveform. The dynamic current waveform should

be obtained by using the dynamic model of the SRM. Fig. 4-3 illustrates an example of the dynamic current waveform for one electrical cycle. The phase current waveforms and, hence, the magnetic field density and the radial forces are dependent on the motor control parameters. Notably, it is possible to simulate the radial forces of an SRM with a voltage source and an asymmetric bridge converter model in FEA. However, the simulation step time would be extremely small in that case, resulting in a long simulation time.

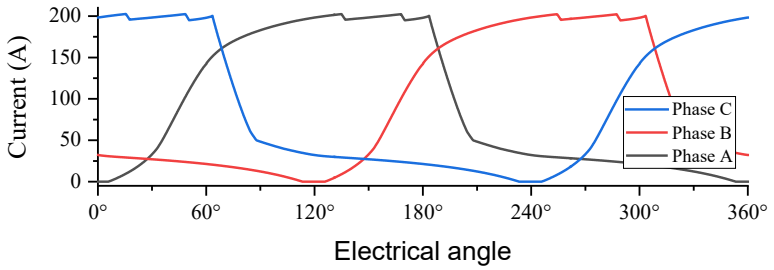

Fig. 4-3. Sample of the dynamic current waveform for a three-phase SRM.

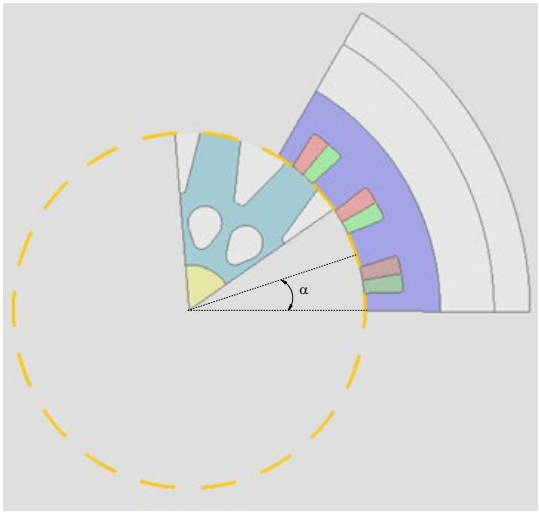

Fig. 4-4. Air gap support position for radial force measurement of an 18/12 SRM.

Fig. 4-5 illustrates the radial force density with the dynamic current excitation for a three-phase 18/12 SRM. In each electrical cycle, the radial force density has 18 peaks. The stator teeth, associated with the same phase, face the same radial force due to the same excitation. The shape of the radial force waveform is dependent on the motor geometry and the control parameters (e.g., conduction angles) [40].

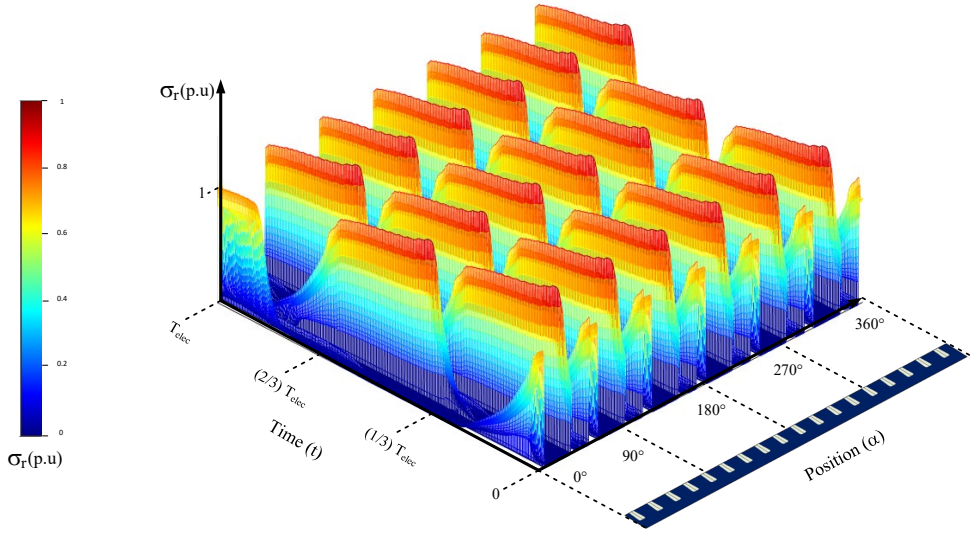

Fig. 4-5. Radial force density (stress) for an 18/12 SRM.

In order to simplify the representation of radial force density, it can be presented in a two-dimensional plot with a colour map, as shown in Fig. 4-6. The number of stators teeth associated with each phase can be calculated as the ratio of number of stator poles (N_s) and number of phase (m): N_s/m. Therefore, each phase produces six (N_s/m) peaks per electrical cycle in a three-phase 18/12 SRM.

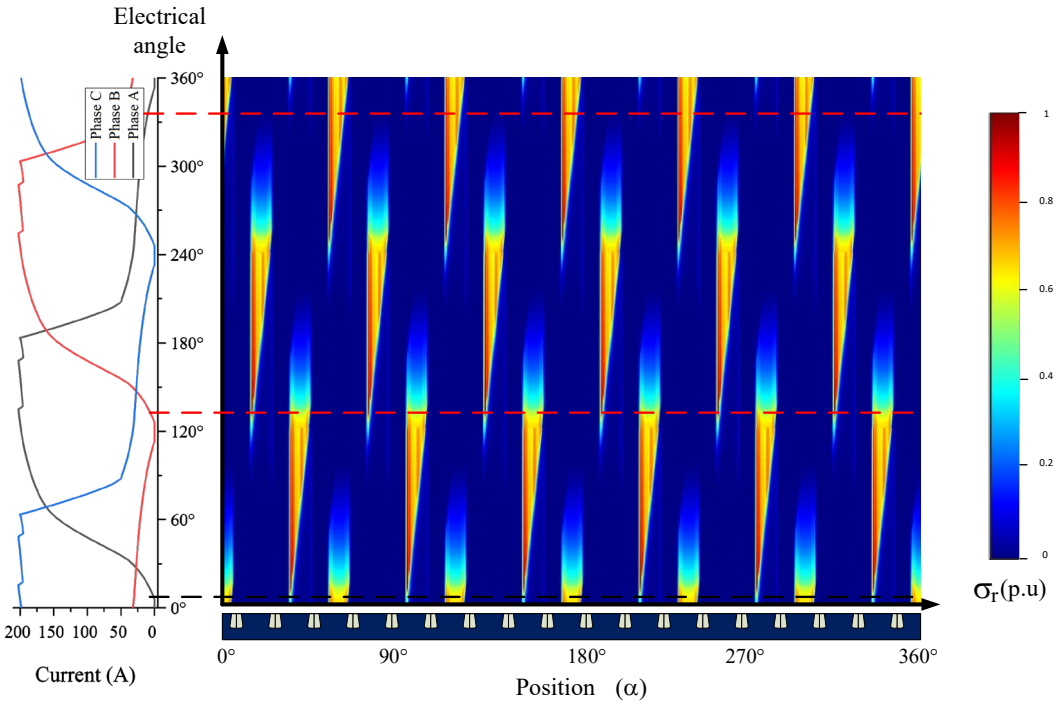

Fig. 4-6. Radial force density contour plot for an 18/12 SRM and the corresponding phase excitation waveforms.

4.2.2: Verification

The Maxwell Stress Tensor method in (4.1) calculates both the radial force density and tangential force density. Tangential force density creates the electromagnetic torque as it is in the direction of rotation. In order to verify that the Maxwell Stress Tensor method is utilized correctly and the calculation of the radial force density from the airgap magnetic flux density is accurate, the tangential stress calculated and then compared with the torque derived from magnetic co-energy. The torque waveforms obtained from the two methods should be the same, which indicates that the tangential force density calculation was accurate as well as the

radial force density calculation. Fig. 4-6 illustrates the torque production waveforms from the two methods. The torque obtained from tangential force density has a few dents because of the mesh size resolution. The number of mesh nodes in the airgap region is a trade-off between accuracy and simulation time. Overall, the results verify the accuracy of the radial force model.

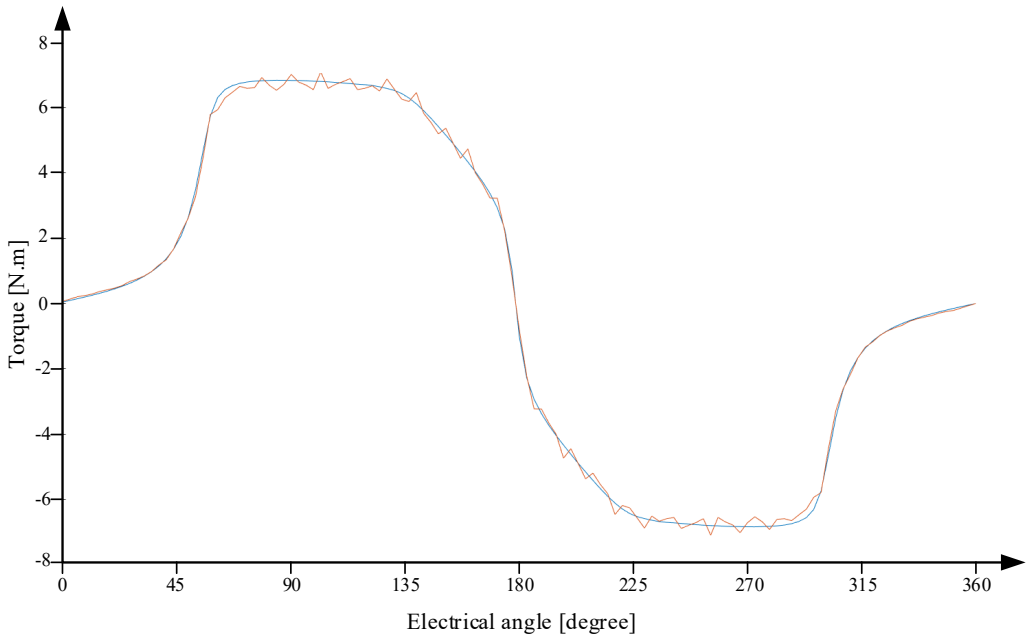

Fig. 4-7. The comparison of static torque with constant 20A excitation calculated by Maxwell stress and co-energy

4.2.3: Circumferential and Temporal Periodicity

Usually, a large number of simulations are necessary to analyze radial forces in a motor design process, and the simulation time can significantly impact the design framework. Hence, it is essential to use available periodicities to reduce the simulation burden.

In an SRM, the stator poles are evenly distributed between phases. Each phase excites N_s/m number of stator pole. Therefore, there is periodicity with a period of $360°/(N_s/m)$ in the circumferential domain. For instance, for an 18/12 SRM, the periodicity is for every 60° mechanical. Besides, the current waveforms of the different phases are usually identical in one electrical cycle but they are phase-shifted. For example, in a three-phase SRM, the currents of Phase B and Phase C are equal to the current of Phase A with 120° and 240° electrical angle phase shifts, respectively. As illustrated in Fig. 4-8, the radial force density can be calculated for only 360°/m electrical angle and for 360°/(Ns/m) mechanical angle. Then, this periodicity can be used to reconstruct the entire radial force density waveform. For a three-phase 18/12 SRM, using this periodicity reduces the simulation time by an order of eighteen times.

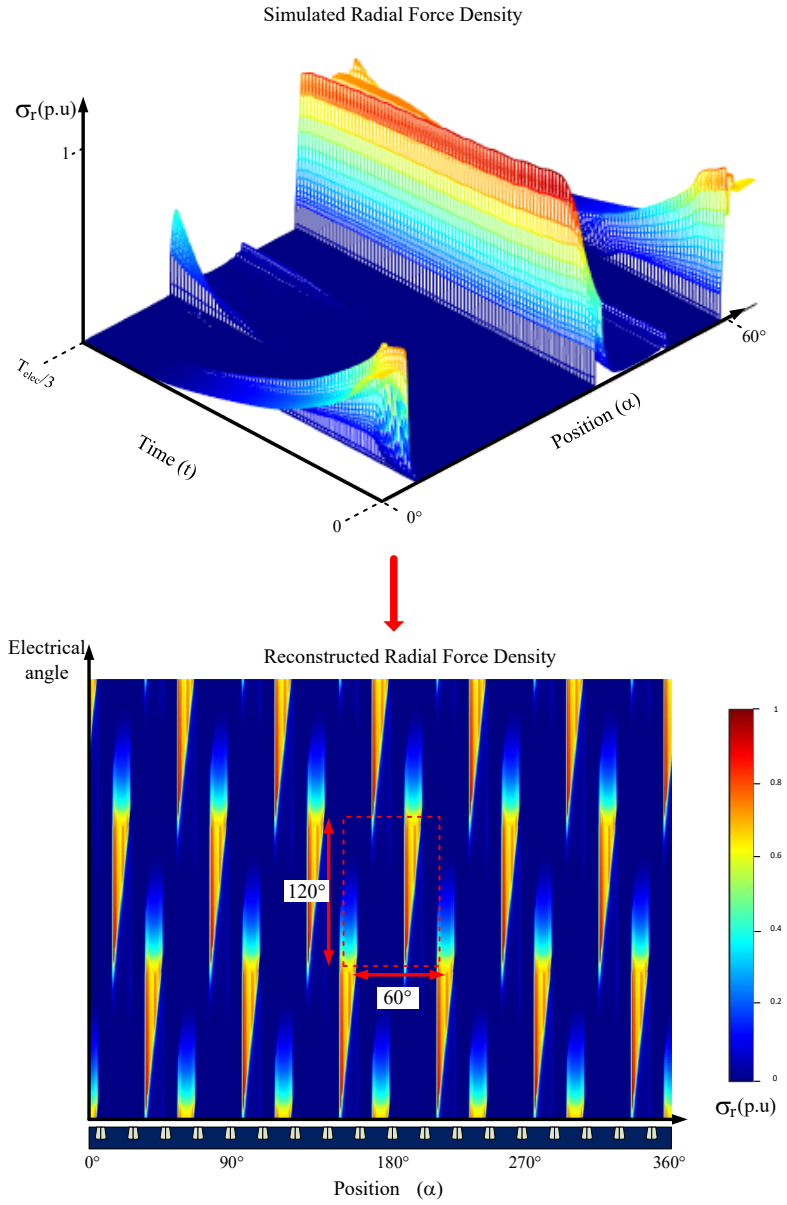

Fig. 4-8. Radial force density waveform for an 18/12 SRM by reconstructing it using mechanical and electrical periodicity.

4.3: Decomposition of Radial Force Density

The radial force density can be considered as a time- and spatially-varying surface waveform in a cylindrical shell representing the stator. The radial forces in

a cylindrical shell has three fundamental characteristics: (i) it changes over time or temporal domain, (ii) it changes over circumferential position, and (iii) it changes over axial position. The degree of deformation caused by the radial forces depends on the mechanical boundary conditions of the motor, such as the mounting specifications. In the proposed design process, axial deformation has not been considered to simplify the objective for radial forces, and only time and circumferential domains are taken into account. Only a two-dimensional electromagnetic analysis is performed rather than a three-dimensional electromagnetic analysis, and the results are approximated to be uniform across the axial length of the stator core (Fig. 4-9).

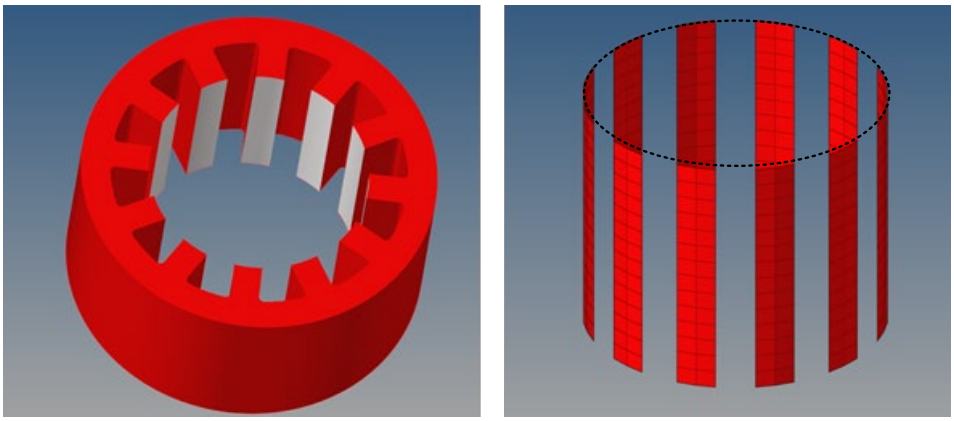

Fig. 4-9. The cylindrical shell for the radial force analysis.

4.3.1: Decomposition of Harmonics

Radial force behaviour may be analyzed by decomposing the radial force waveform into circumferential (spatial) and temporal harmonic components using (4.2) [41]:

$$f_r(t,\alpha) = \sum_{v=-\infty}^{\infty} \sum_{u=-\infty}^{\infty} \sum_{ax=1}^{\infty} \left(F_{r(u,v,ax)}\right) \approx \sum_{v=-\infty}^{\infty} \sum_{u=-\infty}^{\infty} \left(F_{r(u,v)}\right)$$
$$f_r(t,\alpha) = \sum_{v=-\infty}^{\infty} \sum_{u=-\infty}^{\infty} \left[|F_{r(u,v)}| \cos\left(\omega_{\text{mech}}\, ut + v\alpha + \theta_{(u,v)}\right)\right] \quad (4.2)$$

where the f_r is the radial force as a function of circumferential position, α and time, t. $|F_r|$ is the amplitude for harmonic order (u, v); where, u is the temporal order, v is the spatial order, ax is the axial order of the radial force harmonic. ω_{mech} is the mechanical speed, and θ is the phase angle for a given harmonic order (u, v).

4.3.2: Surface Wave in Cylindrical Shell

When decomposing the radial forces using (4.2), the forces are decomposed to harmonic contents as a function of circumferential position and time. For demonstration, a example surface waveform, f_{ex} in (4.3) with a single harmonic content based on time order *u* and spatial order *v* is used:

$$f_{ex}(t,\alpha) = |F_{ex}| \cos(\omega_{\text{mech}}\, u_{ex}\, t + v_{ex}\alpha + \theta_{ex}) \quad (4.3)$$

where $|F_{ex}|$ is the magnitude of the surface wave, u_{ex} is the temporal order (related to time), ω_{mech} is mechanical speed, v_{ex} is the spatial order (related to position), θ_{ex} is the phase angle, t is time, and α is the spatial position. By using the mechanical frequency, f_{mech}, instead of mechanical speed, the expression can be expressed as:

$$f_{ex}(t,\alpha) = |F_{ex}| \cos(2\,\pi\, f_{\text{mech}}\, u_{ex}\, t + v_{ex}\alpha + \theta_{ex}) \quad (4.4)$$

To better understand the example surface wave, $f_{ex}(t, \alpha)$ in (4.4) can be illustrated with a three-dimensional plot as a function of the mechanical position (α) and time (t). As shown in Fig. 4-10, the spatial position (α) can be interpreted as the linear axis in the two-dimensional waveform.

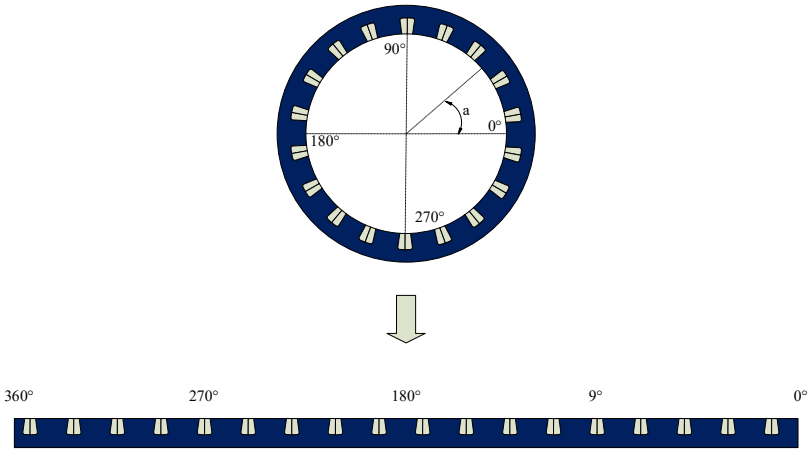

Fig. 4-10. Clarification of spatial angle as a linear axis.

A surface wave, $f_{ex}(t, \alpha)$ with magnitude $|F_{ex}| = 1$, spatial order, $v_{ex} = 2$, temporal order $u_{ex} = 3$, and phase angle $\theta_{ex} = 0$ is expressed by:

$$f_{ex}(t, \alpha) = |1| \cos(3\ \omega_{\text{mech}}\ t + 2\ \alpha + 0). \tag{4.5}$$

Fig. 4-12 shows the example surface waveform in a three-dimensional plot. The horizontal plane is the spatial position, α and time, t. The vertical axis and colour legend is the instantaneous value of the force magnitude, f_{ex}. The spatial order means that in every given time, there are two spatial positions with the maximum value of the waveform, and the periodicity of the wave is half of the circumference $360°/v$. A temporal order $u_{ex} = 3$ implies that each specific spatial position encounters the maximum value of waveform three times per mechanical

cycle; thus, the periodicity is equal to one-third of the mechanical period T_{mech}/u. The top view of the waveform with colour mapping can be used instead of a three-dimensional view for a more straightforward illustration, as shown in Fig. 4-11.

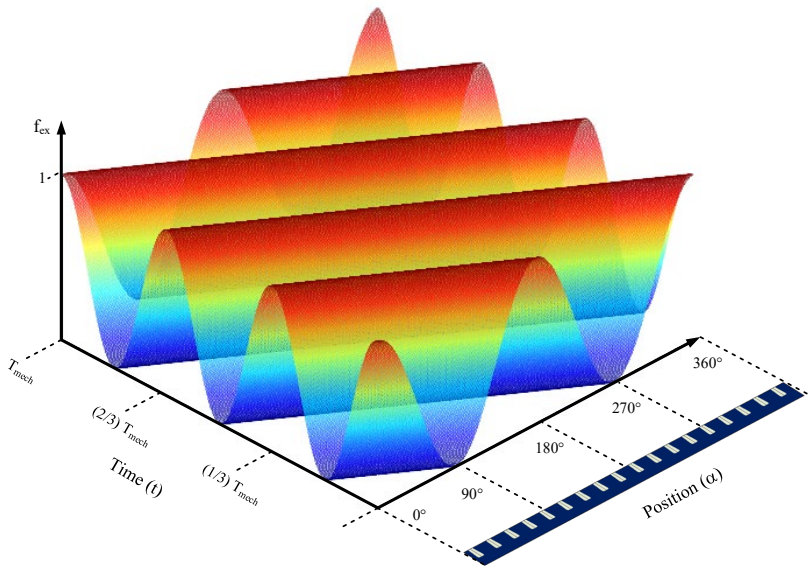

Fig. 4-11. Surface waveform example with spatial order two and temporal order three (three-dimensional view).

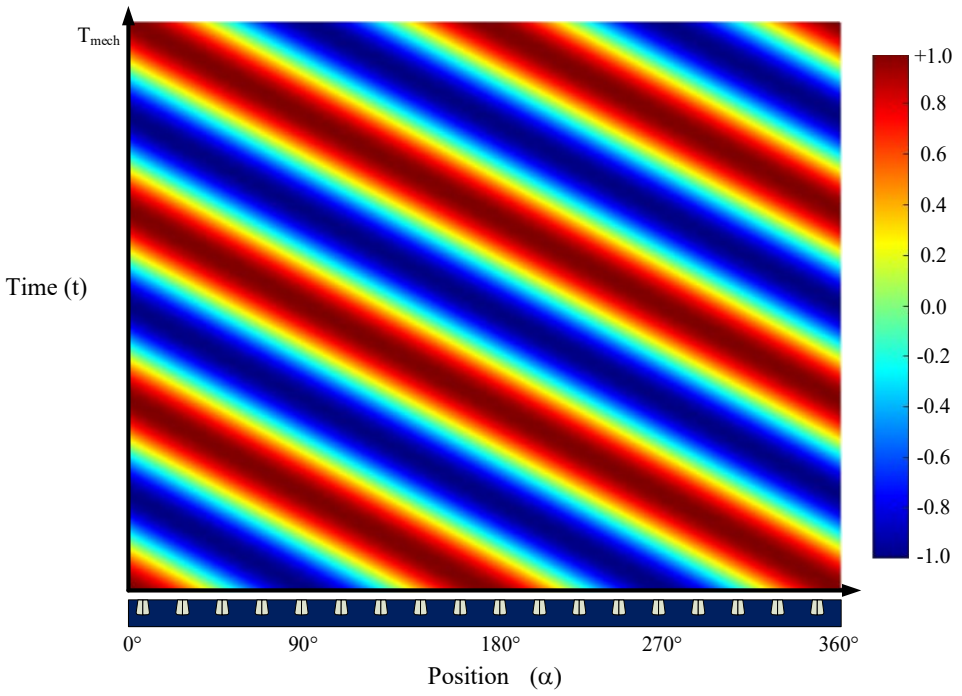

Fig. 4-12. Surface waveform example with spatial order two and temporal order three (top view).

4.3.3: Temporal Orders

If we consider a specific spatial position, the temporal order can be determined by the number of oscillations over one mechanical cycle (T_{mech}). For example, the two-dimensional waveform for spatial order $v_{ex} = 2$ with temporal order $u_{ex} = 3$ and $u_{ex} = 5$ are plotted in Fig. 4-13 and Fig. 4-14, respectively. In every T_{mech}, the waveform with temporal order $u_{ex} = 3$ alters from peak-to-peak three times, and the waveform with temporal order $u_{ex} = 5$ alters from peak-to-peak five times.

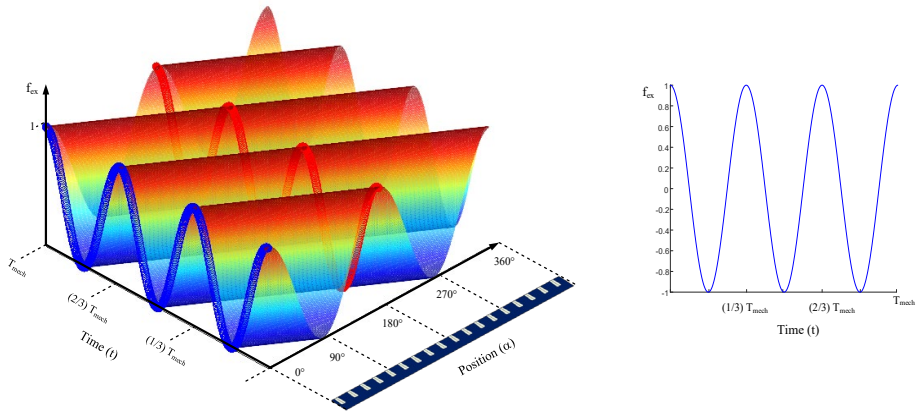

Fig. 4-13. Harmonic content example with temporal order three.

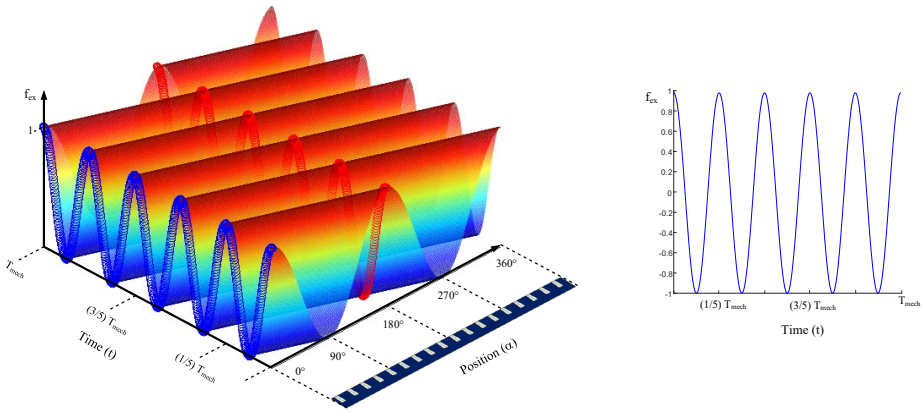

Fig. 4-14. Harmonic content example with temporal order five.

The temporal order is based on the mechanical period, which depends on the motor's mechanical speed. To express the relationship between the mechanical speed, ω_{mech} and the temporal order, u the forcing frequency is defined as:

$$f_{f(u)} = |u| f_{\text{mech}} \tag{4.6}$$

where $f_{\text{f(u)}}$ is the forcing frequency, f_{mech} is the mechanical frequency, and $|u|$ is the absolute value of the temporal order. The forcing frequency increases linearly with the mechanical speed as shown in Fig. 4-15. The difference in

the speed of the motor changes the forcing frequency and, hence, the radial force harmonics can get closer or further away from the natural frequency of the corresponding mode shape impacting the vibration and noise characteristics of the motor.

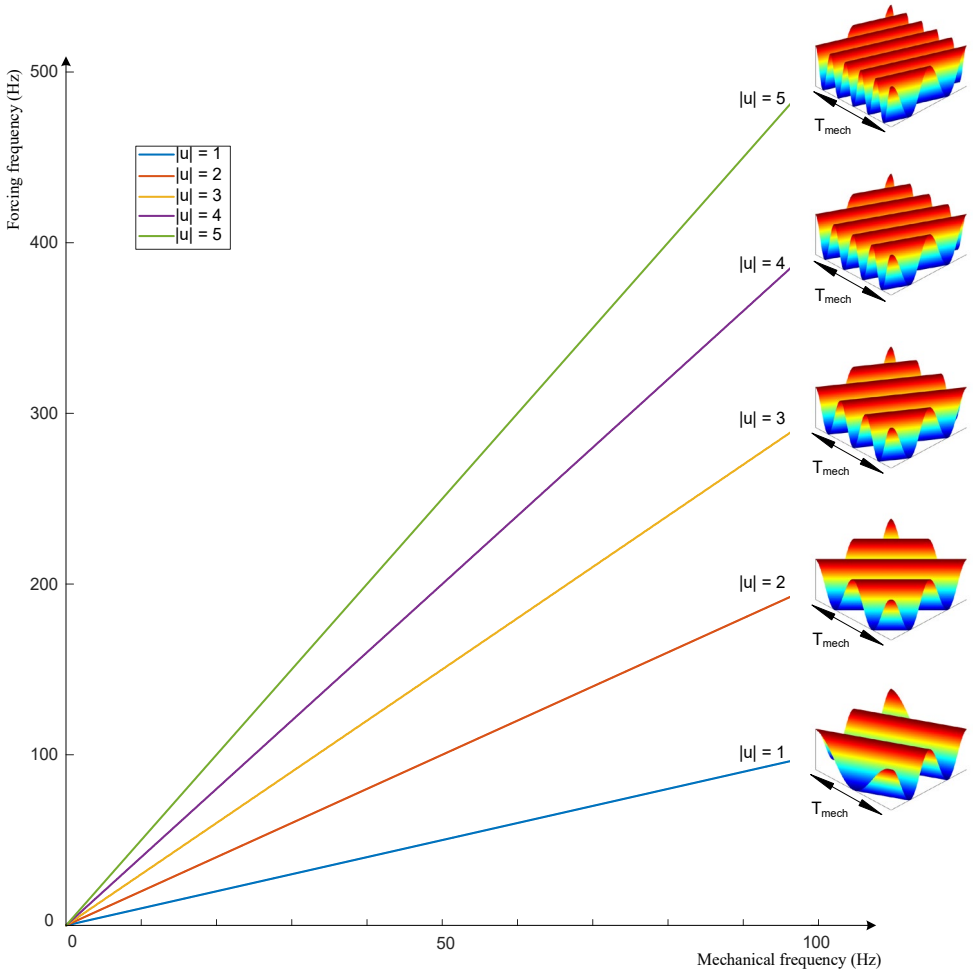

Fig. 4-15. Relationship between forcing frequency, and mechanical frequency and temporal order.

4.3.4: Spatial Orders

At every given time, the spatial order is determined by the number of oscillations over the stator circumference. For example, the surface wave for spatial order $v_{ex} = 2$ with temporal order $u_{ex} = 3$ is shown in Fig. 4-16. In every time instance, the maximum force occurs in two positions ($v = 2$). For every $t = k\,T_{mech}/3$, where k is a positive integer starting from zero, the maximum value of the waveform is at 0° and 180° in the spatial domain. This was demonstrated with a blue line in Fig. 4-16. The surface wave function is expressed as follows when t is substituted in (4.5):

$$f_{ex}(t,\alpha)|_{t=k\,T_{mech}/3} = \cos(2\,\alpha). \tag{4.7}$$

For another time instance, when $t = (k + 0.5)T_{mech}/\,3$, where k is a positive integer starting from zero , the maximum value of the wave will be at 90°, and 270° circumferential like the red line instance in Fig. 4-16; based on (4.5), the equation (4.8) expressed the relation ship as:

$$f_{ex}(t,\alpha)|_{t=(k+0.5)\,T_{mech}/3} = \cos(\pi + 2\,\alpha) \tag{4.8}$$

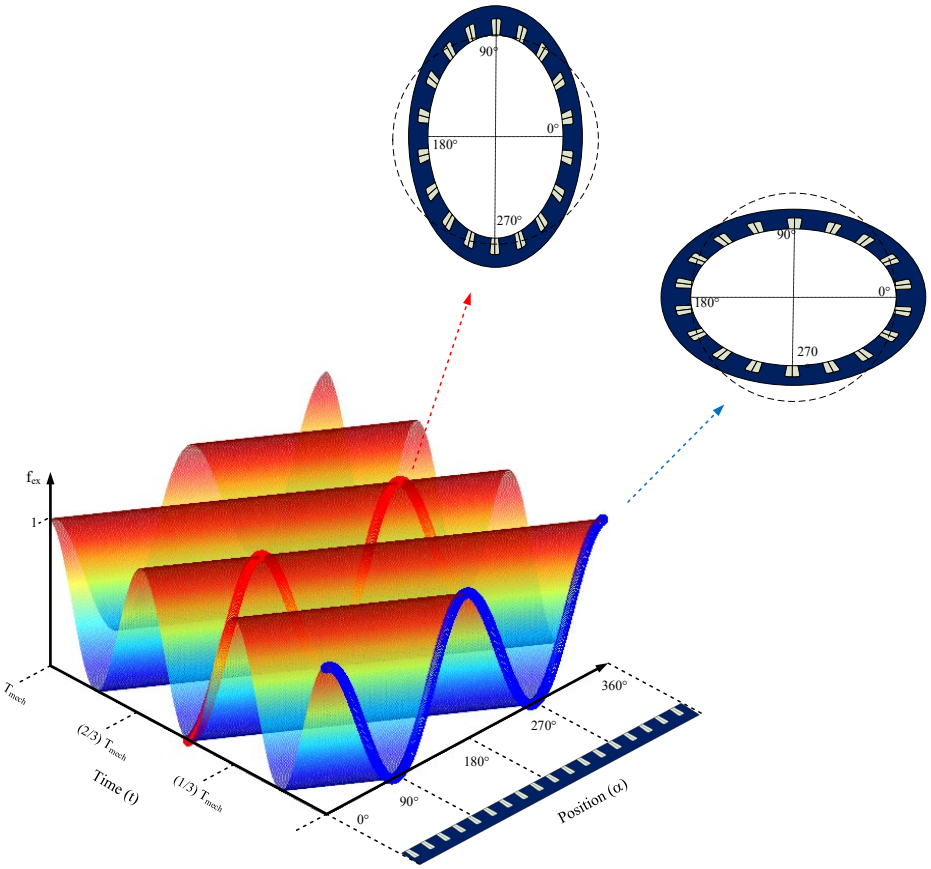

Fig. 4-16. Surface waveform with temporal order $u_{ex} = 3$ and spatial order $v_{ex} = 2$ The waveforms with respect to spatial position are highlighted at $t = k\,T_{mech}/3$ (blue) and $t = (k + 0.5)T_{mech}/\,3$ (red).

The spatial order can be different in the number of peaks per circumference. In Fig. 4-17, the spatial mode shapes from zero to seven are illustrated for a cylindrical shell. A cylindrical shell (stator) in mode zero contracts and expands equally along its circumference, so its shape is a concentric circle. When $v = 1$, the cylindrical shell shape becomes an eccentric circle. For $v = 2,$ it becomes an oval shape. As the absolute value of v increases, the number of peaks increases as well.

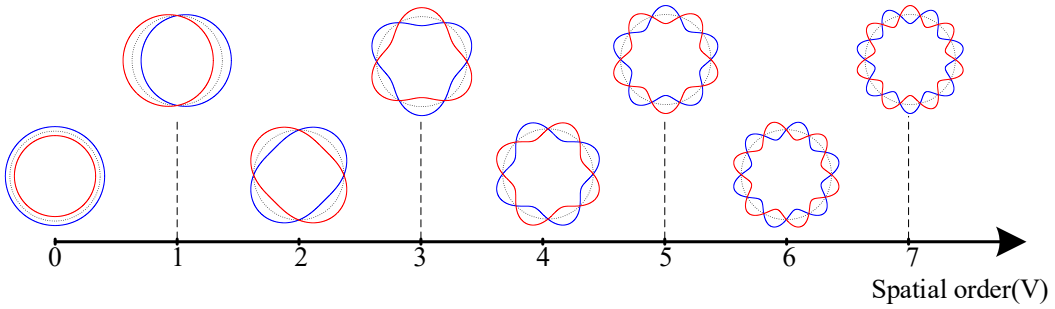

Fig. 4-17. Circumferential mode shapes for a cylindrical shell for spatial order zero to seven.

4.3.5: Four-Quadrant *u-v* Coordinate System and Direction of Rotation

The decomposition of the radial force waveform into temporal and spatial harmonics was quantified in (4.2) as

$$f_r(t,\alpha) = \sum_{v=-\infty}^{\infty} \sum_{u=-\infty}^{\infty} \left[|F_{r(u,v)}|\cos\left(\omega_{\text{mech}}\, ut + v\alpha + \theta_{(u,v)}\right)\right].$$

Each harmonic content act like a surface wave. The harmonics can be illustrated in four-quadrans *u-v* coordinate system. Based on the position of a harmonic content in the *u-v* coordinate system and the motor specifications, the surface waveform for that harmonic has a certain rotation direction. The signs of the temporal and circumferential orders define the rotation direction of the harmonic content. When the signs of the temporal and spatial orders are the same, the surface waveform of that harmonic rotates clockwise (negative rotation). When the signs of the temporal and spatial order are opposite, the rotation is in the counter-clockwise direction (positive rotation). Fig. 4-18 depicts the rotation regions in different quadrants of the *u-v* coordinate system.

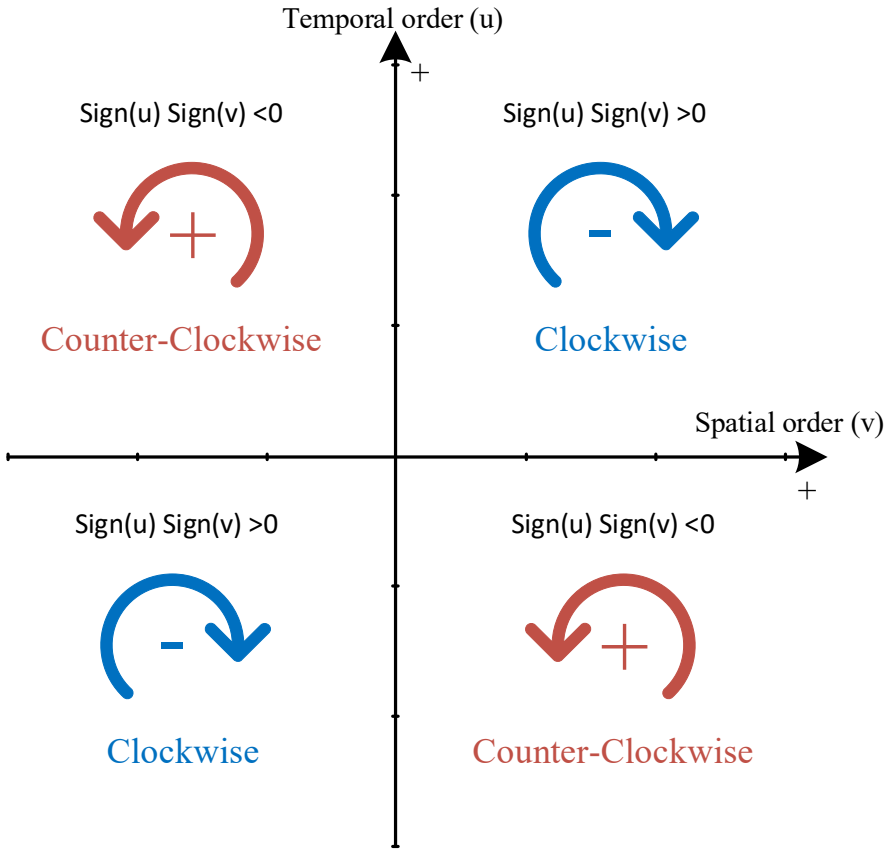

Fig. 4-18. The rotation direction of harmonic content in the u-v coordinate system.

To better illustrate the rotation direction, a three-dimensional waveform with three consecutive time instants (t_1, t_2, t_3) is plotted in Fig. 4-19 for spatial order $v = +2$ with temporal orders $u = \pm 4$. In the first quadrant in Fig. 4-19, the position of the maximum value of the surface waveform moves in the negative direction of the spatial position, α. For instance, Fig. 4-19 illustrates that, at the three consecutive time instants (t_1, t_2, t_3) surface waves move in a negative direction at their peak for spatial order $v = +2$, and temporal order $u = +4$. In the fourth quadrant, the position of the maximum value of the surface waveform moves in the positive

direction of the spatial position, α. For instance, Fig. 4-19 illustrates that, at the three consecutive time instants (t_1, t_2, t_3), surface waves move in a positive direction at their peak for spatial order $v = +2$, and temporal order $u = -4$.

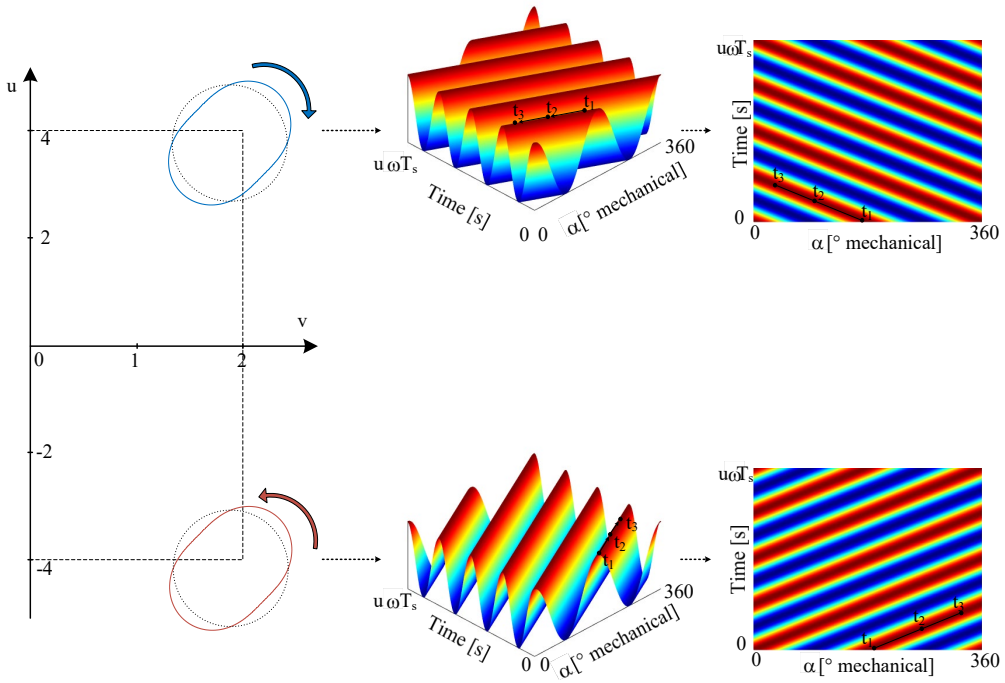

Fig. 4-19. Illustration of the harmonic content's rotation direction with three consecutive time instants (t_1, t_2, t_3).

The radial force harmonics contents are not only limited to the four quadrants discussed in the Fig. 4-18. As shown in Fig. 4-20, the radial force harmonic content in the *u*-*v* coordinate system are scattered in different quadrants and they can also be located on the axes. Some of them can be on the temporal axis ($v = 0$), where the magnitude of all circumferential positions are the same. Conversely, for any given spatial position, the harmonics on the spatial axis (u=0)

have the same radial force at any time. It is possible to reduce the number of harmonic content through the superposition of harmonics. A comprehensive description of the superposition conditions can be found in [42].

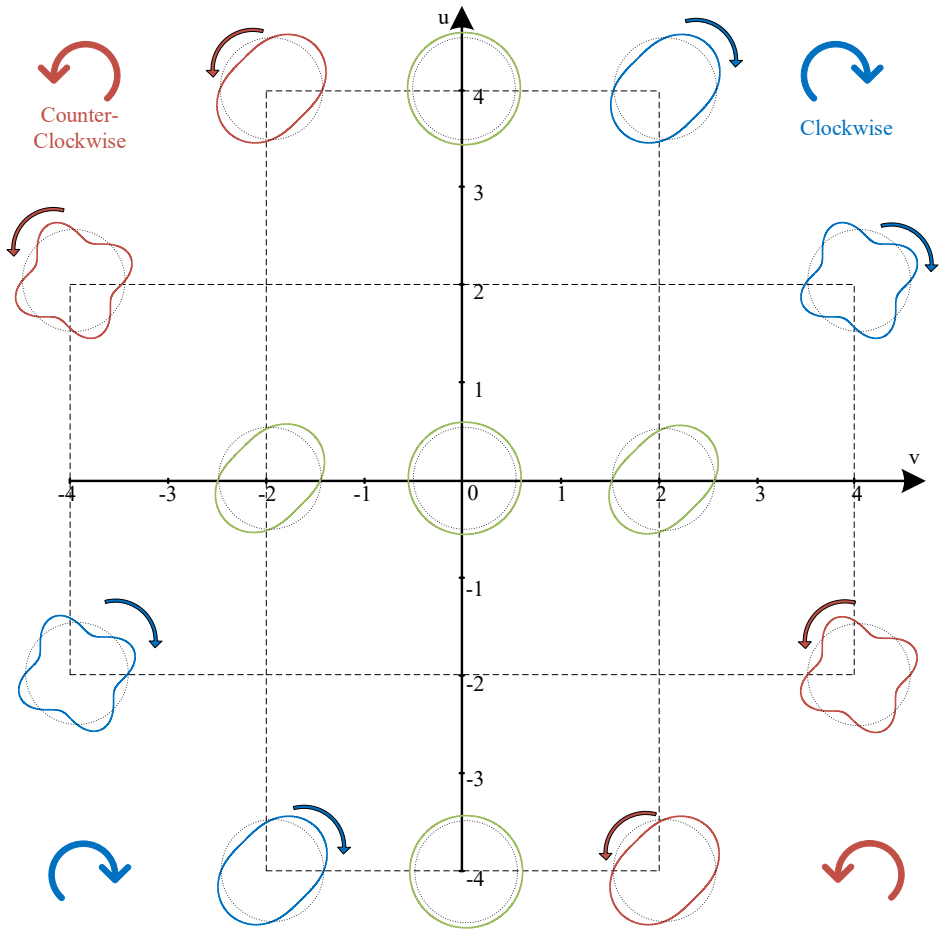

Fig. 4-20. Example harmonic content shapes and rotation directions for selected orders in four quadrants u-v coordinate system.

4.4: Radial Forces Density Decomposition of an 18/12 Switched Reluctance Motor

The position of harmonic contents of the radial force density in the u-v coordinates system varies depending on the number of phases, m, the number of stator poles, N_s and the number of rotor poles, N_r . Equations (4.9) and (4.10) define the dominant harmonic orders an 18/12 SRM, where j, and k are integers [38]. Fig. 4-21 shows the decomposition of radial force density for an 18/12 SRM using 2D FFT. The position of harmonics are consistent with the calculations from (4.9) and (4.10).

$$v = \frac{Ns}{m}k = \frac{18}{3}\,k = 6k. \tag{4.9}$$

$$u = N_r\,(mj + k) = 12\,(3j - k) = 36j - 12k. \tag{4.10}$$

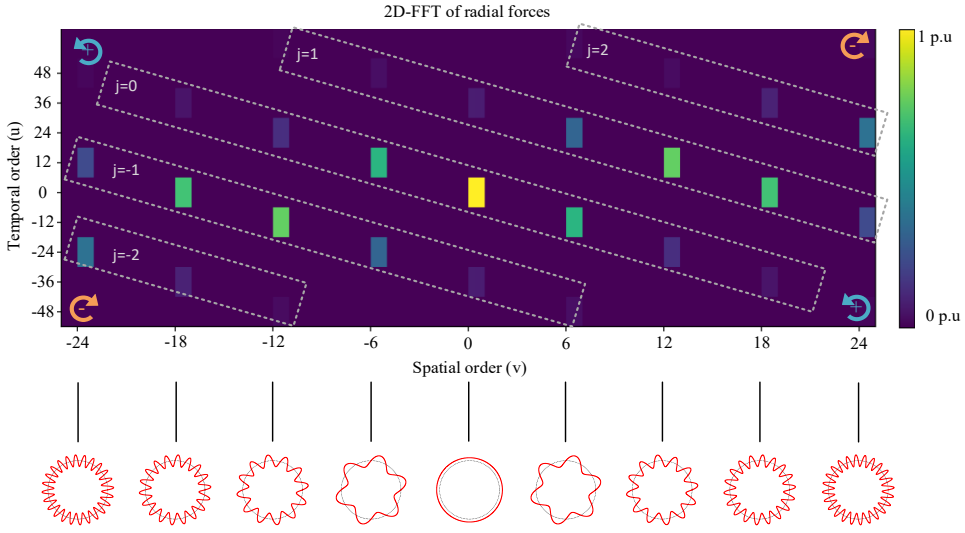

Fig. 4-21. Amplitudes of dominant harmonic content of radial force density of a three-phase 18/12 SRM.

4.5: Conclusions

One of the main sources of vibration and acoustic noise in internal-rotor SRMs is the radial electromagnetic forces exerted on the stator. Electrical motor design projects should aim to minimize vibrations and acoustic noise, thereby reducing radial forces. The Maxwell Stress Tensor method is used to calculate the electromagnetic forces exerted on the stator. A comparison of torque production from tangential forces and torque production from magnetic co-energy has been demonstrated as a verification for radial force calculation. By using periodicities, the simulation time has been reduced by order of the number of stator poles (Ns). The radial force density waveform from the dynamic current excitation is decomposed to temporal and spatial harmonics. It is demonstrated how to interpret the temporal and spatial orders (*u* and *v*) of harmonic contents. The harmonic contents and rotation direction are indicated using a *u*-*v* coordinate. An analysis of the radial force density for an 18/12 SRM is executed, and the presentation of the harmonics' positions in the *u*-*v* coordinate system is illustrated.

Chapter 5

5. Multi-objective Design Framework for the Design of the Light Sport Aircraft Switched Reluctance Motor

5.1: Introduction

SRM geometry and control optimization has gained considerable attention in recent years. SRM optimization has been studied in both stochastic and deterministic forms [43]. The primary performance measures include torque density [44], [45], efficiency [45], [46], torque ripple [47], [48], and radial forces [49], [50], [51] have been the subject of studies on geometry design. Generally, the main focus of the control optimization is on torque ripple reduction [52]-[54] and radial force reduction, which results in reduced vibration and noise [40], [55].

There is a close relationship between the motor geometry design and the control strategy, but the effect of control is usually neglected in the geometry design process. Every geometry is assigned an optimal control parameter, but to simplify

the design process, the control parameters or the shape of the phase current waveform have either been set by experience or by heuristic curves which may or may not be optimized for each geometry combination. Some researchers have proposed that combining control and geometry design can be useful [56], [57]. However, they used either a simplified control design or a less accurate electromagnetic model (e.g. an equivalent magnetic circuit) as a motor model. Due to the highly nonlinear nature of SRMs, these less-accurate motor models may not be effective to model for every variation in the geometry. Additionally, they are not optimizing for radial forces, which is an important performance indicator for the motor in terms of vibration and acoustic noise.

In the light-sport aircraft (LSA) application, a high torque density is targeted, and the effect of the control parameter cannot be neglected. In this chapter, the proposed multi-objective design framework for the LSA SRM is presented. The proposed framework consists of two main stages: (i) static analysis and design, and (ii) dynamic analysis and design. The author recommends that before implementing the framework, one should perform an initial design to examine the motor's parameters and gain some insight into the correlations. The proposed design framework does not require this initial step, but it helps the less experienced designer gain a deeper understanding of the motor parameters.

The first step of the framework is the design of the motor based on static characteristics. The purpose of this layer is to identify all geometry combinations with a high static average torque. The geometry combinations are clustered and put

through the next layer of the framework, the dynamic design stage. The dynamic design stage's objective is to increase the average torque, and reduce radial forces and torque ripple. A dynamic design is composed of a control and geometry optimization loop. In each loop iteration, the deterministic optimization algorithm tries to find the best geometry around the current geometry, and the limited boundary of changes limits the variation of the optimum control parameters. The best geometry design is selected as the final design after applying the dynamic design to all of the high static average torque combinations.

5.2: Static Analysis and Design

The static characteristic of an SRM refers to its performance under a single-phase constant-current excitation. The static design aims to identify the geometry combinations that have the best static performance, such as high average torque and low induced voltage. The mutual coupling between phases is normally ignored in SRM design. In the static performance, the mutual coupling is not taken into account. In dynamic optimization in the next step, the mutual coupling and torque ripple due to dynamic current are taken into account. As a precaution, the static design should be performed using nominal current and low current. The low current static optimization is important to ensure the maximum induced voltage is limited in all current ratings.

The static design process consists of several steps, as depicted in Fig. 5-1. First, a fast parameterized model is defined, and then an extensive design of experiment (DOE) is performed. The results are fitted with two nonlinear surrogate

models and then optimized with three different global optimization algorithms to ensure the geometry combination list is as inclusive as possible, and the chances of missing good geometry combinations are low. After the optimization, the list undergoes a validation process with a higher-fidelity finite element model to ensure the surrogate models were accurate.

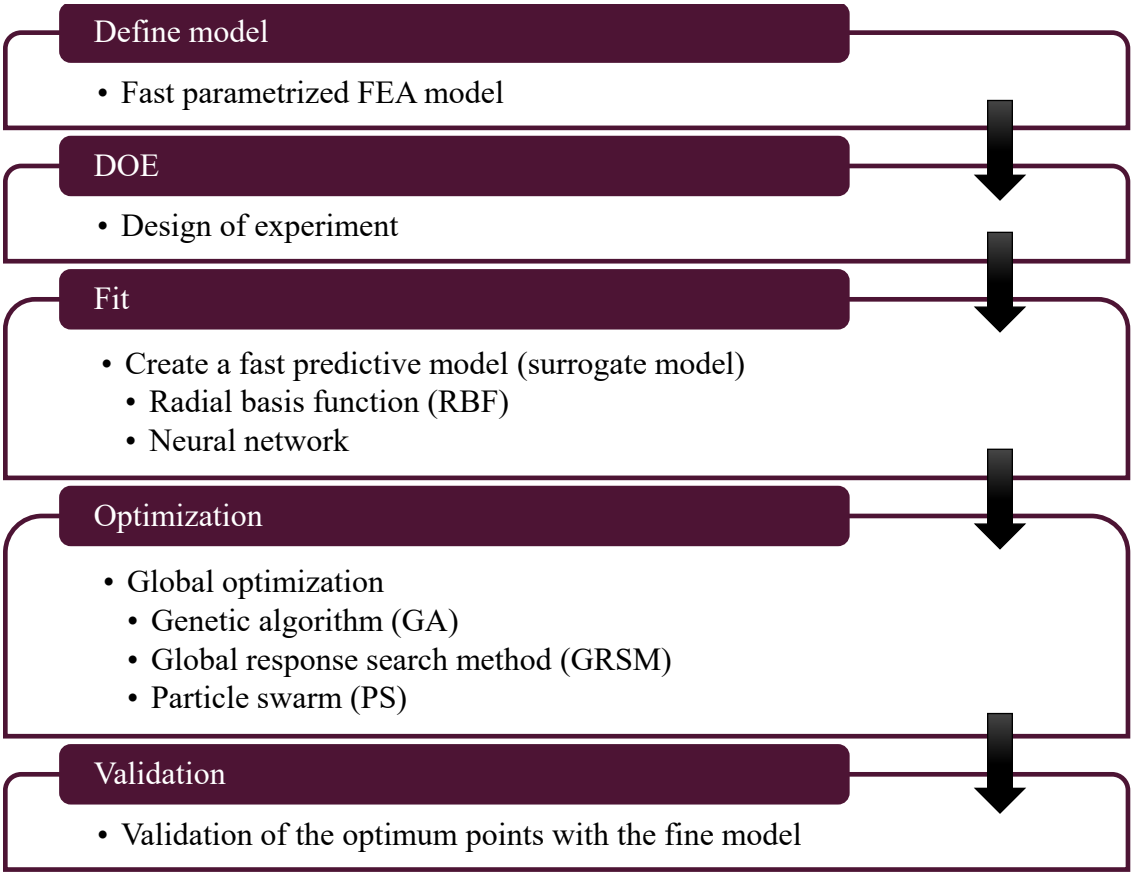

Fig. 5-1. The steps of the static design process in the proposed SRM design framework.

5.2.1: Definition of Fast Finite Element Analysis Model with Constant Current Density Coils

For geometry design and optimization, there is a need to have a fast parametric FEA model of the motor. The motor parameters can be categorized into geometry parameters and coil parameters. The coil parameters add more variables to the design of the motor, which can increase the design time. Additionally, the correlation between the slot area, fill factor and current density complicates the design process. According to Ampere-Maxwell's law, the magnetic field intensity, H is related to the current density, J:

$$\nabla \times \vec{H} = \vec{J} \tag{5.1}$$

In an electric motor, magnetomotive force, MMF is generated by the coil current, I that flows through the coil turns, N_{turns}. The product of the number of turns and coil current can be rewritten as the product of slot area, A_s, copper fill factor, ff, and current density, J:

$$MMF = N_{turns} I = J\, A_s\, ff\,. \tag{5.2}$$

The magnetic flux density, B is related to the equivalent permeability of the electromagnetic circuit, μ and magnetic field intensity. Based on (5.1), the magnetic field intensity is related to the current density. Therefore, the magnetic flux density is related to the product of equivalent permeability and current density, which is defined as,

$$G_B = J\, \mu\,. \tag{5.3}$$

The torque production is dependent on the product of magnetic flux density and magnetomotive force, which can be defined as,

$$G_T = MMF\ G_B\ . \tag{5.4}$$

By substituting (5.2) and (5.3) into (5.4), torque production expression can be simplified as:

$$G_T = ff A_s J^2 \mu\ . \tag{5.5}$$

Hence, if the fill factor, current density, and area of the two different coil designs are the same, the resulting torque production would be the same. In addition, if the resistive losses are neglected, the induced voltage will be the same for both coils. Therefore, a constant current density region can be used instead of a coil region with certain number of strands, the number of turns, magnetic wire size, and coil pattern. In order to illustrate the similarity between different coil designs and the current density region, four different coil patterns and constant current density regions with the same current density, fill factor, and slot area are simulated. The coil parameters of each design are listed in Table 5-1. The different coil designs have different wire sizes, the number of turns and the number of strands. Even with all the differences in the coil windings, because the slot area, fill factor, and current density are the same, the results in static torque and induced voltage are the same for all of them, as shown in Fig. 5-2 and Fig. 5-3.

Table 5-1. Verification coil parameter strategy

Winding pattern	**Magnet wire American Wire Gauge (AWG)**	**Number of turns**	**Number of strands**	**Fill factor**	**Current density (A/mm^2)**
6s	17	15	7	0.597	25.42
2p3s	20	30	7	0.595	25.47
3p2s	21	45	6	0.607	24.97
6p	21	89	3	0.601	24.97
Constant current density region				0.6	25

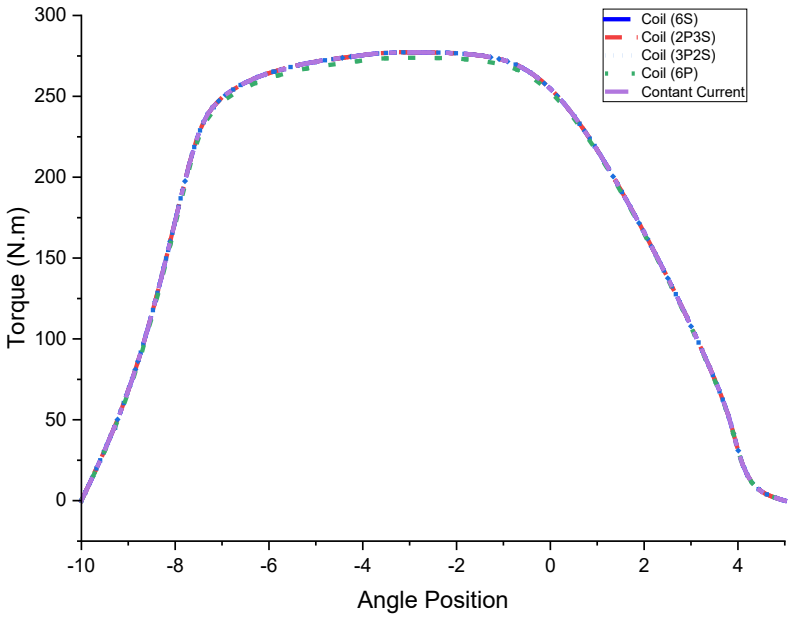

Fig. 5-2. Comparison of static torque for different coil parameters to verify the model definition.

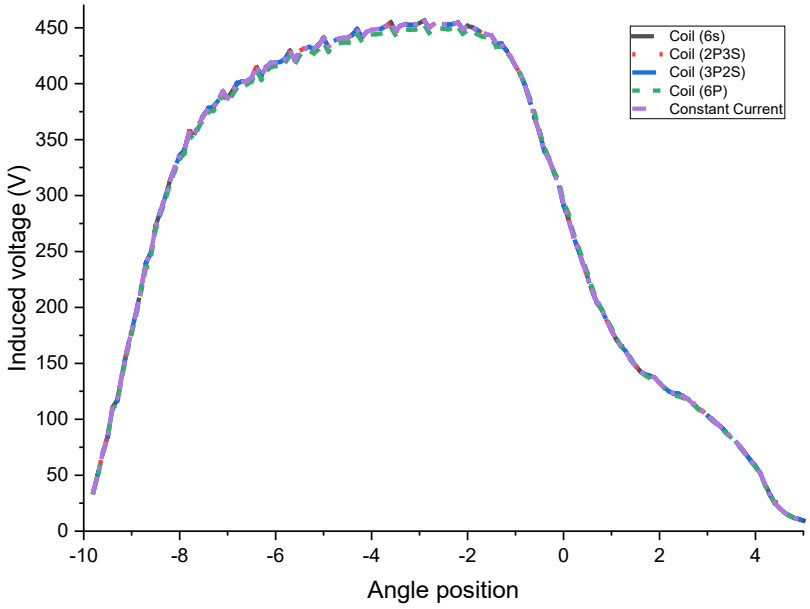

Fig. 5-3. Comparison of static induced voltage for different coil parameters to verify the model definition.

By using a constant current density region instead of conventional stranded coils, there is no need to define any constraint on the current density and fill factor. This will reduce the possibility of convergence of the geometry with extreme current densities or fill factors. An example of that poor convergence is graphically illustrated in Fig. 5-4, the area of the slot is reduced by changes in the stator pole arc angle and, hence, the fill factor and current density are extreme and impossible to achieve.

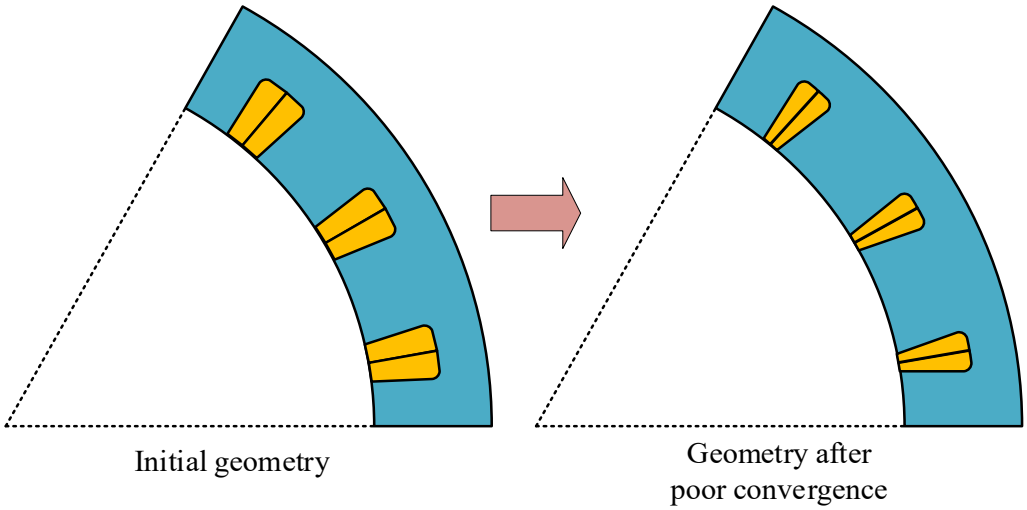

Fig. 5-4. An example for demonstrating poor convergence of the geometry.

There are plenty of different parameters for the geometry parameters that can be selected as the design parameter. Based on the insights of the initial design and a primitive calculation of correlations with a simple DOE, a set of geometry parameters are selected for the design process for the highest correlation with torque and induced voltage. The selected parameters, as illustrated in Fig. 5-5, are different diameters and the pole arc angles. As shown in Table 5-2, the rotor outer radius, $R_{1,}$ and slot inner radius, $R_{2,}$ have the highest impact on the average torque; due to their direct effect on the rotor radius and stator slot area. Pole arc angles mainly change the shape of the torque production, which is more important in the torque production capability of the motor with dynamic excitation. The taper and fillet angles are not considered in this level of optimization to simplify the process. The air gap length is defined by the motor's speed and power rating.

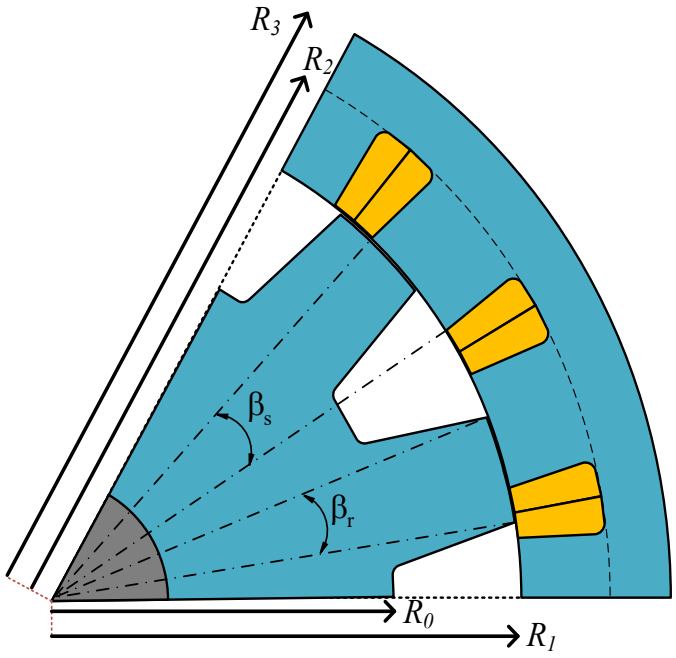

Fig. 5-5. Geometry variables for static optimization.

Table 5-2. Correlation of geometry parameters with static torque

Geometry parameters	**Average static torque**	**Maximum static torque**
β_r (rotor pole arc angle)	0.09	0.15
β_s (stator pole arc angle)	-0.08	-0.35
R_0 (rotor inner radius)	-0.02	-0.03
R_1 (rotor outer radius)	-0.51	-0.5
R_2 (slot inner radius)	0.68	0.68
R_3 (stator outer radius)	0.10	0.08

5.2.2: Design of Experiment and Fitting for the Surrogate Model

With the FEA model prepared in the previous section, two comprehensive designs of experiment (DOE) are performed for two different currents. One of them should be with the motor's nominal current, and the other should be with a lower current, less than half of the nominal current, based on the author's experience with this motor design. The reason behind using two different currents is to ensure that the motor's saturation is not reducing the induced voltage artificially in the high current static simulations. As shown in Fig. 5-6, the initial flux linkage increases for the high current excitation; therefore, the slope of the flux linkage reduce with the high current excitation ($\phi_2 < \phi_1$). Hence, based on Faraday's law, the induced voltage is lower for a smaller flux linkage slope.

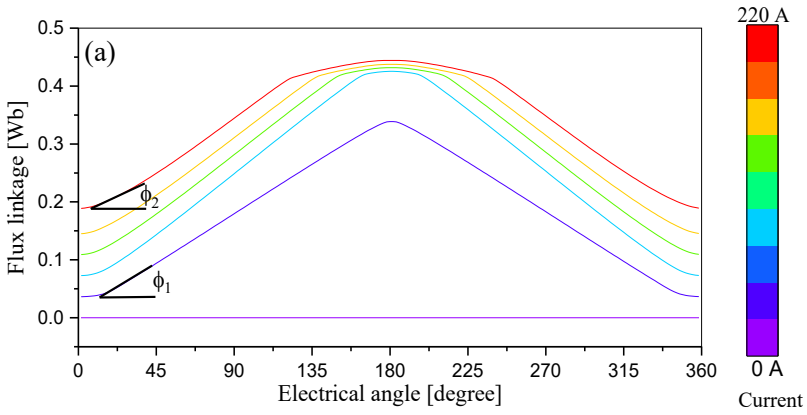

Fig. 5-6. Flux linkage slope difference for high current excitation.

A DOE with a high number of different input geometry combinations is performed with the multi-execution of the FEA model in the Altair HyperStudy environment. The input parameters are selected uniformly with an extensible lattice

sequence. This sequence reduces the clumps and empty spaces in the input parameters of the DOE. An example of the DOE with 900 different input parameters is illustrated in Fig. 5-7. Each line connects the input parameters of an experiment to the output of that experiment. For instance, the golden line in Fig. 5-7 is one of the experiment instances with labelled geometry parameters (β_r, β_s,R_0,R_1,R_2,R_3) and the resulting average torque.

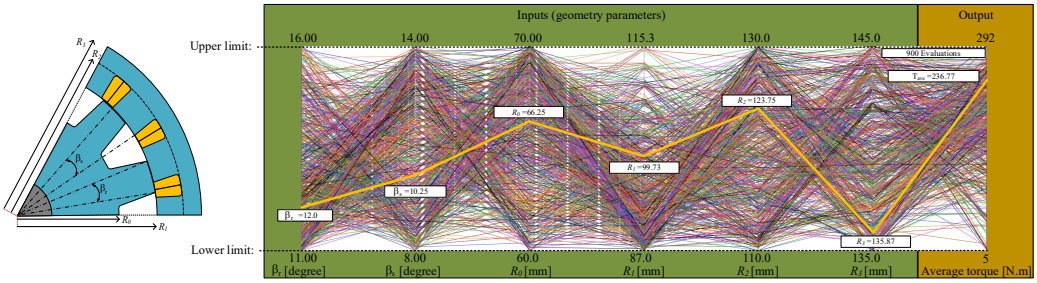

Fig. 5-7. An example of DOE evaluations of the static model.

The resulting DOE is then fitted with a fast surrogate model, which are used as the objective of static optimization. Due to the high nonlinearity of an SRM, the conventional linear fit models are not accurate enough. Two nonlinear models are selected as the surrogate model: (i) Radial Basis Function (RBF) and (ii) Neural Network (NN).

5.2.2.1: Radial Basis Function Surrogate Model

The radial basis function (RBF) is a function in which the output is dependent on the distance of the inputs and some fixed points. Traditionally, there are several options such as Gaussian and Multiquadric for the function of the RBF.

After some investigation and analysis, the Gaussian function is selected for the surrogate model. The RBF surrogate model is expressed as

$$f(x) = \sum_{i=1}^{n} \lambda_i e^{-\frac{(\|x-d_i\|)^2}{2\sigma_j^2}} \tag{5.6}$$

where d_i is the fixed point i, x is the vector of input variables, n is the number of fixed centre points, σ_j is the standard deviation for the Gaussian basis function i, λ_i is the gain for the Gaussian basis function i, and $f(x)$ is the surrogate model output.

As illustrated in Fig. 5-8, the RBF can also be related to the feedforward neural network. The training process of the RBF is moderate and the running time, when used as a surrogate model, is very fast.

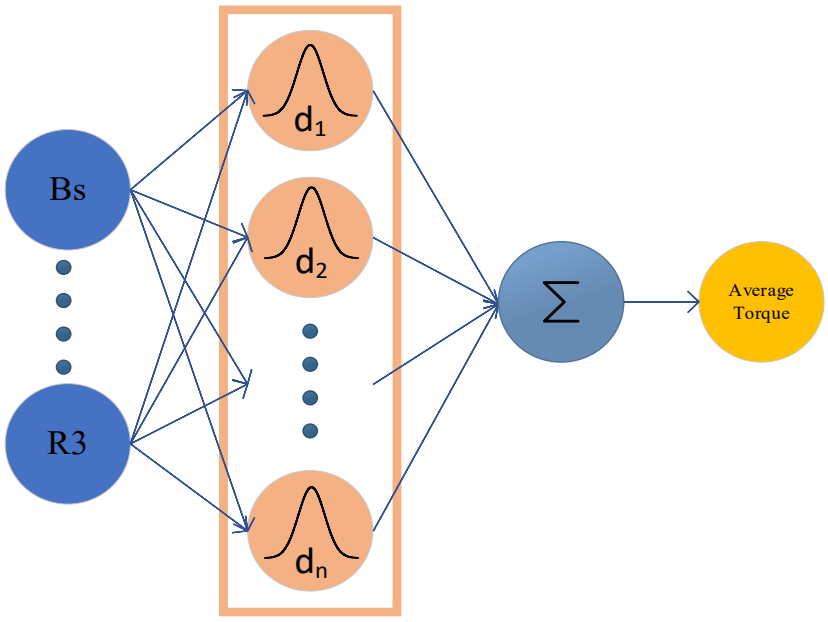

Fig. 5-8. Graphical illustration for radial basis function used as surrogate model.

5.2.2.2: Neural Network Surrogate Model

Considering the nonlinearity of the motor, a Neural Network (NN) is a good fit as a surrogate model. An NN with five hidden layers and fifty nodes is trained in the Python environment. The resulted NN has high accuracy and fast running time.

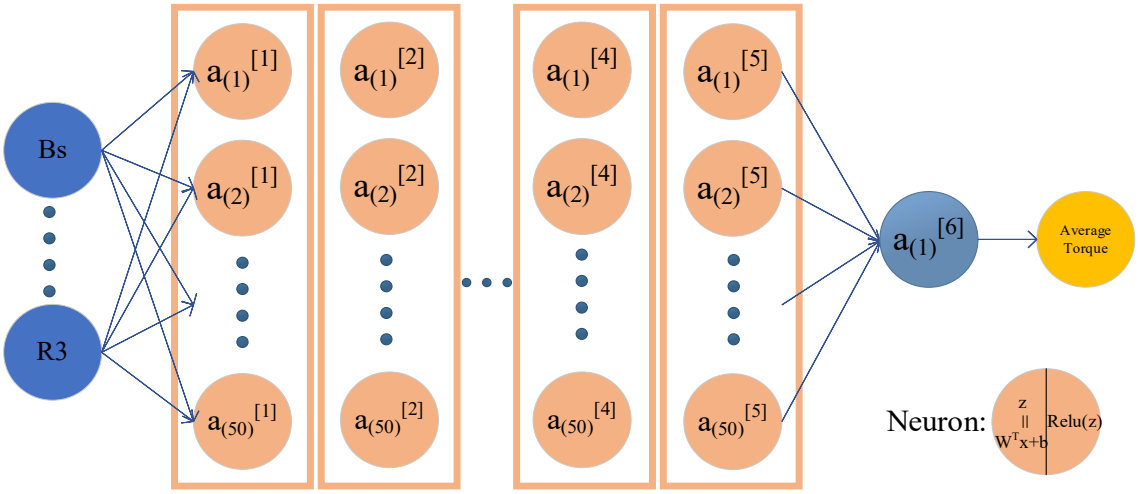

Fig. 5-9. Graphical illustration for NN used as a surrogate model.

5.2.3: Global Optimization and Verification

A combination of two different surrogate models and three global optimization algorithms is used to increase the chance of capturing all high-torque-density geometry combination. Fig. 5-10 shows the combinations of surrogate models and global optimization algorithms. The RBF is used as a surrogate model of genetic algorithm (GA) and global response surface method (GRSM) in the Altair HyperStudy environment. The NN is used as a surrogate model of particle swarm optimization (PSO) with fix and variable inertia in the Python environment.

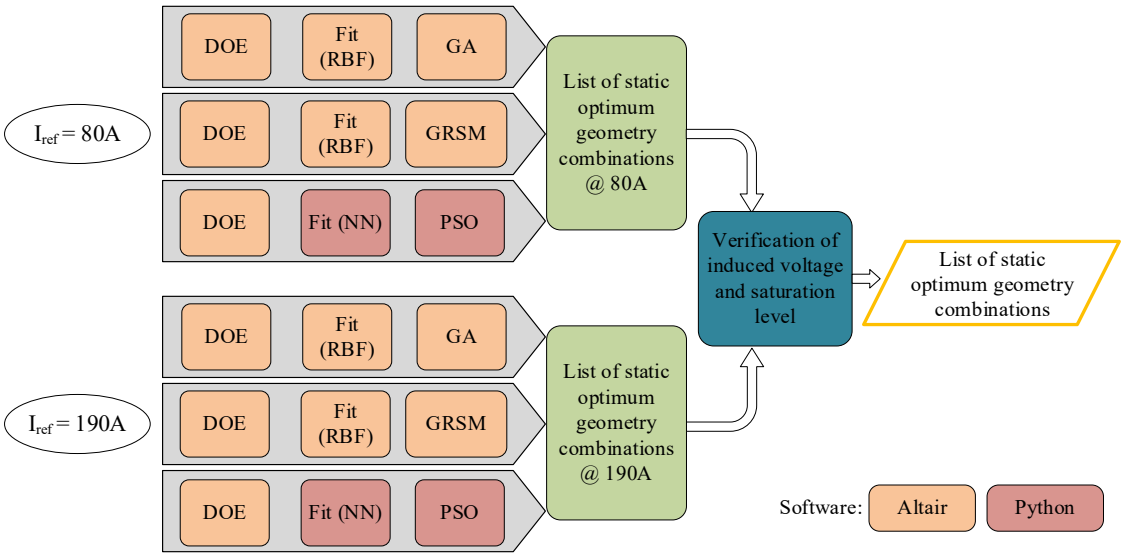

Fig. 5-10. Block diagram of the static design: Fit models and global optimizations used for two different currents rating.

The GA optimization of the RBF surrogate model was the most inclusive method and found the highest number of static torque geometry combinations. RBF surrogate model optimized with GRSM was the fastest; however, using a response surface over a surrogate model increases error, and the result is not as comprehensive as other methods. In the PSO, variable inertia was used to improve the convergence speed. Using PSO for the NN model has fast and inclusive results. After validating geometries for both current ratings, the list of the geometry combinations with high static average torque is prepared.

The use of different methods in parallel improves the comprehensiveness of the static design. On the other hand, the high number of results makes it more time-consuming to apply dynamic design for each of them. Therefore, the static design

results are clustered to reduce the number of initial geometries of the dynamic design process. Moreover, to double-check the accuracy of the surrogate models, the high-resolution FEA models are used to verify the list of outputs.

5.3: Dynamic Analysis and Design

The static optimization finds the geometry combinations with the highest static average torque. Those geometry combinations are then used as initial combinations in the dynamic design. The dynamic design aims to improve torque ripple and radial forces while maintaining high average torque. The motor's dynamic performance depends on the current conduction angles. The proposed method is based on the assumption that if the changes in the geometry are small, the optimized conduction angle does need to be changed. The block diagram of the dynamic design method is shown in Fig. 5-11. The design process is developed by a loop involving geometry and controls optimization. For each of the initial geometry combinations, a full static characterization is performed, and then, using a genetic algorithm, the conduction angles are optimized. The FEA model with dynamic excitation is used as a model in a GRSM optimization, and the resulting geometry is checked for the convergence criteria. If the design converged to a local minimum, the process is finished for this initial combination. Otherwise, the geometry goes through the loop again until either the design parameters converge or the number of iterations exceeds ten loops. In case, after the iterations, the geometry combination gets close to another initial geometry combination, the loop is aborted to eliminate redundant simulations.

In the next sub-section, each step of the dynamic optimization loop is explained in detail:

(i) 5.3.1: Optimization of Motor Control Parameters with Genetic Algorithm

(ii) 5.3.2: Finite Element Analysis Model with Dynamic Excitation

(iii) 5.3.3: Dynamic Optimization for Performance and Radial force Reduction with Limited Boundary

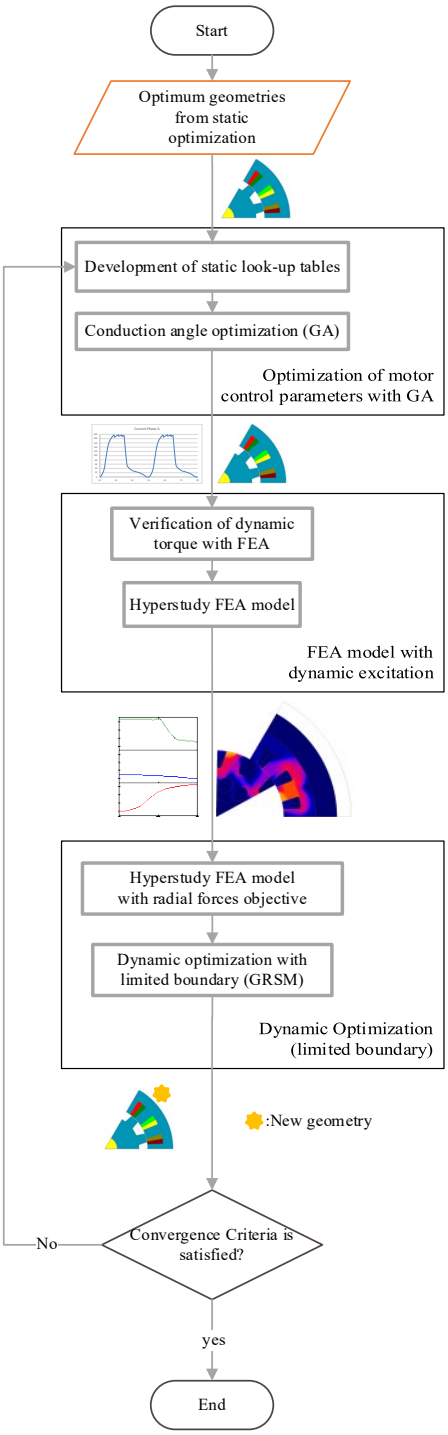

Fig. 5-11. Block diagram of the dynamic design loop.

5.3.1: Optimization of Motor Control Parameters with Genetic Algorithm

The control parameters have to be updated for each of the initial geometry parameters or after each iteration. The control optimization part of the dynamic optimization shown in Fig. 5-11 is highlighted with more details in Fig. 5-12. Each time the optimum control parameters need to be updated, static look-up tables should be created. In that process, the static characteristics of the motor under different constant current excitation are simulated with high resolution to obtain the required look-up tables. A sample of the simulated static characteristics for one of the geometry combinations is illustrated in Fig. 5-13.

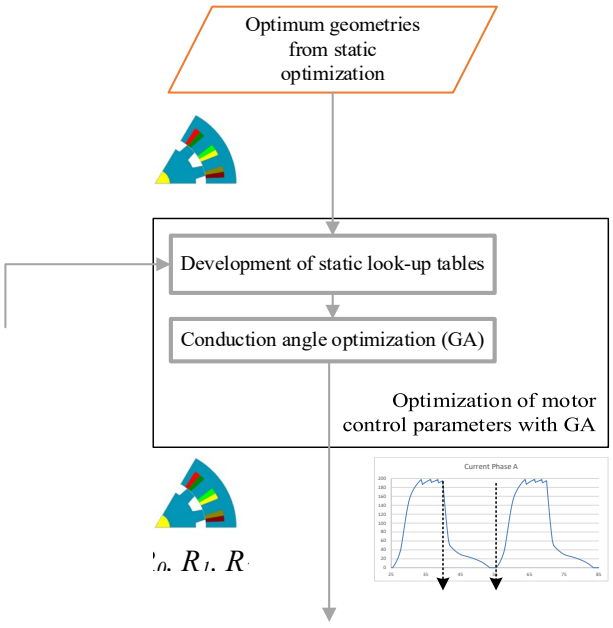

Fig. 5-12. Optimization of motor control parameters with GA.

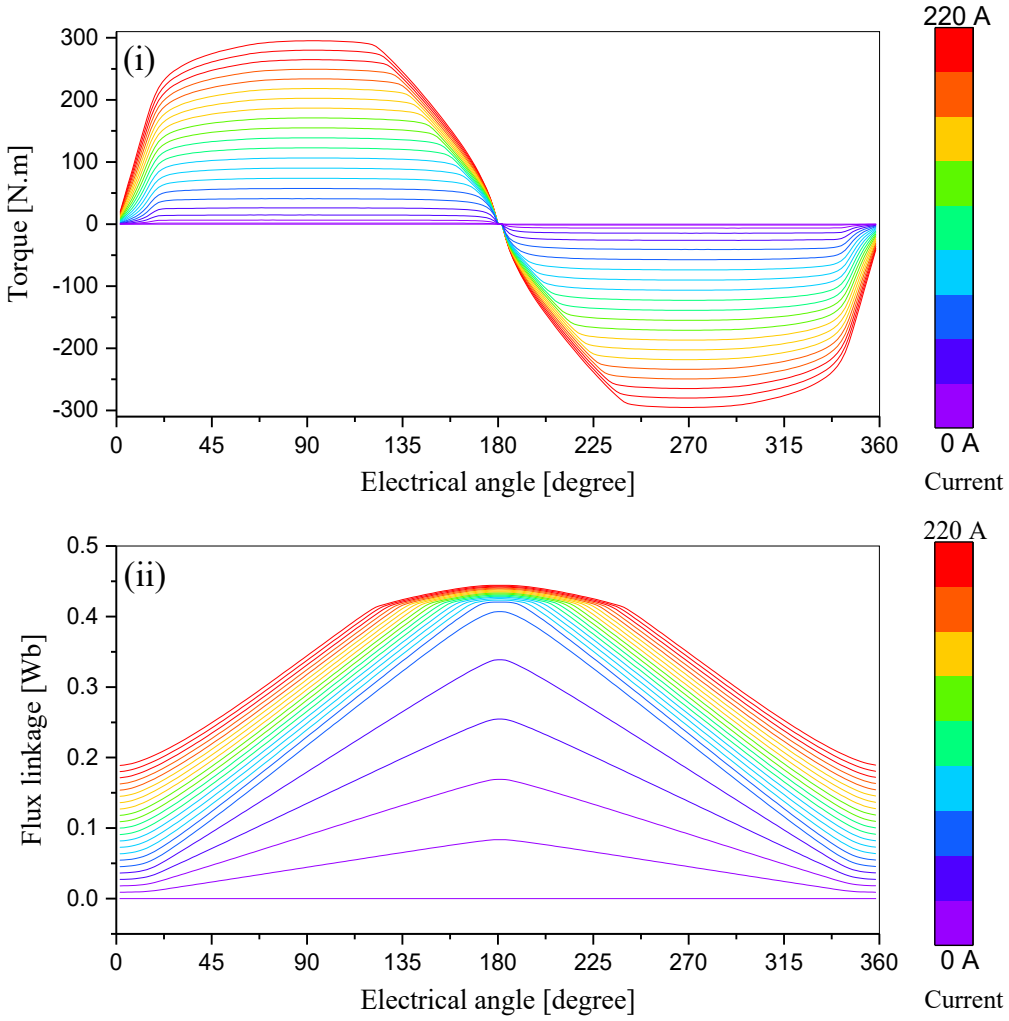

Fig. 5-13. Static motor characteristics used as look-up tables (i) torque, (ii) flux linkage.

The static characteristics are used as the look-up tables for a fast dynamic motor model in the Python environment. The model uses the equivalent circuit and the operational equations to determine the motor's dynamic performance for a given set of control parameters. Fig. 5-14 illustrates an example of the Python-based dynamic model that calculates the dynamic performance of the motor based on the control parameters and static lookup tables.

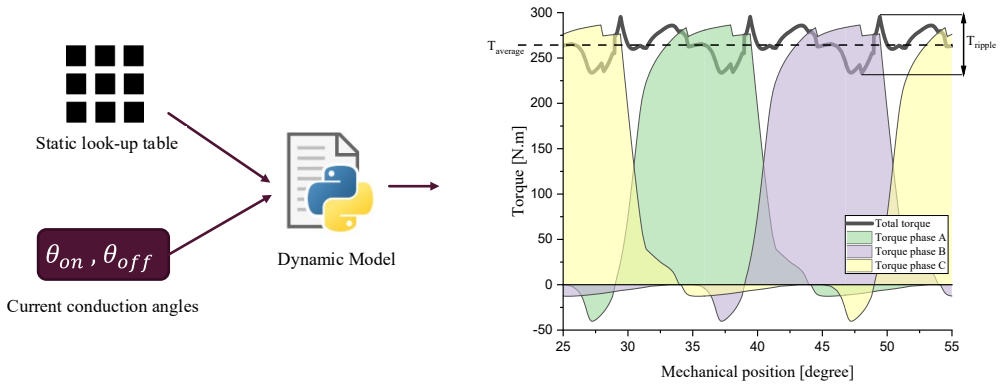

Fig. 5-14. Implementation and results of the dynamic model in Python environment.

The python based dynamic model is fast, and the control parameters can be optimized using different algorithms. A GA algorithm is used as the optimization method to find the best control parameters based on the defined objective for the average torque and torque ripple. A nonlinear constraint for the current of the motor is applied based on the maximum Root Mean Square (RMS) of the current:

$$I_{RMS} = \sqrt{\frac{1}{\theta_2 - \theta_1}\int_{\theta_1}^{\theta_2} I^2(\theta)d\theta} \leq I_{\text{limit}} . \tag{5.7}$$

where the I_{RMS} is the RMS value of the current, $I(\theta)$ is the current of the motor at electrical angle θ, and I_{limit} is the limit of current depending on the motor specification. The linear constraints are set for the current conduction angles as:

$$\begin{bmatrix} 1 & -1 \\ -1 & 1 \end{bmatrix} \begin{bmatrix} \theta_{on} \\ \theta_{off} \end{bmatrix} < \begin{bmatrix} -\frac{360}{m} \\ \frac{360k}{m} \end{bmatrix} \tag{5.8}$$

where m is the number of phases, k is the constant limiting the conduction period defined by the user, θ_{on} is the turn-on angle, and θ_{off} is the turn-off angle of the

asymmetric bridge converter used as the driver of the motor. Fig. 5-15 shows a sample of GA finding the fittest control parameters in the boundary of linear and nonlinear constraints.

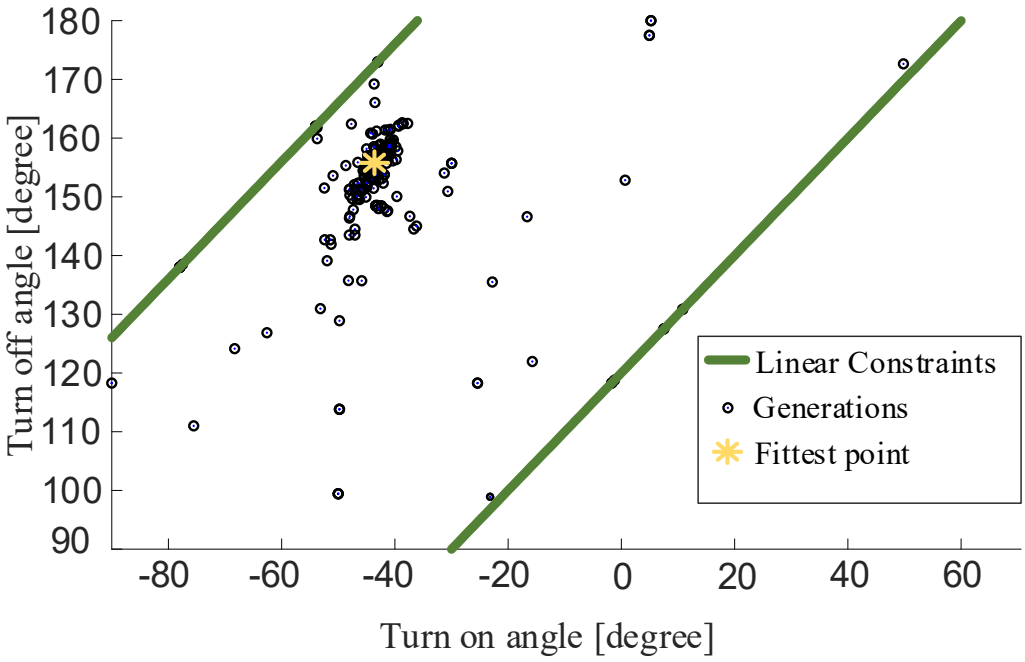

Fig. 5-15. GA used for the optimization of control parameters.

5.3.2: Finite Element Analysis Model with Dynamic Excitation

The Python-based dynamic model does not consider mutual coupling, but by using an FEA model with dynamic excitation, the effect of mutual coupling is checked to ensure it is minimal. As shown in Fig. 5-16, the dynamic excitations are applied to the FEA model, and the torque production is verified. Then the HyperStudy-compatible FEA model with dynamic current excitation is prepared.

To reduce the simulation time, the simulation span is limited to one-third of the electrical cycle because the motor has a periodicity of three based on the number of phases.

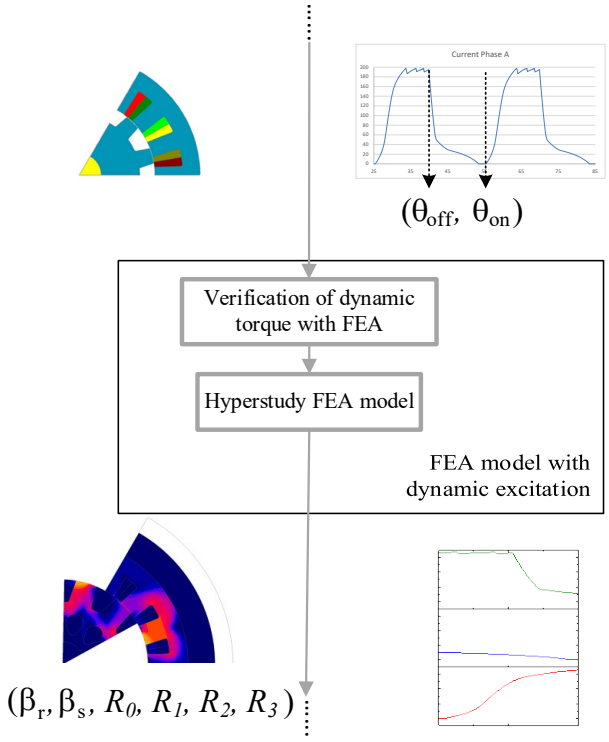

Fig. 5-16. FEA model with dynamic excitation.

5.3.3: Dynamic Optimization for Performance and Radial force Reduction with Limited Boundary

The dynamic design has radial forces as an objective, as well. As illustrated in Fig. 5-17, the FEA model can automatically generate the radial forces over the circumferential position of the motor and save the data in an excel file. Then a post-processing python script is developed to reconstruct the radial forces based on the

periodicities that are used in the FEA model and calculate the two-dimensional Fourie Transform (2D-FFT) of the waveform. The 2D-FFT decomposes the radial force waveform to the temporal and circumferential orders. A sample of radial force decomposition for an 18/12 SRM is graphically represented in Fig. 5-18 for dominant harmonics.

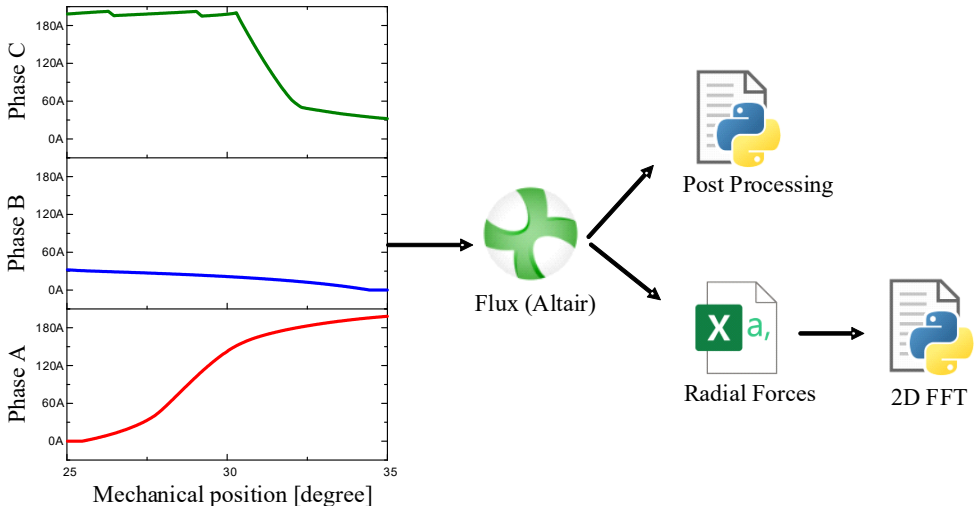

Fig. 5-17. HyperStudy compatible FEA model with dynamic excitations and post-processing scripts.

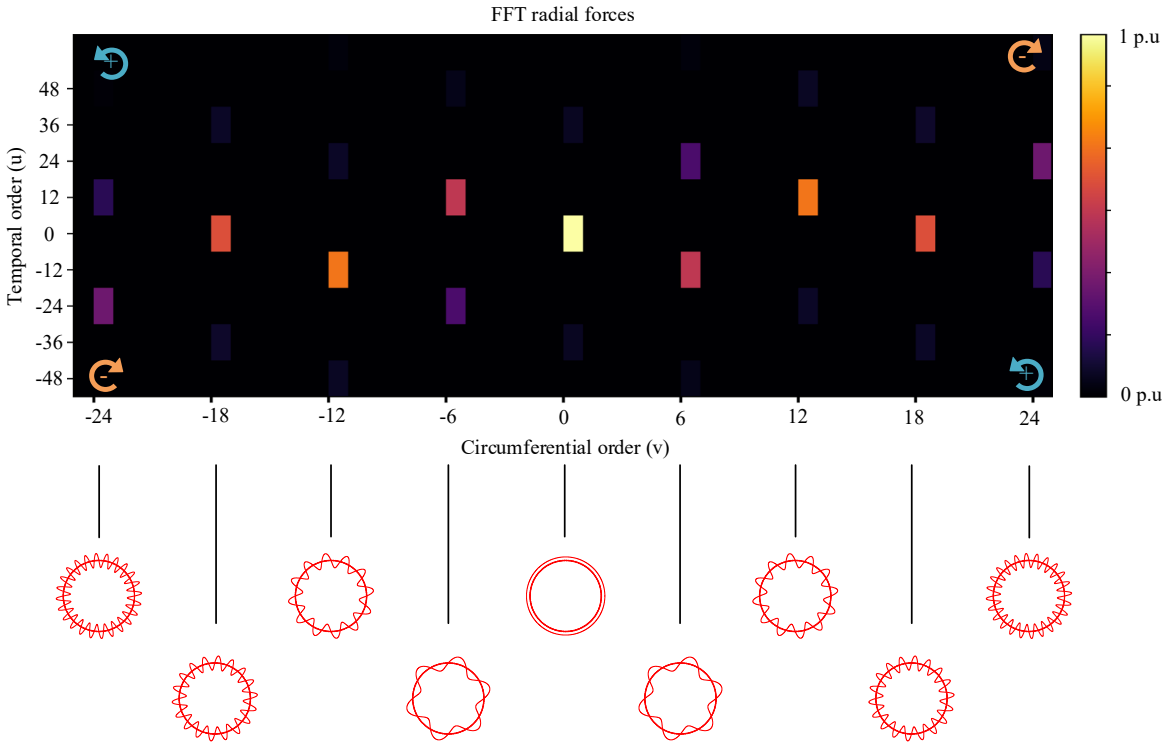

Fig. 5-18. Dominant radial forces harmonics for an 18/12 SRM.

The objective function for the radial force harmonic is defined as

$$Radial\ force\ objective = \sqrt{\sum_{u,v=-Lim}^{+Lim} G_{u,v}\, Fr_{u,v}^2} \qquad (5.10)$$

where the $Fr_{u,v}$ is the magnitude of the radial force harmonics and $G_{u,v}$ is the gain for the radial force harmonic with temporal order u and circumferential order v. The gain is designed to favour the reduction of lower-order harmonics more than higher-order harmonics due to different natural frequencies and damping ratios of different stator mode shapes.

With the HyperStudy-compatible FEA model and integrated post-processing python scripts, the motor geometry parameters are further improved within a limited boundary to ensure that the same optimum control settings can still be used. Because of the low boundary, the deterministic gradient-based optimization algorithms work well and converge fast to the better geometry combination in that boundary. The objectives are set to increase the dynamic average torque, reduce the radial force objective and maintain the low torque ripple. Fig. 5-19 shows the dynamic optimization in detail with convergence criteria and conditions. After the dynamic optimization with limited boundary, the convergence is checked for the following:

(i) The resultant geometry and control parameters are close to a previous iteration; hence the design process has converged.

(ii) The number of iterations exceeds ten without improving the performance; hence, the process is terminated.

(iii) The new geometry is close to another initial geometry; hence, the process is terminated to eliminate redundant simulation.

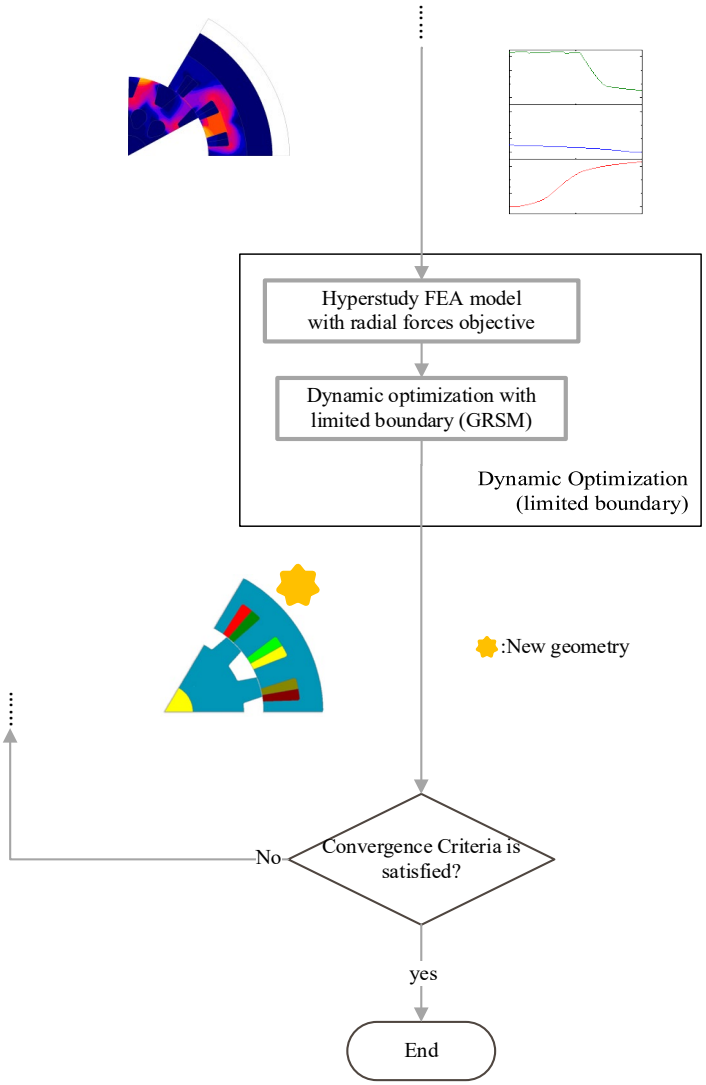

Fig. 5-19. Dynamic optimization (limited boundary) and convergence criteria.

5.4: Conclusions

In this chapter, an optimization framework for the design of a high-density switched reluctance motor is presented. With the separation of the design process into two stages, the framework seeks to overcome the interdependency between geometry design and conduction angle optimization. To determine the inclusive geometry combinations with the highest average static torque, the first layer combines the design of experiments, two nonlinear surrogate models (radial basis function and neural network) and three global optimization algorithms (e.g. genetic algorithm, particle swarm optimization, and global response surface method). For this stage, a lower current is also used to ensure the saturation level will not cause false low-induced voltages. These combinations of geometries are clustered and evaluated using finite element analysis to validate the accuracy of the surrogate model. Every geometry combination must undergo the second level of design: dynamic design. Dynamic optimization involves a loop involving control and geometry optimization along with objectification of radial force harmonics, torque ripple, and average torque. In each iteration of the loop, the variation of geometry parameters is limited so that the same control parameters are maintained. After the dynamic design is performed for all of the high static average torque geometry combinations, the best final geometry is selected as the final design.

Chapter 6

6. Design of a Switch Reluctance Motor for Light-sport Aircraft Application:

6.1: Introduction

A thorough study of the current and future market for electrified light-sport aircraft (LSA) and electrical motors was conducted in Chapter 2, and the desired motor specifications were defined. In Chapter 5, a multi-objective design framework for high power density switched reluctance motor was presented. In this chapter, the design of the LSA SRM is presented. First, the selection of core material is discussed. Then, the design of the motor geometry is presented using the proposed framework for the desired objectives. The design of the coil parameters based on practical constraints have been discussed. The use of rotor cutouts to reduce the rotor mass is proposed in order to improve the motor torque density. The static performance and torque-speed characteristics of the final electromagnetic

design is demonstrated. Steady-state thermal analysis is performed to calculate the motor's thermal performance at the base speed.

6.2: Selection of the Core Material

The performance of an SRM is highly dependent on the magnetic properties of the core material. A carefully selected magnetic core material should be used for both the stator and rotor core of the motor to enhance torque density. The material should exhibit low core loss and high saturation levels of magnetic flux. Two materials have been selected as candidates for the motor design due to their unique characteristics:

- HIPERCO® 50 and HIPERCO® 50A [58]

  Iron-cobalt vanadium alloys, such as HIERCO® 50 and 50A, have the highest magnetic saturation rating of all soft magnetic alloys (2.4 Tesla). In addition, the low core loss compared to electrical steels contributes to the higher efficiency for SRMs.

- JFE_10JNEX900 (Super Core ^{TM}) [59]

  Magnetic properties of silicon steel are well known to improve as the silicon content increases up to 6.5%. JNEX Core (Super Core ^{TM}) silicon steel sheets have improved silicon content compared to conventional silicon steel sheets. Using a chemical vapour deposition (CVD) process in manufacturing, the silicon content is increased up to 6.5%, compared to a maximum of 3.5% in conventional silicon steel. This results in a high silicon steel sheet with a high

saturation magnetic flux density up to 1.94 Tesla. In addition, the core loss is low, which helps improve the motor's efficiency.

As compared in Fig. 6-1, the magnetization characteristics of the materials are different, especially in the magnetic saturation level. The HIPERCO® 50/50A has a higher magnetic saturation level. The static performance of the same geometry with two different materials is illustrated in Fig. 6-2. With low current density and, hence, low magnetic field intensity, the static torque performances are close. However, as the current increases, the silicon-based material is unable to maintain performance compared to HIPERCO® 50/50A. Therefore, The HIPERCO® 50A is selected as the core material for the motor design in this project due to better performance and higher magnetic saturation.

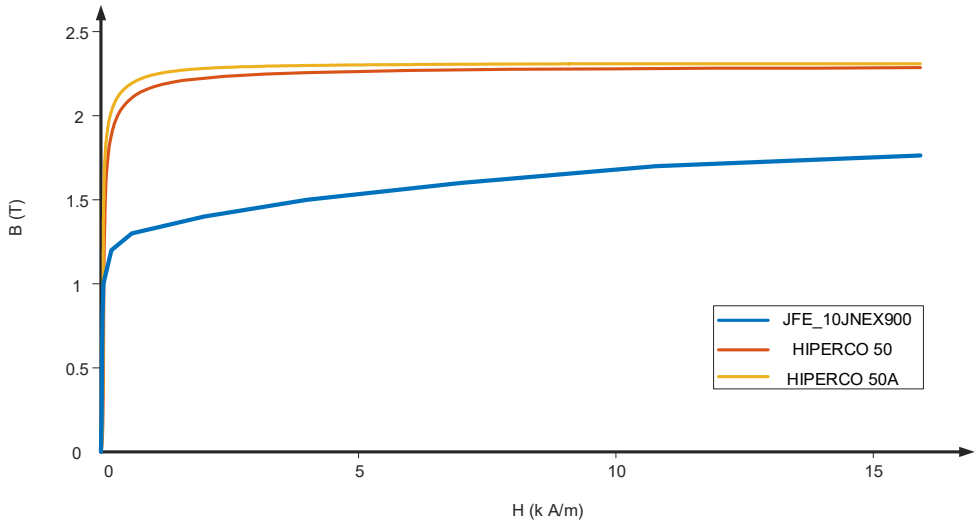

Fig. 6-1. Comparison of the magnetic properties of HIPERCO® 50/50A and JNEX Core.

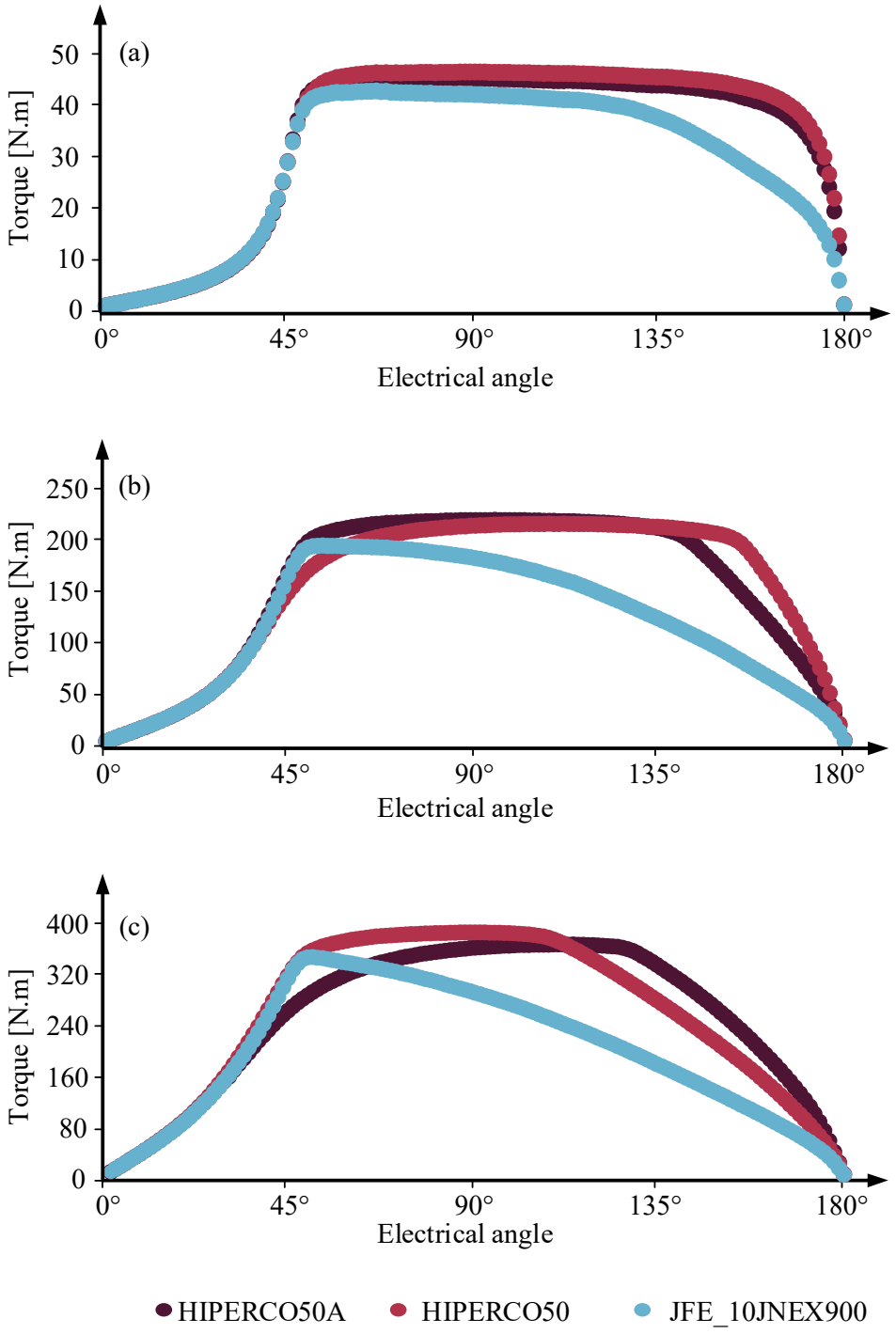

Fig. 6-2. Comparison of static torque production of HIPERCO® 50, HIPERCO® 50A, and JFE_10JNEX900; (a) J=5A/mm^2 , (b) J=15A/mm^2, and (c) J=25A/mm^2

6.3: Electromagnetic Design with the Proposed Framework

There are two stages in the proposed electromagnetic design framework: static design and dynamic design. The author suggests adding another stage before the framework is applied to familiarize oneself with the correlation of the SRM design parameters. This stage may be easily completed if the designer has SRM design experience before.

6.3.1: Initial Design

The motor application requirements and constraints define many of the motor's geometry parameters. One of the first steps of every motor design is to try some random design cases, observe the results, and understand the correlations between the parameters. The results from this initial design do not need to be perfect because the motor's geometry is going to be optimized in the following stages. But it is essential for the designer to understand the motor's different parameters and the geometry restrictions. Despite the fact that SRMs are highly non-linear, the fundamental electromagnetic relationships are able to explain the correlations similar to other motor types. For example, we may observe that when the axial length of the motor is increased, the induced voltage and the torque also increase. This observation may be explained by the changes in the slot area. The following factors can be considered when investigating the initial design stage:

- The induced voltage of the motor at base speed
- Current density limit (based on cooling system)

- Wire fill factor limit
- Mechanical constraints of the motor

It is noteworthy that some parameters should be fixed and not change over the proposed framework. The number of stator and rotor poles can be a variety of different combinations for three-phase SRMs. After several simulations of different possible combinations, the 18/12 combination is selected based on the motor's size and the application's speed and direct-drive requirements. The air gap is fixed to 0.4 mm based on the motor's speed, power rating, and mechanical constraints.

6.3.2: Static Design and Results

The static design aims to find the different geometry combinations with the highest static average torque production. A total of three different optimization algorithms with two different surrogate models were used to find the geometries for two current ratings: the nominal current and a lower current. Approximately one-third of the nominal current is used for the lower current design in order to prevent over-saturation at low current condition and ensure that the maximum induced voltage in the lower current cases is still below the DC link voltage, as explained in Fig. 5-6. The static design objective and constraints for each current level is as follows:

Minimize:

$$f_{(R0,R1,R2,R3,\beta r,\beta s)} = -mean(T_{static})$$

Subject to:

$$R_0 < R_1 < R_2 < R_3$$

$$8° < \beta s < 14°$$

$$11° < \beta r < 16°$$

$$20° < \beta s + \beta r < 30°$$

$$\max(V_{ind}) < V_{dc}.$$

The geometry parameters are defined in Chapter 5 in Fig. 5-5 in order to be able to control the phase current, mostly in the constant torque region of the motor, the maximum induced voltage should be less than the DC-link voltage, V_{dc} up to the base speed. The geometry parameters should be limited to the mechanical constraints, and the self-start capability limits the minimum value of the pole arc angles. As a result of using a constant current density region for the coils, coil constraints are not necessary for static optimization.

The static design for the given constraints and objectives find a list of more than 260 geometry combinations that have high static average torque. Many of these combinations are close to each other; the data is clustered based on the search radius of the next dynamic design stage. As previously mentioned, the highest correlation to the average torque is with rotor radius, $R1$, stator pole arc angle, βs, and rotor pole arc angle, βr. For illustration purposes, the list of torque-geometry combinations is plotted with those three parameters in Fig. 6-3:

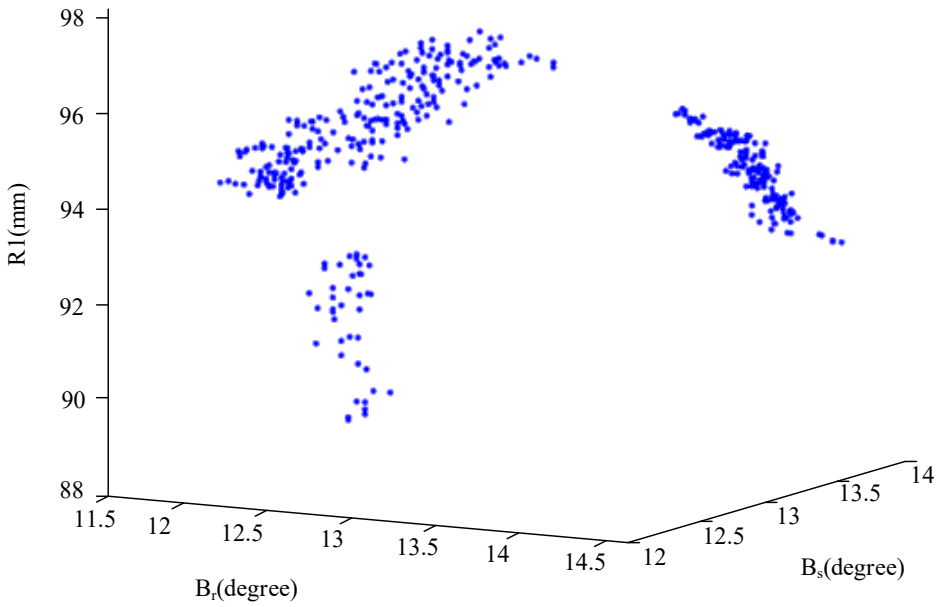

Fig. 6-3. Illustration of static design results with the three main parameters.

The resulting clustered data is verified with the FEA model to ensure that the surrogate model used was accurate. As shown in Fig. 6-4, the error of the surrogate model (RBF) was less than 0.9%. Each of these geometry combinations are applied to the next stage of design, dynamic design.

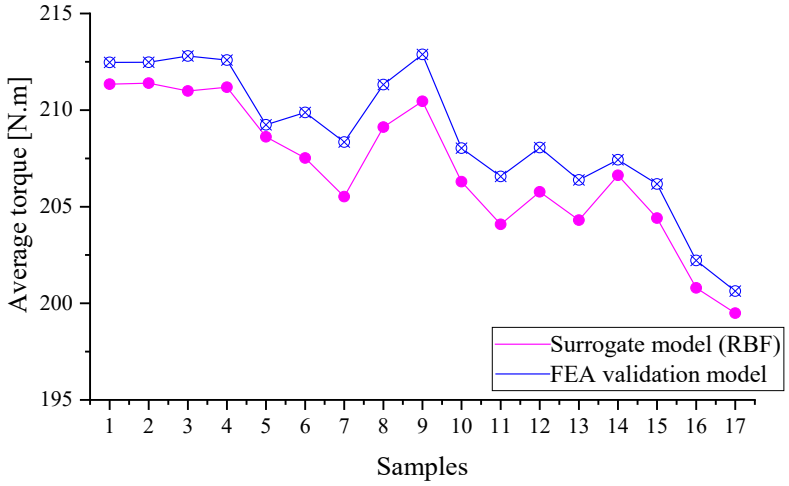

Fig. 6-4. Validation of average torque for surrogate model with FEA model.

6.3.3: Dynamic Design Process and Results

The dynamic design process integrates the control and geometry design in a loop to objectify the average torque, torque ripple, and radial force. Even though the pilot cabin is isolated from the propeller and the motor's noise is much lower than the propeller's noise, radial forces and torque ripple should be reduced. Radial forces and torque ripples can result in premature wear and fatigue of mechanical installation parts, as well as coupling between the motor and propeller.

For each of the geometry combinations resulting from the static design, the dynamic design process is performed. In the end, the best final design is selected as the final design. Table 6- 1 shows the changes in the motor geometry and performance improvements from the initial iteration to the last iteration for the selected final design. After five iterations of the dynamic optimization, the average torque was increased by 3.4%, whereas the torque ripple remained the same, and

the radial forces improved. Fig. 6-5 shows the reduction in the radial force harmonics following five iterations for the selected geometry. Significant reductions are observed in the magnitudes of circumferential orders zero, six, and twelve. Although the magnitude of the circumferential order eighteenth has been slightly increased, on the whole, the optimization process has improved torque performance while reducing radial forces. The circumferential order eighteen of the radial force harmonic would potentially excite vibration mode zero through the sampling effect. The increase in the magnitude of the circumferential mode 18 is smaller than the decrease in the magnitude of the circumferential mode zero of the radial force density harmonics. Therefore, overall, a reduction in the excitation of the vibration mode zero can be expected.

Table 6- 1: The improvements of the motor performance after five iterations in the dynamic design process for the selected design.

Parameter	**Initial iteration**	**Final iteration**
Stator pole arc angle, βs	13.25	13.153
Rotor pole arc angle, βr	12.65	12.74
Turn on angle	-54.659842	-47.9
Turn off angle	122.93833	125
Average torque	258.56	267.8
Torque ripple (%)	18.04	19.48
Radial force objective	245.45528	241.52

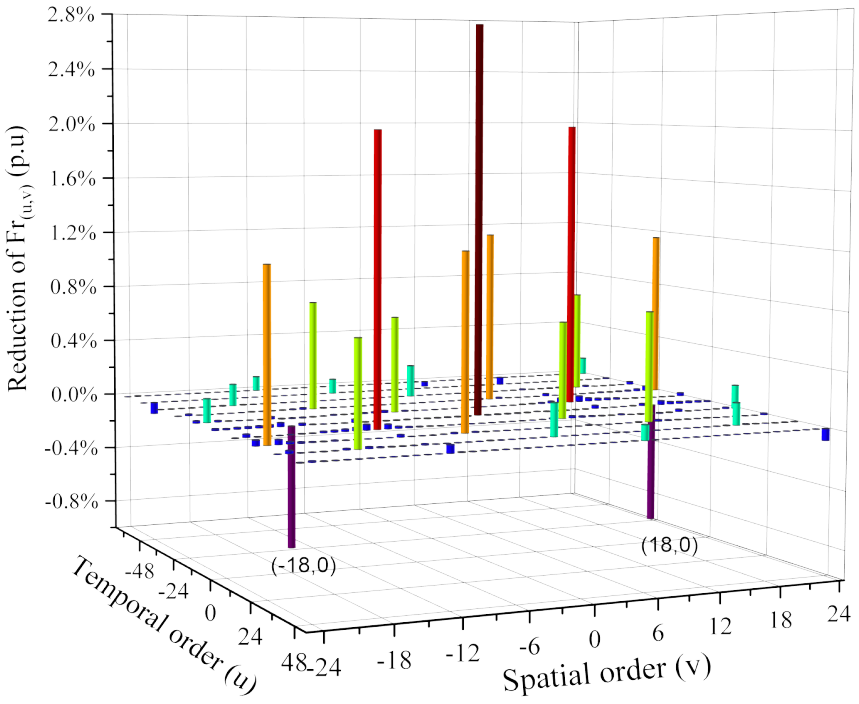

Fig. 6-5. An evaluation of the change in radial force after five iterations of dynamic optimization.

6.4: Coil design

In the proposed framework, the coil design is based on a constant current density region in the static design stage and on a simplified stranded coil conductor region in the dynamic design stage. The coil design aspect requires special attention due to its high impact on the performance of the motor, both in terms of torque production, thermal performance, and overall dimensions of the motor.

6.4.1: Coil Design Script

A MATLAB script is used to automate the coil design process, as shown in Fig. 6-6, to identify the possible coil parameters based on fill factor, current density

limit, and magnetomotive force. The magnetomotive force is calculated based on the simplified stranded coil conductor region of final model of dynamic design. The current density limit is based on the cooling method, and the slot area is based on the selected geometry. With the help of the script, the feasible coil configurations are listed in Table 6-2. As highlighted in the table, the six parallel winding options are preferred. This is because parallel winding configurations enables coils with higher number of turns and fewer number of strands. Fewer number of strands allows an easier implementation of the coils and reduces the resistance mismatch between the strands of a coil, if the strands are wound on top of each other, which might be essential especially when a winding machine is used. Fewer strands also enable better wire layout in the coil implementation, which helps achieving a more consistent resistance in each coil of the motor and, hence, more balanced phase resistances. Besides, parallel winding configuration helps mitigating unbalanced magnetic pull in case of eccentricity [60].

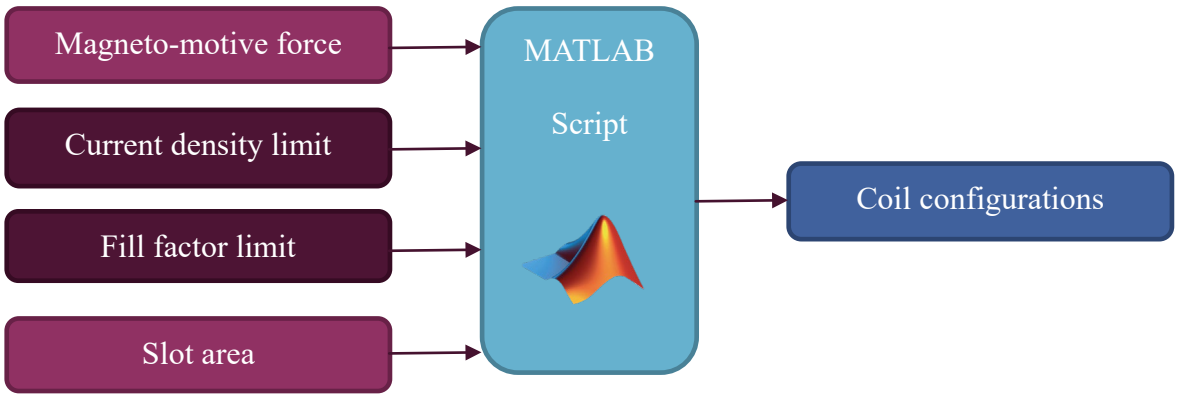

Fig. 6-6. Coil design script.

Table 6-2: Coil possibilities for the design

Winding pattern	Number of turns per coil	Magnet wire American Wire Gauge (AWG)	Number of strands	Number of conductors per coil	Copper fill factor	Current density (@ 120A) [A/mm2]	Coil resistance (@ 25 °C) [Ω]	Phase resistance (@ 25 °C) [Ω]
6 coils in series	14	9	1	14	0.53	18.10	0.008885	0.053307
		12	2	28	0.53	18.14	0.008906	0.053435
		14	3	42	0.50	19.21	0.009440	0.056643
		15	4	56	0.53	18.16	0.008928	0.053570
		16	5	70	0.53	18.35	0.009009	0.054054
2-parallel, 3-series	28	12	1	28	0.53	18.14	0.035623	0.053435
		15	2	56	0.53	18.16	0.035713	0.053570
		17	3	84	0.50	19.23	0.037867	0.056800
3-parallel, 2-series	42	14	1	42	0.50	19.21	0.084964	0.056643
		17	2	84	0.50	19.23	0.085200	0.056800
6 coils in parallel	83	17	1	83	0.50	19.23	0.336742	0.056124
		20	2	166	0.50	19.27	0.337474	0.056246

In coil prototyping, in addition to having a limited fill factor and current density, it is preferred to avoid many strands and magnetic wires that are too thin or too thick. Based on the power rating and size of the motor, a six parallel coil pattern is a better fit for the prototyping of this motor. The preferred coil options are summarized in Table 6- 3.

Table 6- 3: Comparison of different preferred coil option

Parameter	**Option 1**	**Option 2**
Pattern	6P	6P
American wire gauge (AWG)[1]	17	20
Number of turns	83	83
Number of strands	1	2
Copper fill factor	0.5	0.5
Wire fill factor	0.59	0.59
Current density (120A)	19.23 A/mm^2	19.27 A/mm^2
Phase resistance @25ºC	56.12 mΩ	56.25 mΩ
Phase resistance with end turn[2] @ 200ºC	111.2254 mΩ	111.4831 mΩ

[1] MW35-C triple insulation

[2] Includes phase leads and inter-coil connections

6.4.2: AC Losses Verification

The AC losses and the effect of the skin and proximity effects were not considered in the geometry design framework or coil design script. In order to simulate the skin effect and the AC losses, both preferred coil options are tested with individual windings in the FEA. A Python (Pyflux) command automates the conversion to solid conductors for each coil winding option. Fig. 6-7 shows the coils converted into individual wire designs for both options.

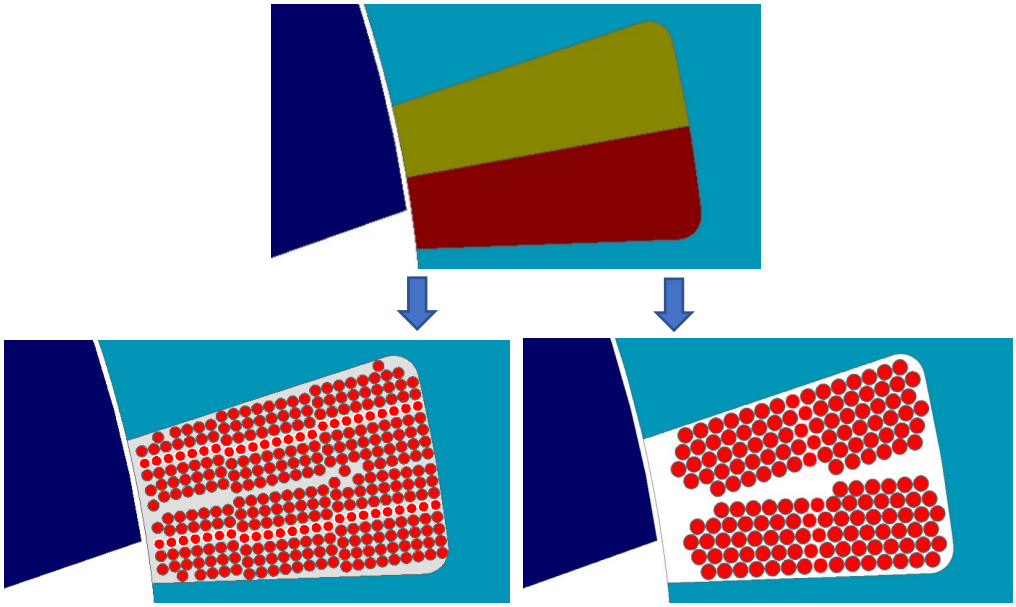

Fig. 6-7. Conversion of stranded coil region to coil with individual wires.

The AC losses of the windings are simulated using a transient FEA analysis that considers each conductor individually in the corresponding circuit. The AC copper loss is about 1 to 6 % higher than the power loss calculated from the RMS current and phase resistance. The AC copper loss is illustrated in Fig. 6-8 for both

coil winding options. The average AC copper loss is summarized in Table 6- 4. AC copper loss of option 2 with thinner wire and more strands is slightly lower. However, the difference in the losses is not significant, and the lower number of strands of option one makes it a better fit for coil implementation and manufacturing of the motor. Hence, option one is selected as the final winding coil design.

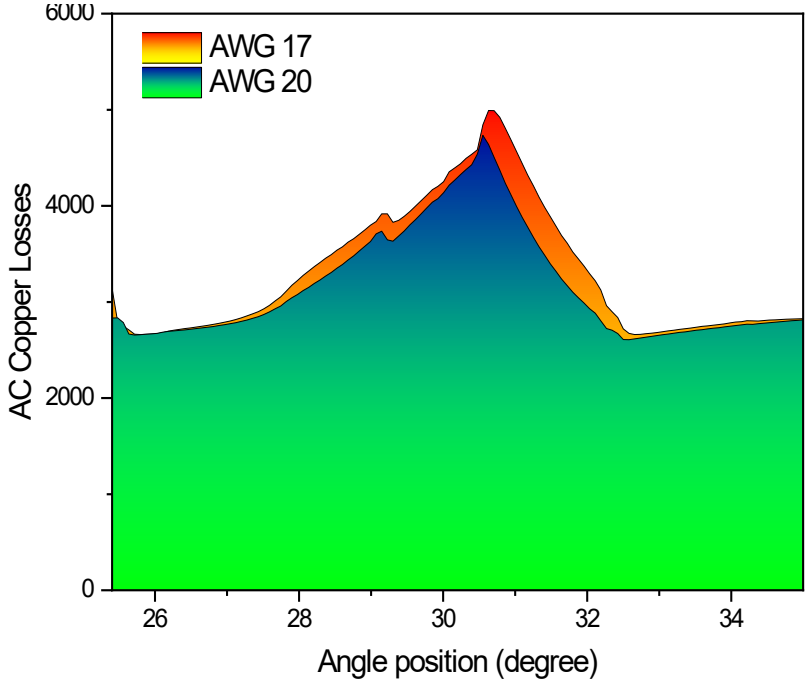

Fig. 6-8. Comparison of AC losses for two different winding options.

Table 6- 4: Comparison of average AC copper loss for two different winding options

	American wire gauge (AWG)	**Number of strands**	**Copper losses (AC) @ 150°C**
Option 1	17	1	3307.75W
Option 2	20	2	3162.58 W

6.4.3: Coil Retention Design

To ensure that the coils are secure inside the stator slots, a slot wedge design is considered. The stator of the LSA SRM is designed without any pole shoes to not to impact the flux path and cause a reduction in electromagnetic torque. Therefore, the stator teeth need to be designed with grooves to insert the slot wedge as shown in Fig. 6-9.

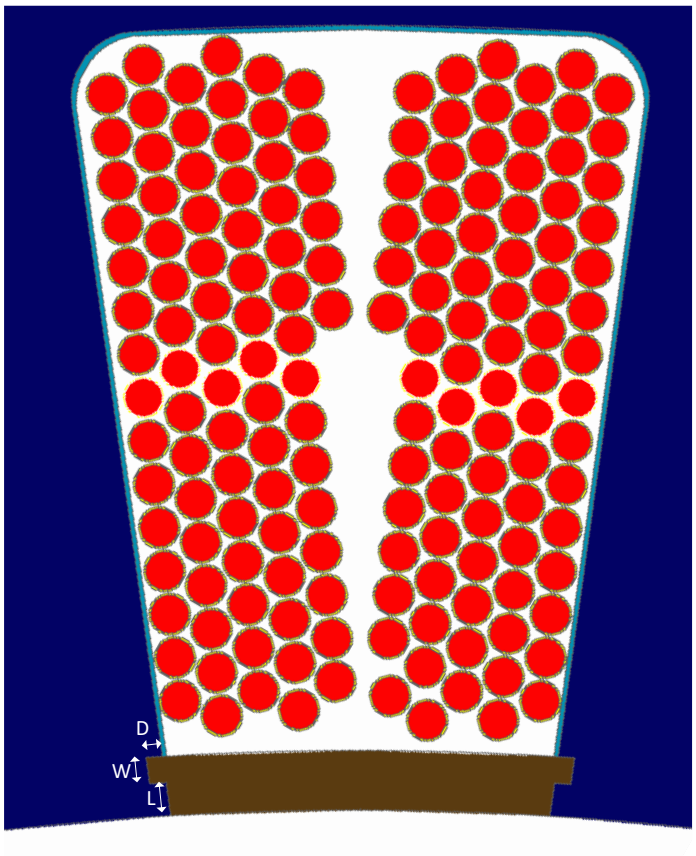

Fig. 6-9. Coil retention with grooves and slot wedge, and the geometry parameters of the slot wedge.

It is essential to design the size and the shape of the grooves so that they do not have a significant impact on the magnetic flux, slot area and, hence, the

electromechanical performance. A simple design of the experiment is performed by varying the parameters of the groove to find the effect of the location of the grooves and their size. Fig. 6-10 shows the effect of the groove on the torque production of the motor with groove width of 0.8mm. The boundary that the groove parameter can change without a significant effect on the torque production is shown in Fig. 6-10 with a dashed rectangle.

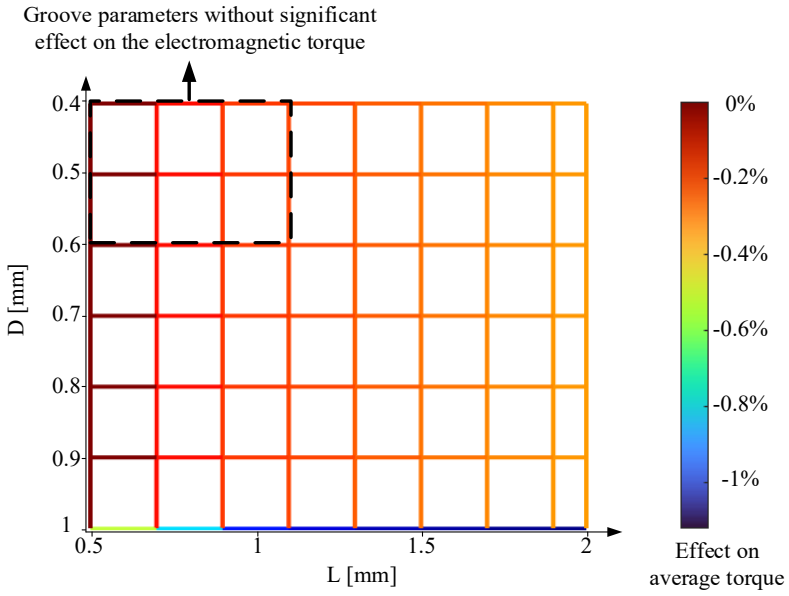

Fig. 6-10. Effect of groove dimensions on torque production with 0.8mm width groove.

The slot retention wedge is designed to be prototyped by 3D printing using glass-filled nylon or Durable nylon. Based on the size of the part and required accuracy, selective laser sintering (SLS) 3D printing is selected. These materials are mechanically and thermally strong and have been used in prototyping for similar purposes. Based on the analysis, the dimensions of the grooves are set to be 0.8 mm

wide, 0.5mm deep and 1 mm away from the edge of the stator teeth (W = 0.8 mm, D = 0.5 mm, and L = 1 mm in Fig.6-9). In addition to verification of the coil retention with FEA mechanical model, the 3D printed part is used to ensure the strength and correct tolerance of the coil retention as shown in Fig. 6.11.

Fig. 6-11. 3D printed stator with coil retention for validation of strength and tolerance.

6.5: Reducing the Rotor Mass

In the design of the LSA SRM, several design methods were used to enhance the torque density of the motor as much as possible. Based on the magnetic flux paths of the rotor, some rotor cut-outs can be used to reduce the rotor's weight; hence, increasing the motor's torque density. In addition, the reduction of mass in the rotor reduces the inertia of the motor; hence, the dynamic mechanical performance can be improved. The position and shape of the cut-outs can vary based on the rotor design and performance requirements.

6.5.1: Proposed Rotor Cut-outs and Their Effect on the Torque Production

The tapered elliptical cut-outs were selected as rotor cut-outs due to their high mass reduction and lower deterioration of mechanical strength [61]. The position of the cut-outs is selected based on the magnetic flux paths to ensure that they have minimal effect on the electromagnetic performance of the motor. After several design iterations for the size of the rotor cut-outs, the 4.97 mm and 9.29 mm are selected for the dimension of the tapered elliptical cut-outs, as illustrated in Fig. 6-12. The key consideration was monitoring the magnetic flux density and ensuring that over saturation does not happening even in the worst-case scenario. In order to investigate the worst-case scenario, a wide conduction period (-40° and 180°) is selected, and the magnetic flux density level is monitored in the rotor to be

homogenously distributed. The rotor cut-outs reduced the rotor mass by 18.4% equivalent of approximately 3 kg of mass reduction.

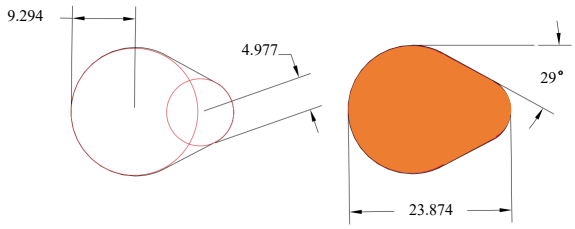

Fig. 6-12. Proposed rotor cut-outs (dimension in mm).

In addition to magnetic flux density monitoring, the effect of rotor cut-outs is investigated by checking the static characteristics before and after the rotor cut-outs. The motor static torque production for before and after cutouts is shown in Fig. 6-13. The good placements and shape of the rotor cutouts ensure there is no considerable torque reduction due to the rotor cutouts.

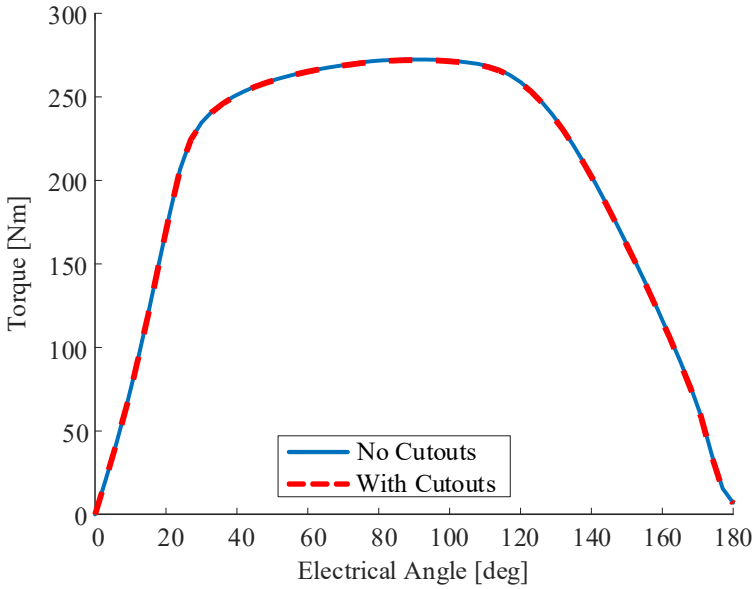

Fig. 6-13. Static torque before and after rotor cut-outs at 195 A.

6.5.2: Mechanical Stress Verification

The impact of the rotor cut-outs are structurally validated by using mechanical FEA. The total deformation and von-Mises stress analysis are performed to ensure no stress concentration exists around the added cut-outs. For the mechanical analysis, material properties are required. The mechanical properties of the core material are summarized in Table 6- 5.

Table 6- 5: Mechanical properties of HIPERCO® 50A [58]

Property	Value	Unit
Density	8120	Kg/m^3
Young's modulus	2.07E+11	Pa
Poisson's ratio	0.3	Pa
Bulk modulus	1.725E+11	Pa
Shear modulus	7.9615E+10	Pa
Tensile yield strength	2.12E+8	Pa
Tensile ultimate strength	4.98E+08	Pa

The mechanical analysis is performed in the Ansys software, and the deformation and the von-Miss stress analysis are conducted for 4500 rpm speed, which is higher than the operating speed by a considerable margin. The results of the simulations are presented in Fig. 6-14 and Fig. 6-15. There is no stress concentration around the rotor cut-outs, and the maximum stress is below the yield

strength. Therefore, the displacement is minimal as well. The maximum displacement is compared with the case without cut-outs, and the difference is 6 µm, which is 1.5% of the air gap length. The mechanical analysis concludes that the rotor mass reduction with cutouts does not compromise the motor's mechanical operation even at an extremely high-speed operation for this motor.

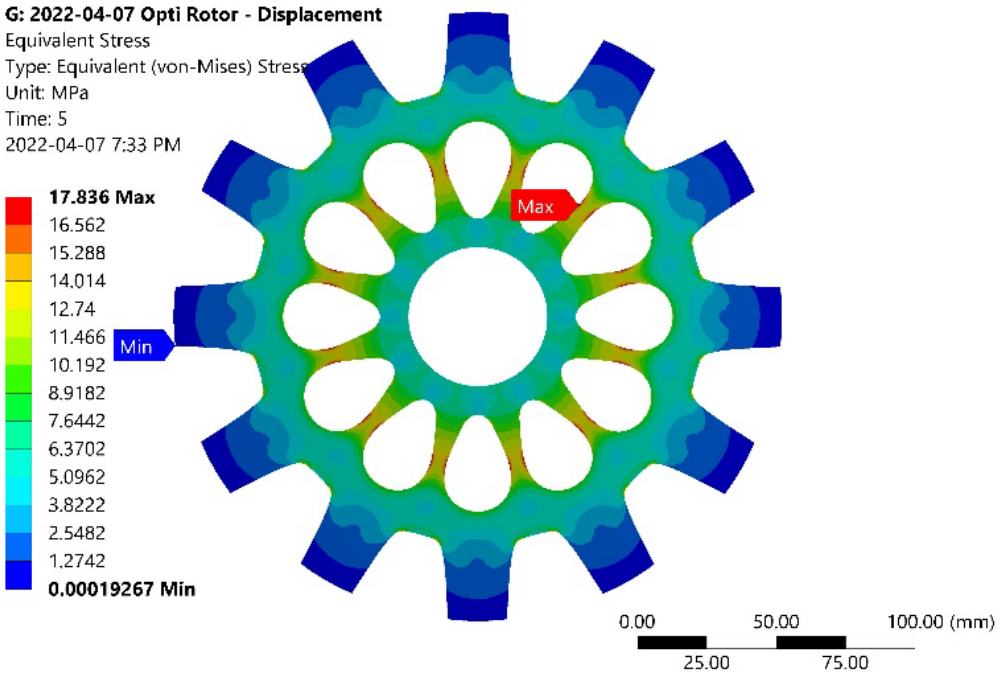

Fig. 6-14. Von-Mises stress of the rotor at 4500 RPM.

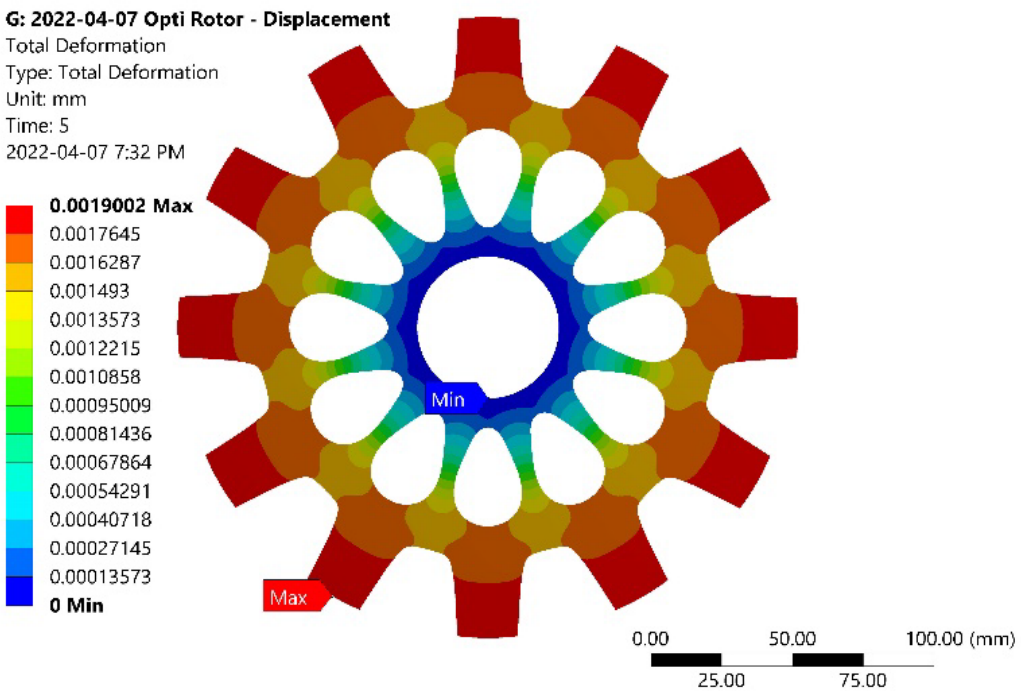

Fig. 6-15. Deformation of the rotor at 4500 RPM.

6.6: Final Electromagnetic Design and Results

The final motor design met the operational requirements of the specific application while adhering to the application constraints. The final design parameters are listed in Table 6- 6 and Table 6- 7.

Table 6- 6: The 18/12 SRM's final geometry configuration

Parameter	Value
Airgap length	0.4 mm
Stack length	100 mm
Shaft diameter	50 mm
Number of stator poles	18
Stator back iron thickness	20 mm
Stator pole height	23.6 mm
Stator pole arc angle	13.153^o
Stator taper angle	2^o
Stator bottom fillet radius	2 mm
Number of rotor poles	12
Rotor back iron thickness	45 mm
Rotor pole height	26 mm
Rotor pole arc angle	12.74^o
Rotor taper angle	4^o
Rotor bottom fillet radius	2 mm

Table 6- 7: The 18/12 SRM's final coil configuration

Parameter	**Value**
Coil configuration	Six parallel
Magnetic wire (Ansi type)	MW35-C
Wire insulation	Triple insulation
Wire gauge	17 AWG
Number of strands	1
Number of turns	83
Slot fill factor	59%
Phase resistance[3] @ 200°C	111.2254 mΩ/phase
Phase resistance[3] @ 25°C	66.3142 mΩ/phase

Geometry and coil configuration are designed to achieve high performance while constrained by application requirements and prototyping limitations. The static characterization of the final design is conducted through Altair Flux software by energizing the motor's single phase with constant current excitation for one electrical cycle. As shown in Fig. 6-16 to Fig. 6-18, the static voltage, torque, and flux linkage characterization were derived from this simulation.

[3]Includes estimated phase leads and inter-coil connections.

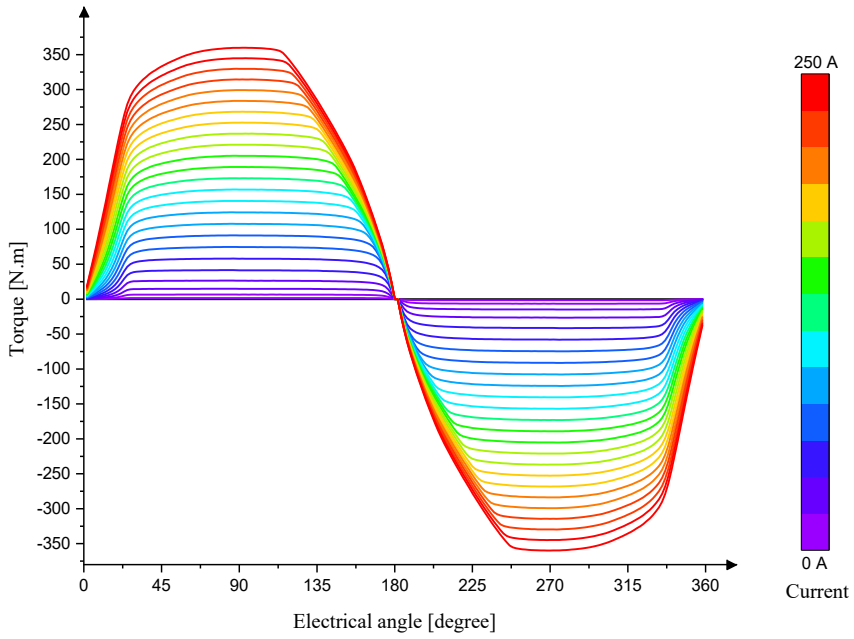

Fig. 6-16. Static electromagnetic torque for different current references.

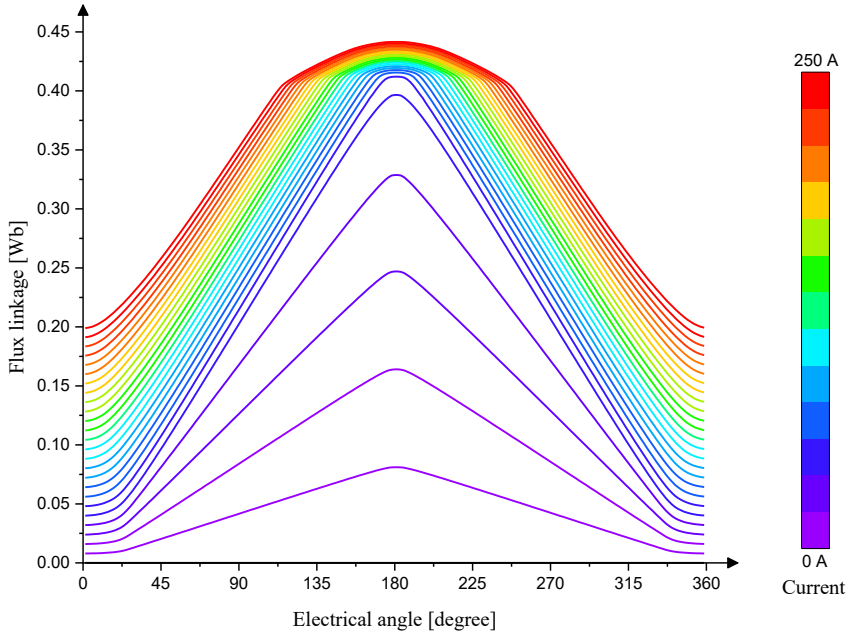

Fig. 6-17. Flux linkage versus current reference for different electrical angles.

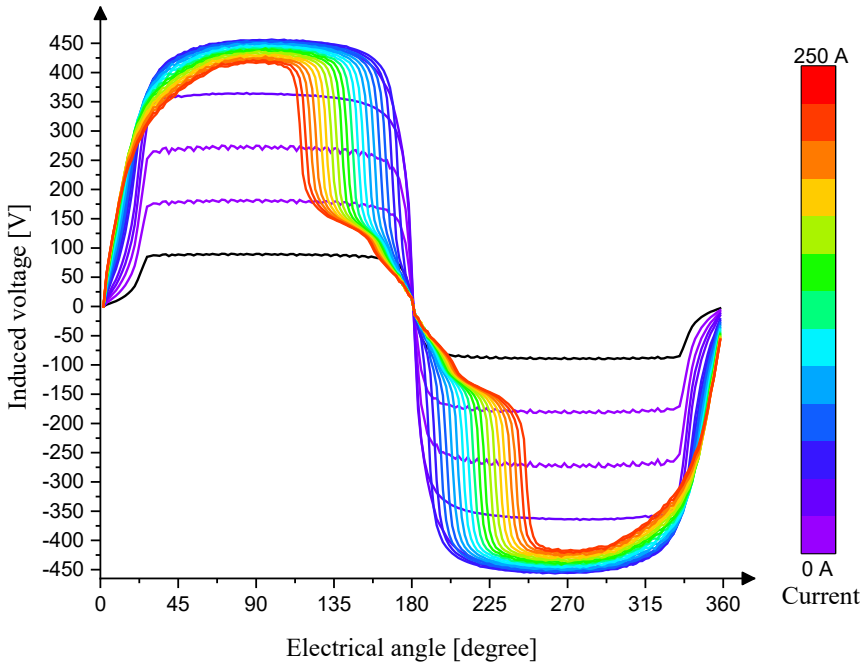

Fig. 6-18. Static voltage waveform at 2600 RPM for different current references.

The motor performance in different speed conditions is investigated by optimization of control parameters. A multi-objective genetic algorithm was used to find the turn-on and turn-off angles of the asymmetric bridge converter with a constant current reference of 200A. The objectives were increasing the average torque and reducing torque ripple. In Fig. 6-19, the torque-speed characteristics and the optimized turn-on and turn-off angles are illustrated. As predicted as the speed increases, the conduction period is shifted to a beyond unaligned position. Based on the application load characteristics, the motor's speed is mainly limited to the highlighted region (“Main operational region”).

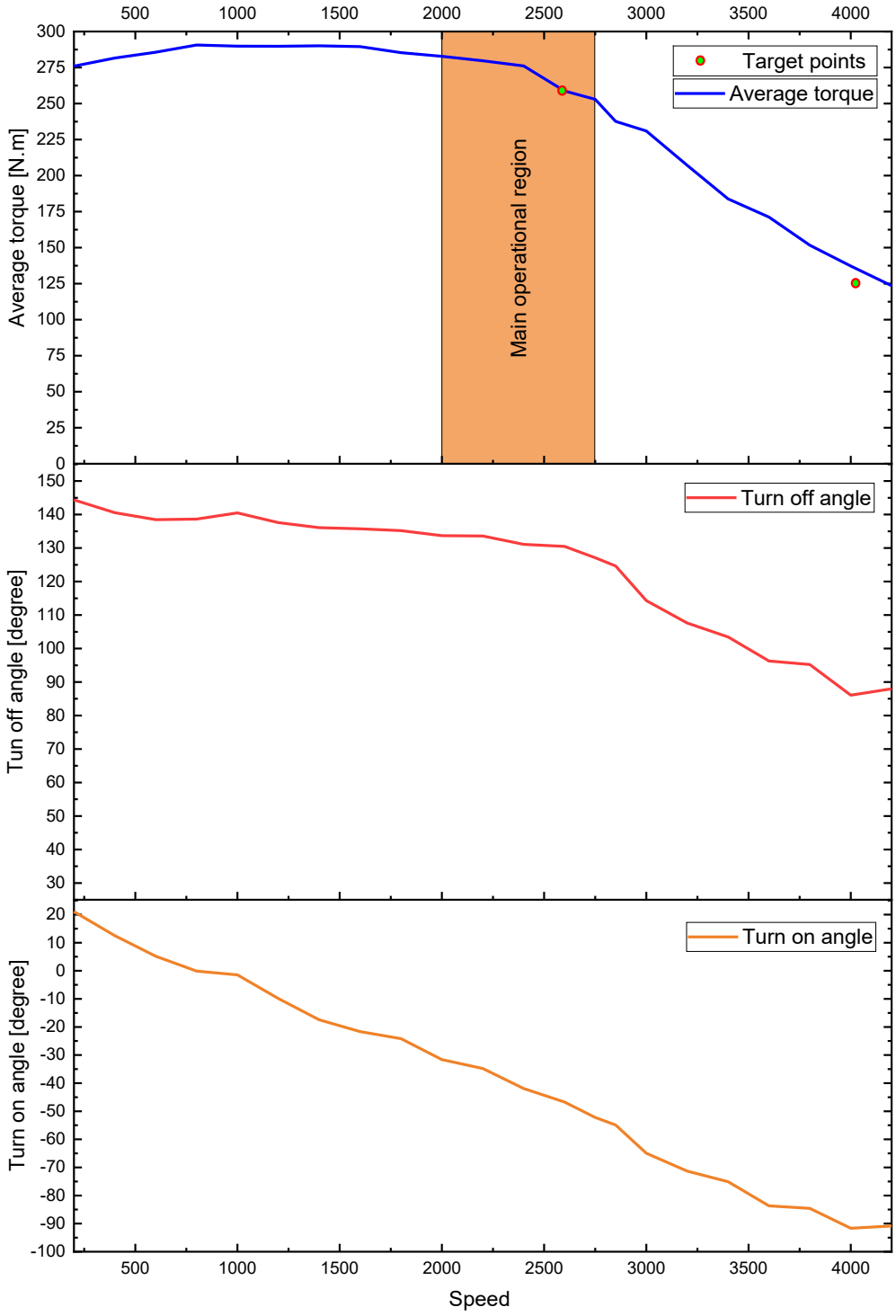

Fig. 6-19. Torque speed characteristics of designed motor with optimized turn-on and turn-off angle.

A three-dimensional electromagnetic FEA model is prepared to validate the two-dimensional electromagnetic FEA, as shown in Fig. 6-20. The main target point for the motor, which is in the operational region of the load, is 2600 RPM. The same optimized current waveforms and, hence, conduction angles at 2600RPM is used in the two-dimensional (Fig. 6-21) and three-dimensional (Fig. 6-22) electromagnetic FEA. Fig. 6-23 compared the torque waveforms from the two-dimensional and three-dimensional FEA. The average torque production is 2.5% smaller in the three dimensional FEA.

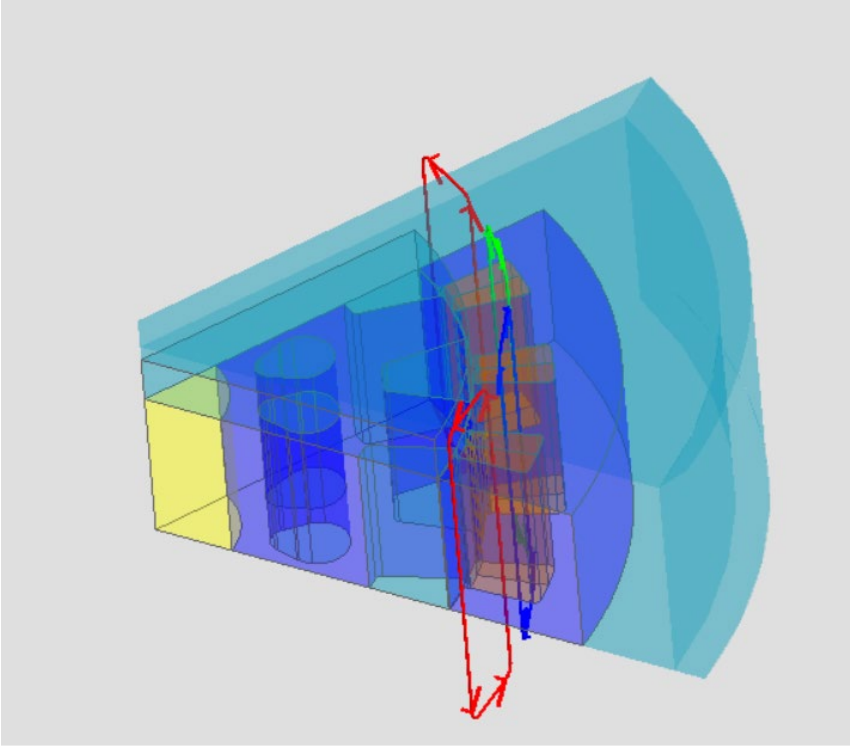

Fig. 6-20. Three-dimensional electromagnetic model for the designed motor.

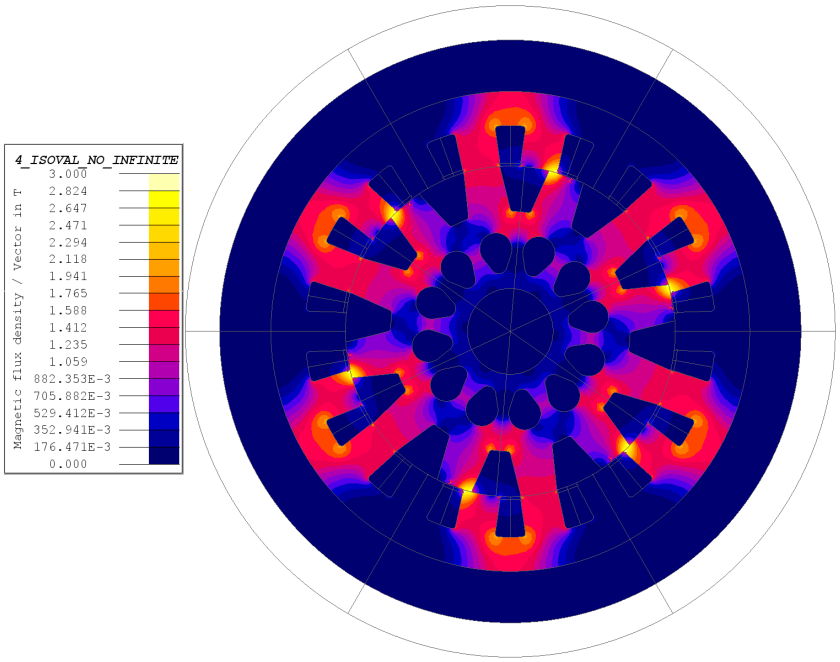

Fig. 6-21. Illustration of two-dimensional magnetic flux density @2600RPM with conduction angle -47.9° and 125°, and I_{ref} = 200A.

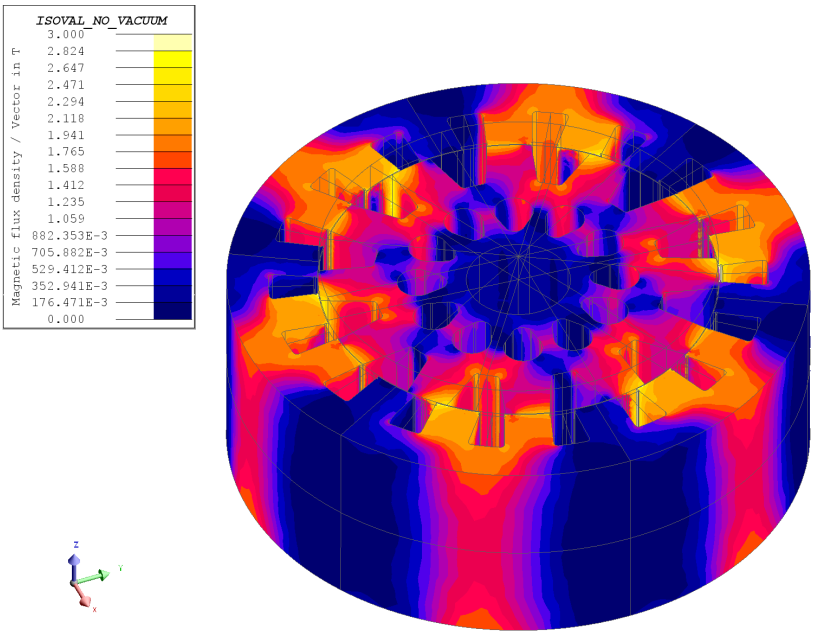

Fig. 6-22. Illustration of three-dimensional magnetic flux density @2600RPM with conduction angle -47.9° and 125°, and I_{ref} = 200A.

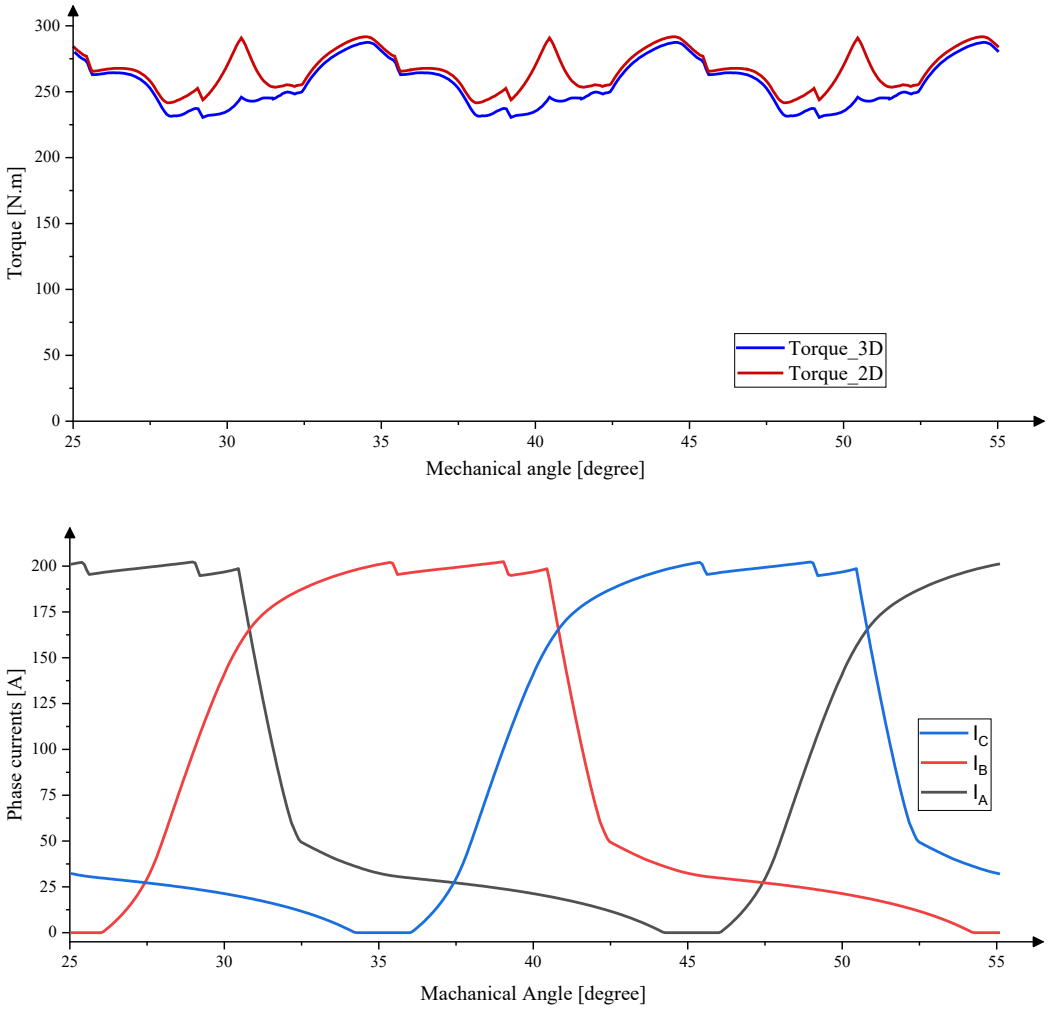

Fig. 6-23. Comparison of torque production with three-dimensional and two-dimensional FEA @2600RPM with conduction angle -47.9° and 125°, and I_{ref} = 200A.

6.7: Loss Calculation and Efficiency Analysis

The core losses are simulated based on the modified Bertotti core loss method, which is preferred by the Altair Flux software. The steady-state core loss equation is presented in (6.1), and the transient core loss equation is presented in (6.2). The function $g(\alpha)$ in (6.2) is defined as in (6.3),

$$P_{SS} = k_1 B_m^{\alpha_1} f + k_2 (B_m f)^{\alpha_2} + k_3 (B_m f)^{\alpha_3} \tag{6.1}$$

$$P_{trans} = k_1 \left(B_m^{\alpha_1} f\right) + k_2 g(\alpha_2) \left|\frac{dB}{dt}\right|^{\alpha_2} + k_3 g(\alpha_3) \left|\frac{dB}{dt}\right|^{\alpha_3} \tag{6.2}$$

$$g(\alpha) = \frac{1}{(2 * \pi)^{\alpha - 1}\, 4 \int_0^{\frac{\pi}{2}} cos^{\alpha}\theta \, d\theta} \tag{6.3}$$

where B_m is maximum magnetic flux density, f is frequency, k_1 and α_1 are coefficient and exponent for hysteresis loss term, k_2 and α_2 are coefficient and exponent for classical loss term, and k_3 and α_3 are coefficient and exponent for excess loss term. The coefficients and exponents are estimated based on the core loss data for the HIPERCO® 50A and presented in Table 6-8.

Table 6-8: Modified Bertotti's exponents and coefficients values for the HIPERCO® 50A

Exponents	Value	Coefficients	Value
α_1	1.61939	k_1	54.56280
α_2	2.113459	k_2	0.0350734
α_3	1.386721	k_3	6.527015

The losses and efficiency of the motor are simulated for the base speed (2600 RPM). This is the main operating condition of the LSA SRM and it has a high conduction period to provide high average torque. The resistive losses are simulated considering the AC losses with FEA, and the core losses are simulated with the modified Bertotti method. The losses and the efficiency for the base speed are summarized in Table 6-9. The estimated efficiency for the main operating condition of the motor is calculated as 94.8%.

Table 6-9: Calculated losses and efficiency for nominal current reference and conduction angles -47.9° to 125° @ 2600 RPM

Loss type	Value
Resistive loss in coils (AC losses)	3307.75 W
Average core losses in the rotor	287.6485 W
Average core losses in the stator	337.5244 W
Efficiency	94.8%

6.8: Thermal Analysis

A steady-state thermal analysis is performed to calculate the thermal performance of the motor. For this purpose, the heat sources are considered for the continuous operation at the base speed which has a relatively high current conduction time. Table 6-10 shows the materials properties considered in the thermal analysis. The steady-state thermal behaviour is analyzed by using force boundary conditions to represent the effect of cooling convection of the stator water

jacket and rotor air. A general rule of thumb for the convection heat transfer coefficient can be used for the boundary conditions of the simulation. In Table 6-11, the convection heat transfer coefficient, *h* is summarized according to the cooling method.

Table 6-10: Thermal conductivity characteristics for materials.

Application	**Material**	**Thermal cond. [W/m·K]**	**Max Temp. [^{o}C]**
Stator/Rotor laminations	HIPERCO® 50 [58]	29.83	704[4]
Conductors	Copper	385	1080
Magnetic wire	Polyamidimide (ML)	0.26	240
Impregnation solid (Option 1)	Composite (Aluminum Nitride in Elan Cast P300) [62]	1.2	180
Impregnation solid (Option 2)	Lord CoolTherm® EP-2000 [63]	1.9	204
Coil retention	DuraForm® PA plastic [64]	0.7	180
Liner	Nomex 818 [65]	More than 0.1	250
Cooling jacket	Aluminum	247	660
Air	Air	0.025	--
Moving air	Air	0.24	--

[4] Annealing temperature

Table 6-11: Convection heat transfer coefficient rule of thumb based on colling method

Application	**heat transfer coefficient, h [W/(m^2 K)]**
Natural convection (Air)	5-10
Forced convection (Air)	10-300
Forced convection (water)	500-10000

The simulation of the steady-state thermal analysis with a simple cooling jacket and rotor air convection is performed. The cooling jacket is implemented as illustrated in Fig. 6-24. The cooling performance is simulated using forced boundary conditions with convection coefficients. The water jacket with 50-50 water/glycol is assumed to have a convection coefficient of 6000, and the moving air convection is assumed to be 150. The steady-state thermal FEA results are illustrated in Fig. 6-25. The maximum steady-state temperature is 170.2°C and it is measured on the conductors. Notably, 200°C class magnet wires are widely available. Therefore, the steady-state temperature at the main operating point of the motor is lower than the thermal-class of the magnet wire.

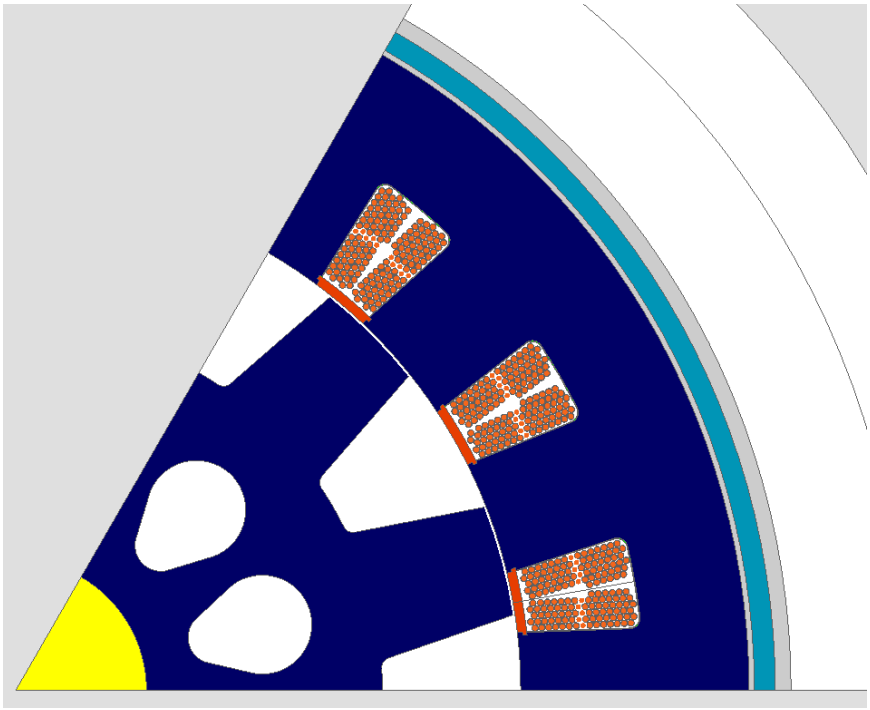

Fig. 6-24. Illustration of cooling jacket in a two-dimensional view.

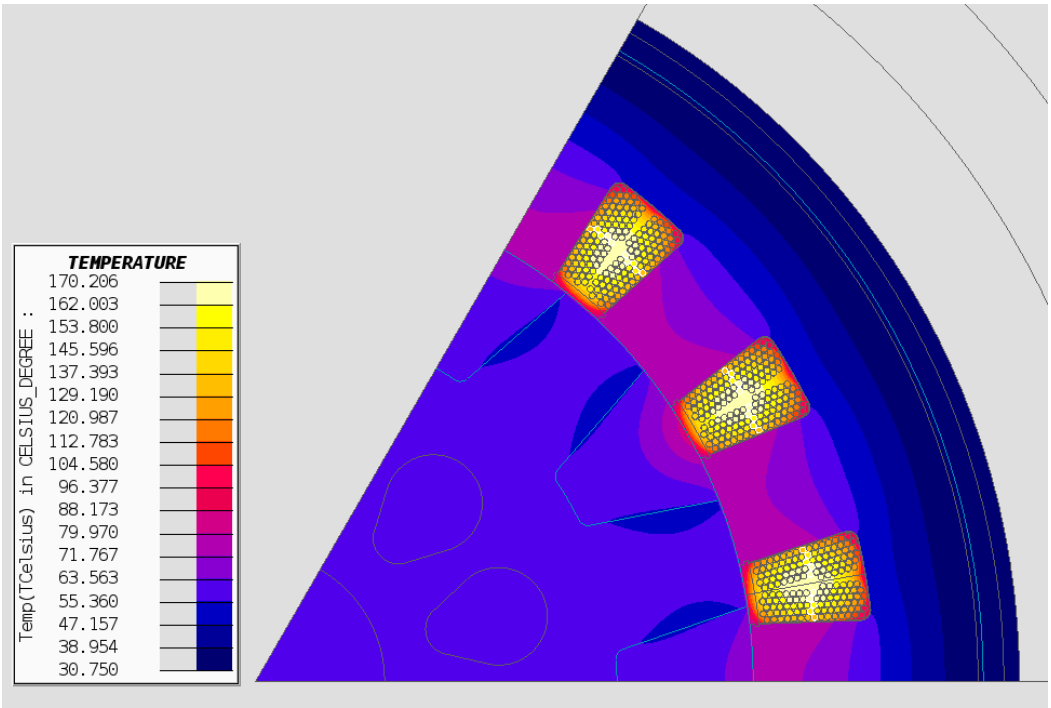

Fig. 6-25. FEM Steady-state thermal analysis result at the base speed.

In addition to steady state thermal simulation with forced boundary conditions, MotorCAD software is used to perform three-dimensional analytical transient thermal simulations. The three-dimensional model is shown in Fig. 6-26. A spiral water jacket with 50/50 water glycol and flow rate of 10 L/min is selected for transient thermal simulations. Although the analytical modelis less accurate than the FEA (Fig. 6-25), it considers the cooling system parameters in more detail.

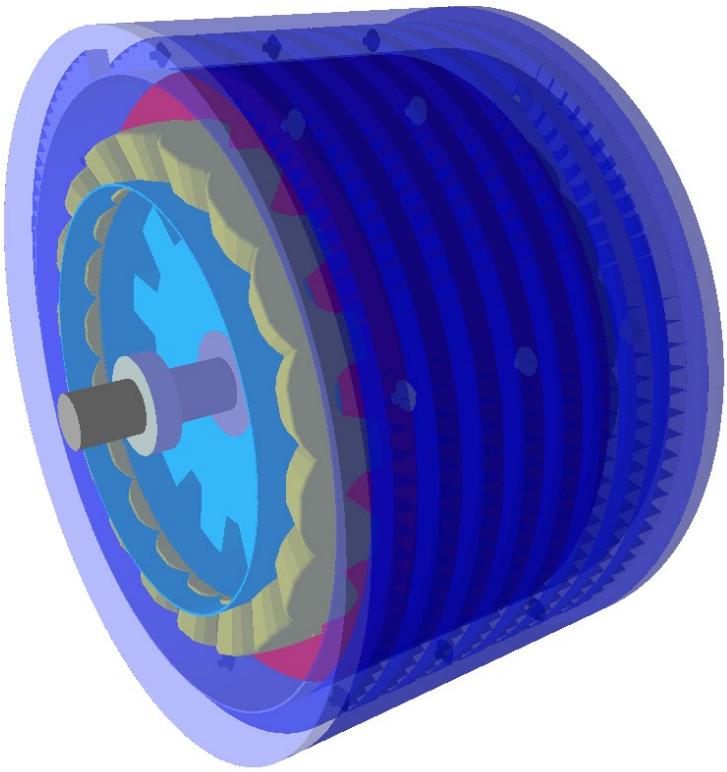

Fig. 6-26. Three-dimensional model used in MotorCAD.

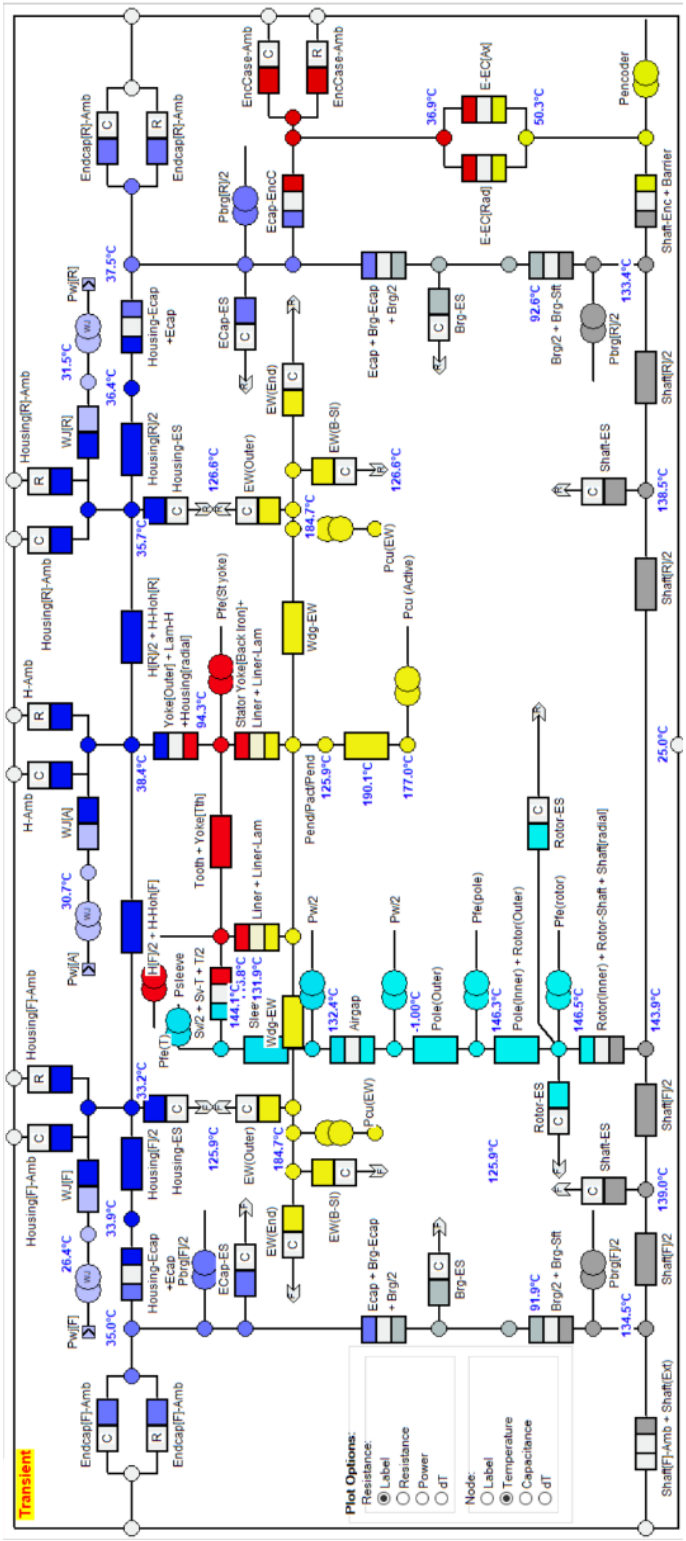

Fig. 6-27. Analytical model of motor for transient thermal performance.

The transient thermal performance of the motor with the assumed cooling system is shown in Fig. 6-28. In comparison to steady state FEA with boundary condition, the steady state temperature of the winding (hotspot) is higher based on the specified cooling system. The magnetic wire selected has 200°C thermal limit, and options selected for impregnation material has 180°C and 204°C thermal limit. For the impregnation epoxy "CoolTherm® EP-2000" is used, there is no time limit for continues operation.

The results of the thermal simulations show that the sizing of the motor was appropriate for the given loading conditions and temperature rise. The motor would still require a detailed thermal design to determine other aspect of the thermal management system such as the pressure drop, transient operation, manufacturing of the water jacket, lifetime of the motor, and cost.

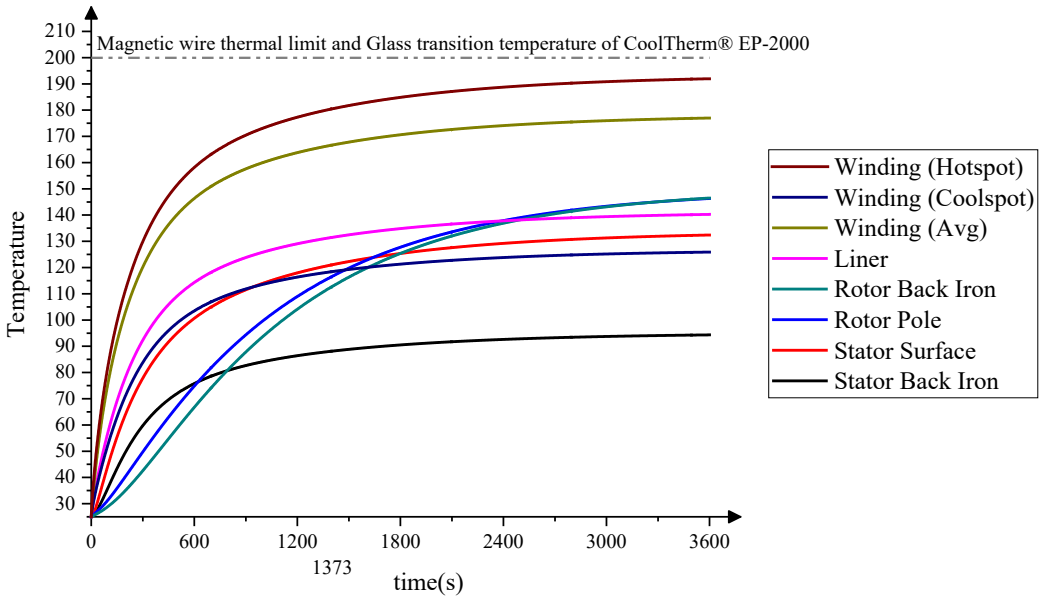

Fig. 6-28. Transient thermal performance of motor with different material thermal constraints.

6.9: Conclusions

In this chapter, the design of the light-sport aircraft switched reluctance motor design is presented. First, a simple comparison of the motor performance is conducted for electrical steel with high silicon content and iron-cobalt alloy. The iron-cobalt alloy with high magnetic saturation is selected as the core material to improve the torque density. The motor geometry is designed using the framework proposed in Chapter 5. In the first stage of the design process, the static design finds the geometries with the highest average static torque. Each of those geometries are further enhanced in the dynamic design stage, which optimizes the geometry and control parameters in a loop to improve the performance. After the dynamic optimization, the best geometry is selected as the final design. The final motor geometry shows high average torque, low torque ripple, and the dominant radial force harmonics are also reduced. A coil configuration is selected considering the electromagnetic torque production, AC copper loss, and practical limitations for the implementation of the coils. The coil retention is designed to secure the coils in place in the stator slot without affecting the slot area and the performance of the motor. The use of cut-outs on the rotor core is proposed as a method of reducing rotor mass. The electromagnetic performance of the motor is examined to ensure that the cut-outs do not impair the performance, and the mechanical stress analysis is performed to ensure there are no high-stress concentration points in the rotor.

This final electromagnetic design satisfies the design requirements motor volume constraints. The torque-speed characteristic is obtained by optimizing the

conduction angles for the nominal current reference. Calculation of the motor's efficiency and losses at base speed with a long conduction period is carried out. In order to ensure that the maximum temperature of the motor in continuous operation does not exceed the material's limitations, steady-state thermal analysis and transient thermal analysis of the motor is performed using FEA with forced boundary conditions and transient analytical model.

Chapter 7

7. Conclusions and Future Work

7.1: Conclusion

Due to the propeller load's nature and the cabin's isolation from noise, switched reluctance motors make an excellent candidate for the propulsion system of electrified light-sport aircraft. Electric LSAs are more efficient, use smaller motors, provide better aerodynamics, have a simpler gearbox or no gearbox, and require simpler cooling systems compared to conventional LSAs. In addition to not emitting greenhouse gases into the atmosphere, they also reduce operational and purchasing costs. The proposed direct-drive SRM is designed to replace a 70-kW permanent magnet synchronous motor used in the aerospace industry with the same dimensional constraints and operational requirements. Iron-cobalt alloy, HIPERCO® 50A with high magnetic saturation is selected as the core material to improve the torque density. In order to meet the high-power density requirements of the aviation industry, a design framework is proposed which includes several

layers of the design process. The framework objectifies the average torque, torque ripple, and radial forces by integrating the control and geometry design. The resulted final motor geometry shows high average torque, low torque ripple, and the dominant radial force harmonics are reduced for base speed. A coil configuration is chosen based on performance and prototyping considerations. The coil retention is designed to hold the coils in place in the stator slot without affecting the slot area and performance of the motor. The use of cutouts on the rotor core is proposed as a method of reducing rotor mass. After adding cutouts, in addition to examining the electromagnetic performance of the motor, it is analyzed for mechanical stress to ensure no high-stress points are present in the rotor. A steady-state and transient thermal analysis of the motor is performed to validate the feasibility of the cooling system. The final electromagnetic design meets all motor requirements while being constrained by motor geometry constraints.

7.2: Future Work

The multi-objective design framework presented in this thesis can be improved in a number of ways. By increasing the number of objectives in the control parameter optimization process and using current profiling, it is possible to enhance the integration of control and geometry design. The mutual coupling of the motor can be considered in the control parameter optimization model. Furthermore, the gains of the mode shapes in the radial force objective can be adjusted according to each mode shape's damping ratio and natural frequency. For verification, a three-dimensional FEA model can be used rather than a two-dimensional model.

The design process is focused on the base speed; other operational speeds can be included in the design framework. Multiphysics integration with mechanical software to simulate the load is an effective method of understanding the motor's operational limits.

The performance of thermal systems needs to be validated, and the thermal design needs to be improved. This can be accomplished by taking different cooling mechanisms, materials, and manufacturing techniques into account.

The designed motor is currently undergoing prototyping with the sponsorship of Carpenter Technology. The motor will undergo several electromagnetic tests, validations, and calibrations as part of the prototyping process.

7.3: Publications

M. E. Abdollahi, N. Vaks, and B. Bilgin, "A multi-objective optimization framework for the design of a high power-density switched reluctance motor," in *Proc. IEEE Trans. Electric. Conf. Expo. (ITEC)*, Anaheim, USA, Jun. 2022

M. E. Abdollahi, A. Zahid, N. Vaks, and B. Bilgin, "Switched Reluctance Motor Design for a Light Sport Aircraft Application," *(Under Preparation)*

References

[1] United Nations Framework Convention on Climate Change (UNFCC). (May. 2016) *Methodological Issues under the Convention: Emissions from Fuel Used for International Aviation and Maritime Transport*. [Online]. Available: https://www.icao.int.

[2] U.S. Department of Transportaion and Transport Canada. (Feb. 2021) *Government of Canada Joint Statement by Transport Canada and the U.S. Department of Transportation on the Nexus between Transportation and Climate Change.* [Online]. Available: https://www.canada.ca/.

[3] David Suzuki Foundation on Nature. (Mar. 2020) *Air Travel and Climate Change*. [Online]. Available: https://davidsuzuki.org/.

[4] The U.S. Department of Energy Bioenergy Technologies Office (BETO). (Sept. 2021) *Sustainable Aviation Fuels* [Online]. Available: https://www.energy.gov/.

[5] UBS Investment Bank. (Jun. 2019) *Green Power: Will climate change propel the sector towards Hybrid Electric Aviation*. [Online]. Available: https://www.ubs.com/.

[6] National Renewable Energy Laboratory (NREL). (Oct. 2021) *Electrification of Aircraft: Challenges, Barriers, and Potential Impacts.* [Online]. Available: https://www.nrel.gov/.

[7] M. Kozlova, T. Nykanen, and J Yeomans, "Technical advances in aviation electrification: enhancing strategic R&D investment analysis through simulation decomposition," *Sustainability*, vol. 14, no. 1, p. 414, Dec. 2021.

[8] J. Overton, "Fact Sheet: The Growth in Greenhouse Gas Emissions from Commercial Aviation," *Environmental and Energy Study Institute*, Oct. 2019. [Online]. Available: https://www.eesi.org/.

[9] G. Bye. (Oct. 2018) *Sun Flyer*. [Online]. Available: https://nbaa.org/.

[10] L. Josephs. (May. 2022) *A Severe Pilot Shortage in the U.S. Leaves Airlines Scrambling for Solutions*. [Online]. Available: https://www.cnbc.com/.

[11] J. Siebenmark. (Oct. 2021) *Flight Training Schools Order 30 Cessna 172 Skyhawks*. [Online]. Available: https://www.ainonline.com/.

[12] C. Alcock. (Jan. 2021) *Bye Starts Series Production of Electric eFlyer 2*. [Online]. Available: https://www.ainonline.com/.

[13] Aircraft Owners and Pilots Association. (Feb. 2009) *Regulatory Brief - General Aviation and Greenhouse Gas Emission*. [Online]. Available: https://www.aopa.org/.

[14] K. Thanikasalam, M. Rahmat, A. G. Mohammad Fahmi, A. M. Zulkifli, N. N. Shawal, K. Ilanchelvi, M. Ananth, and R. Elayarasan, "Emissions of piston engine aircraft using aviation gasoline (avgas) and motor gasoline (mogas) as fuel – a review," in *Proc. IOP Conf. Series: Mater. Sci. Eng.*, Batu Ferringhi, PNG, Malaysia, May 2018, vol. 370, pp. 012012.

[15] Rolls-Royce. (Nov. 2021) *Spirit of Innovation stakes claim to be the world's fastest all-electric vehicle.* [Online]. Available: https://www.rolls-royce.com/.

[16] K. Connor. (Jan. 2022) *Rolls-Royce Electric Aircraft Becomes World's Fastest.* [Online]. Available: https://www.avweb.com/.

[17] F. Lambert. (Apr. 2018) *First all-electric trainer plane gets airworthiness certification from the FAA in the US.* [Online]. Available: https://electrek.co/.

[18] U.S. Department of Transportation - Federal Aviation Administration. (Feb. 2004) *Powerplant Guide For Certification of Part 23 Airplanes and Airships.* [Online]. Available: https://rgl.faa.gov/.

[19] Pipistrel Aircraft. (Jul. 2020) *E-811 - Electric Engine - Certificates & Registration.* [Online]. Available: https://www.pipistrel-aircraft.com/.

[20] Pipistrel Aircraft. (May 2020) *E-811 - Type Certificate - EASA.E.234.* [Online]. Available: https://www.pipistrel-aircraft.com/

[21] F. Anton, O. Otto, J. Hetz, and T. Olbrechts. (Apr. 2018) *Siemens eAircraft*. [Online]. Available: https://www.ie-net.be/.

[22] Siemens. (Jun. 2016) *Rekord-Motor SP260D und Extra 330LE.* [Online]. Available: https://assets.new.siemens.com/.

[23] MagniX. (Apr. 2019) *Magnix Products.* [Online]. Available: https://magnix.aero/.

[24] Pipistrel Aircraft. (2020) *E-811 - Electric Engine.* [Online]. Available: https://www.pipistrel-aircraft.com/.

[25] F. Anton and O. Otto. (Sep. 2019) *eAircraft: Hybrid-elektrische*. [Online]. Available: https://www.bbaa.de/.

[26] M. Harris and R. Applegarth. (Mar. 2019) *What to Know: Siemens Hybrid-Electric Propulsion Systems*. [Online]. Available: https://www.avbuyer.com/.

[27] E. Elhomdy, Z. Liu, and G. Li, "Thermal and mechanical analysis of a 72/48 switched reluctance motor for low-speed direct-drive mining applications," *App. Sci.*, vol. 9, no. 13, p. 2722, Jul. 2019.

[28] M. Kasprzak, J. W. Jiang, B. Bilgin and A. Emadi, "Thermal analysis of a three-phase 24/16 switched reluctance machine used in HEVs," in *Proc. IEEE Energy Convers. Congr. Expo. (ECCE),* Milwaukee, WI, USA, Sept. 2016, pp. 1-7.

[29] B. Bilgin, J. W. Jiang, and A. Emadi, “Thermal management of switched reluctance machines,” in *Switched reluctance motor drives: fundamentals to applications.* Boca Raton, FL, USA: CRC Press/Taylor & Francis Group, 2019.

[30] D. Staton, "Thermal analysis of traction motors," in *Proc. IEEE Trans. Electrific. Conf. Expo. (ITEC),* Ellesmere, Shrops., UK, Jun. 2014, pp. 1–139.

[31] B. Bilgin, P. Magne, P. Malysz, Y. Yang, V. Pantelic, M. Preindl, A. Korobkine, W. Jiang, M. Lawford, and A. Emadi, "Making the case for electrified transportation," *IEEE Trans. Transp. Electr.*, vol. 1, no. 1, pp. 4-17, Jun. 2015.

[32] K. Nansai, K. Nakajima, S. Kagawa, Y. Kondo, Y. Shigetomi, and S. Suh, "Global mining risk footprint of critical metals necessary for low-carbon technologies: the case of neodymium, cobalt, and platinum in Japan," *Am. Chem. Soc.,* Jan. 2015.

[33] US Environmental Protection Agency. (Dec. 2012) *Rare Earth Elements: A Review of Production, Processing, Recycling, and Associated Environmental Issues.* [Online]. Available: https://nepis.epa.gov.

[34] B. Plumer. (Oct. 2014) *China no longer has a stranglehold on the world's supply of rare earth metals.* [Online]. Available: https://www.vox.com/.

[35] K. bradsher. (Oct. 2010) *After China's rare earth embargo, a new calculus*. [Online]. Available: https://www.nytimes.com/.

[36] M. Filipenko. (Jul. 2019) *Electric and Hybrid-Electric Aircraft: A pragmatic view*. [Online]. Available: https://indico.cern.ch.

[37] B. Bilgin, J. W. Jiang, and A. Emadi, “Derivation of pole configuration in switched reluctance machines,” in *Switched reluctance motor drives: fundamentals to applications.* Boca Raton, FL, USA: CRC Press/Taylor & Francis Group, 2019.

[38] J. Liang, A. Callegaro, B. Howey, B. Bilgin, J. Dong, J. Lin, and A. Emadi, "Analytical calculation of temporal and circumferential orders of radial force density harmonics in external-rotor and internal-rotor switched reluctance machines," *IEEE Open Journal of Ind. Appl.*, vol. 2, pp. 70-81, Apr. 2021.

[39] Altair Co. (2022) *Altair FluxTM 2022.1 User Guide.* [Online]. Available: https://www.altair.com/.

[40] A. D. Callegaro, B. Bilgin, and A. Emadi, "Radial force shaping for acoustic noise reduction in switched reluctance machines," *IEEE Trans. Power Electron*., vol. 34, no. 10, pp. 9866-9878, Oct. 2019.

[41] B. Bilgin, J. W. Jiang, and A. Emadi, “Noise and vibration in switched reluctance machines,” in *Switched reluctance motor drives: fundamentals to applications.* Boca Raton, FL, USA: CRC Press/Taylor & Francis Group, 2019.

[42] B. Bilgin, J. W. Jiang, and A. Emadi, “Fundamentals of vibrations and acoustic noise,” in *Switched reluctance motor drives: fundamentals to applications.* Boca Raton, FL, USA: CRC Press/Taylor & Francis Group, 2019.

[43] M. Abdalmagid, E. Sayed, M. H. Bakr, and A. Emadi, "Geometry and topology optimization of switched reluctance machines: a review," *IEEE Access*, vol. 10, pp. 5141-5170, Jan. 2022.

[44] P. C. Desai, M. Krishnamurthy, N. Schofield, and A. Emadi, "Novel switched reluctance machine configuration with higher number of rotor poles than stator poles: concept to implementation," *IEEE Trans. Ind. Electron*., vol. 57, no. 2, pp. 649-659, Feb. 2010.

[45] A. Chiba, Y. Takano, S. Ogasawara, M. Takeno, N. Hoshi, T. Imakawa, and M. Takemoto, "Torque density and efficiency improvements of a switched reluctance motor without rare-earth material for hybrid vehicles," *IEEE Trans. Ind. Appl.*, vol. 47, no. 3, pp. 1240-1246, May.-Jun. 2011.

[46] X. Song, Y. Park, J. Li, and J. Lee, "Optimization of switched reluctance motor for efficiency improvement using response surface model and kriging model," in *Proc. Int. Joint Conf. Comput. Sci. Optim*., Kunming, Yunnan, China, Apr. 2011, pp. 259-260.

[47] P. T. Hieu, D. Lee, and J. Ahn, "Design of 2-phase 4/2 SRM for torque ripple reduction," in *Proc. Int. Conf. Elect. Mach. Syst. (ICEMS)*, Sapporo, HK, Japan, Oct. 2012, pp. 1-6.

[48] Y. K. Choi, H. S. Yoon, and C. S. Koh, "Pole-shape optimization of a switched-reluctance motor for torque ripple reduction," *IEEE Trans. Magn.*, vol. 43, no. 4, pp. 1797-1800, Apr. 2007.

[49] K. Kiyota, T. Kakishima, A. Chiba, and M. A. Rahman, "Cylindrical rotor design for acoustic noise and windage loss reduction in switched reluctance motor for HEV applications," *IEEE Trans. Ind. Appl.*, vol. 52, no. 1, pp. 154-162, Jan.-Feb. 2016.

[50] S. Hosseini and Y. Alinejad-Beromi, "Noise reduction in switched reluctance motor by modifying the structures," *IET Electr. Power Appl.*, vol. 14, no. 14, pp. 2863–2872, Dec. 2020.

[51] D. Tekgun, "Acoustic Noise and Vibration Reduction on Switched Reluctance Machines through Hole Placement in Stator/Rotor Laminations," M.S. thesis, Dept. Elect. Eng., Akron. Uni., Akron, OH, USA, 2017.

[52] X. D. Xue, K. W. E. Cheng, and S. L. Ho, "Optimization and evaluation of torque-sharing functions for torque ripple minimization in switched reluctance motor drives," *IEEE Trans. Power Electron.*, vol. 24, no. 9, pp. 2076-2090, Sept. 2009.

[53] H. Li, B. Bilgin, and A. Emadi, "An improved torque sharing function for torque ripple reduction in switched reluctance machines," *IEEE Trans. Power Electron.*, vol. 34, no. 2, pp. 1635-1644, Feb. 2019.

[54] R. Mikail, I. Husain, Y. Sozer, M. S. Islam, and T. Sebastian, "Torque-ripple minimization of switched reluctance machines through current profiling," *IEEE Trans. Ind. Appl.*, vol. 49, no. 3, pp. 1258-1267, Jun. 2013.

[55] J. Furqani, M. Kawa, K. Kiyota, and A. Chiba, "Comparison of current waveforms for noise reduction in switched reluctance motors," in *Proc. IEEE Energy Convers. Congr. Expo. (ECCE)*, Cincinnati, OH, USA, Oct. 2017, pp. 752-759.

[56] S. Li, S. Zhang, C. Jiang, J. R. Mayor, T. G. Habetler, and R. G. Harley, "A fast control-integrated and multiphysics-based multi-objective design optimization of switched reluctance machines," in *Proc. IEEE Energy Convers. Congr. Expo. (ECCE)*, Cincinnati, OH, USA, Oct. 2017, pp. 730-737.

[57] C. Ma and L. Qu, "Multiobjective optimization of switched reluctance motors based on design of experiments and particle swarm optimization," *IEEE Trans. Energy Convers.*, vol. 30, no. 3, pp. 1144-1153, Sept. 2015.

[58] Carpenter Electrification. (2020) HIPERCO® 50. [Online]. Available: https://www.carpenterelectrification.com/.

[59] JFE Steel Corp. (2021) Super Core™. [Online]. Available: https://www.jfe-steel.co.jp/

[60] J. W. Jiang, B. Bilgin, A. Sathyan, H. Dadkhah, and A. Emadi, "Analysis of unbalanced magnetic pull in eccentric IPM machines with series and parallel windings," *IET Electric Power Applications*, vol. 10, no. 6, pp. 526-538, 2016.

[61] M. Kasprzak, "6/14 Switched Reluctance Machine Design for Household HVAC System Applications," M.S. thesis, Dept. Mech. Eng., McMaster Uni., Hamilton, ON, Canada, 2017. [Online]. Available: http://hdl.handle.net/11375/20877.

[62] C. Rhebergen, B. Bilgin, A. Emadi, E. Rowan, and J. Lo, "Enhancement of electric motor thermal management through axial cooling methods: a materials

approach," in *Proc. IEEE Energy Convers. Congr. Expo. (ECCE)*, Montreal, QC, Canada, Oct. 2015, pp. 5682-5688.

[63] Parker Lord. (Aug. 2021) *CoolTherm® EP-2000 Thermally Conductive Epoxy Encapsulant.* [Online]. Available: https://www.lord.com/.

[64] 3D Systems Corp. (Dec. 2007) *DuraForm® PA plastic.* [Online]. Available: https://www.3dsystems.com/.

[65] DuPont (Apr. 2014) *DuPont™ Nomex® 818.* [Online]. Available: https://www.dupont.com/.